Missouri S&T Library and Learning Resources

Scholars' Mine

Doctoral Dissertations

Student Theses and Dissertations

Summer 2014

Emission source microscopy for electromagnetic interference source localization

Pratik Rajesh Maheshwari

Follow this and additional works at: https://scholarsmine.mst.edu/doctoral_dissertations

Part of the Electrical and Computer Engineering Commons

Department: Electrical and Computer Engineering

Recommended Citation

Maheshwari, Pratik Rajesh, "Emission source microscopy for electromagnetic interference source localization" (2014). *Doctoral Dissertations*. 2334.
https://scholarsmine.mst.edu/doctoral_dissertations/2334

This thesis is brought to you by Scholars' Mine, a service of the Missouri S&T Library and Learning Resources. This work is protected by U. S. Copyright Law. Unauthorized use including reproduction for redistribution requires the permission of the copyright holder. For more information, please contact scholarsmine@mst.edu.

EMISSION SOURCE MICROSCOPY

FOR ELECTROMAGNETIC INTERFERENCE SOURCE LOCALIZATION

by

PRATIK RAJESH MAHESHWARI

A DISSERTATION

Presented to the Faculty of the Graduate School of the

MISSOURI UNIVERSITY OF SCIENCE AND TECHNOLOGY

In Partial Fulfillment of the Requirements for the Degree

DOCTOR OF PHILOSOPHY

in

COMPUTER ENGINEERING

2014

Approved
Dr. Sahra Sedighsavestani, Advisor
Dr. David Pommerenke, Co-Advisor
Dr. Victor Khilkevich
Dr. Reza Zoughi
Dr. Frank Liu

© 2014

PRATIK RAJESH MAHESHWARI

All Rights Reserved

ABSTRACT

For complex and large systems with multiple sources, it is often difficult to localize the sources of radiation. Near-field electromagnetic scanning is used often for root-cause diagnosis by determining field distribution close to the PCB. In the near-field, the evanescent waves are dominant, which may lead to the misinterpretation of them being the dominant sources contributing to the far-field. Another limitation of near-field scanning is that the probe may not be able to access all locations near the PCB due to the complex geometry and high component density. Two-dimensional synthetic aperture radar is a well-known technique used for antenna diagnostic and alignment of phase array antennas. Using a technique which is derived from the synthetic aperture radar we present emission source microscopy to localize the sources of active radiation on a PCB. After obtaining the location of sources, using near field to far-field transformation, it is shown that the far-field radiation patterns and the total radiated power can be estimated. Using masking algorithms the contribution of individual sources to far-field can be determined. The source localization methodology is presented along with simulation and measurement results on real-DUTs. The results show that the proposed method is capable of detecting multiple active sources on a complex PCB. Different phase measurement methods are presented along with the measurement results. Also, methods to reduce the scanning time for source localization are presented.

ACKNOWLEDGMENTS

Firstly I would like to thank my parents and my sister for their support in my whole life. I owe my loving thanks to my wife, Richa Shekhar, for all her care, understanding and unwavering support throughout my PhD studies.

I would like to express my sincere gratitude to both my advisors Dr. Sahra Sedighsarvestani and Dr. David Pommerenke for years of guidance throughout the PhD study and research. Except from the technical things, they also helped me grow as an individual. I would also like to specially thank Dr. Victor Khilkevich for his continuous guidance and time and enhancing my learning experience through numerous discussions. I would also like to thanks the members of PhD advisory committee, Dr. Reza Zoughi and Dr. Frank Liu, for their time and effort in reviewing this dissertation. It is pleasure to thank all my friends at the EMC laboratory and SendeComp laboratory for their company and assistance in my research work

Last but not the least, I would like to thank the amazing friends I met during my PhD studies here at Rolla and would continue to cherish their friendship throughout my life.

TABLE OF CONTENTS

Page

ABSTRACT ... iii
ACKNOWLEDGMENTS ... iv
LIST OF ILLUSTRATIONS ... vii
LIST OF TABLES ... xiii
SECTION
1. INTRODUCTION ... 1
1.1. MOTIVATION ... 1
2. EMISSION SOURCE MICROSCOPY METHOODLGY ... 8
2.1. INTRODUCTION TO ALGORITHM ... 8
2.2. ANALYTICAL FORMULATION OF THE ESM ALGORITHM ... 8
2.2.1. Test of Methodology on Analytical Data. ... 10
2.2.2. Resolution of Reconstructed Image. ... 16
2.2.3. Suppression of Evanescent Wave Component. ... 17
2.3. PLANAR NEAR-FIELD TO FAR-FIELD TRANSFORMATION ... 18
2.4. MASKING OF INDIVIDUAL SOURCES ... 20
2.5. ACCURACY ESTIMATION IN ESM ALGORITHM ... 26
2.5.1. Measurement Plane Truncation.. ... 26
2.5.2. Cable Amplitude and Phase Variation.. ... 27
2.5.3. Non-Planarity of the Measurement Surface. ... 27
2.5.4. Scan Plane Distance Uncertainty. ... 27
2.5.5. Uncorrelated Phase Error. ... 28
3. VALIDATION OF METHODOLOGY ... 30
3.1. SIMULATION ON A CUSTOM PCB ... 30
3.2. DETERMINING FAR-FIELD CONTRIUBTION FROM INDIVDUAL SOURCES ... 43
3.3. EFFECT OF SCANNING PARAMETRS ... 54
3.4. MEASUREMENT METHODOLOGY AND RESULTS ... 57
3.4.1. Measurement Setup. ... 57

3.4.2. Antenna Factor Compensation. 59
3.4.3. Measurement Results and Comparison with Simulated Data. 61
3.4.4. Determining Far-Field Contribution from Individual Sources.......... 74
3.5. EFFECT OF HEATSINK ON THE FAR-FIELD PARAMETRS 81
4. TEST OF METHODOLOGY ON ACTUAL DUT 84
4.1. REAL DUT 1 – NETWORK SWITCH.......... 85
4.2. REAL DUT 2 – FPGA EVALUATION BOARD.......... 111
4.3. REAL DUT 3 – ORTHOGONAL PCBS 116
4.4. TIME-DOMAIN PHASE MEASUREMENT METHOD.......... 120
5. CONCLUSION & FUTURE WORK 125
BIBLIOGRAPHY.......... 126
VITA 131

LIST OF ILLUSTRATIONS

Page

Figure 2.1 Dipole location and measurement plane.. 12

Figure 2.2 Focused fields at different distance with dipoles at same height. 14

Figure 2.3 Focused fields at different distances with dipoles at different height. 15

Figure 2.4 Aperture angle given by the span of the scan plane. 16

Figure 2.5 Algorithm to determine individual source contribution. 21

Figure 2.6 Recorded fields on the scanning plane. 21

Figure 2.7 Recorded fields after zero padding. 22

Figure 2.8 Focused fields on the source plane. 23

Figure 2.9 Calculated far-field pattern obtained from recorded fields. 24

Figure 2.10 Calculated far-field pattern obtained analytical formula. 24

Figure 2.11 Masking sources to isolate only one dipole source. 25

Figure 2.12 Far-field from masked image (containing single dipole contribution). 25

Figure 2.13 Error in the far-field Etheta component versus aperture angle...................... 26

Figure 2.14 Error in the maximum amplitude of the focused field with scan plane distance uncertainty. 28

Figure 2.15 Error in the maximum amplitude of the focused Ex field with addition of random phase variations. 29

Figure 2.16 Error in the maximum amplitude of the focused Ey field with addition of random phase variations. 29

Figure 3.1 Model of Custom PCB. 30

Figure 3.2 Simulated return loss of the larger patches... 31

Figure 3.3 Recorded Ex magnitude (V/m) field and phase (rad) from simulation. 33

Figure 3.4 Recorded Ey magnitude (V/m) and phase (rad) field from simulation. 34

Figure 3.5 Reconstructed Ex field magnitude (V/m) and phase (rad) on the source plane. 35

Figure 3.6 Reconstructed Ey field magnitude (V/m) and phase (rad) on the source plane. 36

Figure 3.7 3D Far-field pattern using Etheta component (dBV/m) of the DUT calculated from NF-FF transform of the focused fields on PCB plane. 37

Figure 3.8 3D Far-field pattern using Etheta component (dBV/m) of the DUT obtained from full wave simulation tool. 38

Figure 3.9 3D Far-field pattern using Etheta component (V/m) obtained from CST. 39

Figure 3.10 Constant Theta = 20 pattern using Etheta component (dBV/m). 40

Figure 3.11 Constant Theta = 45 pattern using Etheta component (dBV/m). 41

Figure 3.12 Constant Phi = 0 pattern using Etheta component (dBV/m). 41

Figure 3.13 Constant Phi = 90 pattern using Etheta component (dBV/m). 42

Figure 3.14 Reconstructed Ex field magnitude (V/m) with source corresponding to patch P1 kept active. 44

Figure 3.15 Reconstructed Ey field magnitude (V/m) with source corresponding to patch P1 kept active. 44

Figure 3.16 3D Far-field pattern for Etheta component (dBV/m) of the DUT obtained from masked fields. 45

Figure 3.17 3D Far-field pattern for Etheta component (dBV/m) of the DUT obtained from CST with only Patch P1 active. 46

Figure 3.18 Constant Phi = 0 pattern using Etheta component (dBV/m). 47

Figure 3.19 Constant Phi = 90 pattern using Etheta component (dBV/m). 47

Figure 3.20 Constant Theta = 20 pattern using Etheta component (dBV/m). 48

Figure 3.21 Constant Theta = 45 pattern using Etheta component (dBV/m). 48

Figure 3.22 Reconstructed Ex field magnitude (V/m) with source corresponding to patch P2 kept active. 49

Figure 3.23 Reconstructed Ey field magnitude (V/m) with source corresponding to patch P2 kept active. 50

Figure 3.24 3D Far-field pattern for Etheta component (dBV/m) of the DUT obtained from masked fields. 51

Figure 3.25 3D Far-field pattern for Etheta component (dBV/m) of the DUT obtained from CST with only Patch P2 active. 51

Figure 3.26 Constant Phi = 0 pattern using Etheta component (dBV/m). 52

Figure 3.27 Constant Phi = 90 pattern using Etheta component (dBV/m). 52

Figure 3.28 Constant Theta = 20 pattern using Etheta component (dBV/m). 53

Figure 3.29 Constant Theta = 45 pattern using Etheta component (dBV/m). 53

Figure 3.30 Measurement setup. 58

Figure 3.31 Open-ended waveguide used as scanning antenna. 58

Figure 3.32 Open-ended waveguide CST model top and side view. 60

Figure 3.33 Measured |S21 | probe output on the scanning plane at 73.2 mm height for X and Y orientations of the antenna. 61

Figure 3.34 Measured Ex field magnitude (V/m) and phase (rad) at 73.2 mm height above the DUT. 62

Figure 3.35 Measured Ey field magnitude (V/m) and phase (rad) at 73.2 mm height above the DUT. 63

Figure 3.36 Simulated Ex field magnitude (V/m) and phase (rad) at 73.2 mm height above the DUT after normalizing. 64

Figure 3.37 Simulated Ey field magnitude (V/m) and phase (rad) at 83.2 mm height above the DUT after normalizing. 65

Figure 3.38 Reconstructed Ex field magnitude (V/m) and phase (rad) on PCB plane from measurement. 66

Figure 3.39 Reconstructed Ey field magnitude (V/m) and phase (rad) on PCB plane from measurement. 67

Figure 3.40 Reconstructed Ex field magnitude (V/m) and phase (rad) on PCB plane from full-wave simulation. 68

Figure 3.41 Reconstructed Ey field magnitude (V/m) and phase (rad) on PCB plane from full-wave simulation. 69

Figure 3.42 3D Far-field pattern using Etheta component (dBV/m) of the DUT calculated from NF-FF transform of the measured focused fields on PCB plane. 71

Figure 3.43 3D Far-field pattern using Etheta component (dBV/m) of the DUT calculated from NF-FF transform of the simulated focused fields on PCB plane. 71

Figure 3.44 Constant Phi = 0 pattern using Etheta component (dBV/m). 72

Figure 3.45 Constant Phi = 90 pattern using Etheta component (V/m). 73

Figure 3.46 Constant Theta = 20 pattern using Etheta component (V/m). 73

Figure 3.47 Constant Theta = 45 pattern using Etheta component (V/m). 74

Figure 3.48 Reconstructed Ex field magnitude (V/m) with source corresponding to patch P1 kept active (simulation results). 75

Figure 3.49 Reconstructed Ey field magnitude (V/m) with source corresponding to patch P1 kept active (simulation results). 75

Figure 3.50 Reconstructed Ex field magnitude (V/m) with source corresponding to patch P1 kept active (measurement results). 76

Figure 3.51 Reconstructed Ey field magnitude (V/m) with source corresponding to patch P1 kept active (measurement results). 76

Figure 3.52 3D Far-field pattern for Etheta component (dBV/m) of the DUT obtained from masked fields (Using scanned fields). 77

Figure 3.53 3D Far-field pattern for Etheta component (dBV/m) of the DUT obtained from masked fields (Using recorded fields). 78

Figure 3.54 Constant Phi = 0 pattern using Etheta component (dBV/m). 79

Figure 3.55 Constant Phi = 90 pattern using Etheta component (dBV/m). 79

Figure 3.56 Constant Theta = 45 pattern using Etheta component (dBV/m). 80

Figure 3.57 Constant Theta = 20 pattern using Etheta component (dBV/m). 80

Figure 3.58 Measured Ex field magnitude (V/m) on a rectangular plane at 73.2 mm above the DUT with heatsink. 81

Figure 3.59 Measured Ey field magnitude (V/m) on a rectangular plane at 73.2 mm above the DUT with heatsink. 82

Figure 3.60 Reconstructed Ex field magnitude (V/m) on the PCB plane. 82

Figure 3.61 Reconstructed Ey field magnitude (V/m) on the PCB plane. 83

Figure 4.1 Radiation spectrum from the DUT. 86

Figure 4.2 Measurement setup for phase and amplitude measurement. 87

Figure 4.3 Actual Measurement setup. 87

Figure 4.4 (a) Measured Ex field magnitude in dBV (b) Measured Ex field phase in rad. 90

Figure 4.5 (a) Measured Ey field magnitude in dBV (b) Measured Ey field phase in rad. 91

Figure 4.6 Measured total tangential field component magnitude in dBm....................... 93

Figure 4.7 Reconstructed Ex field component magnitude in dBm at the PCB plane. 94

Figure 4.8 Reconstructed Ey field component magnitude in dBm at the PCB plane. 94

Figure 4.9 Applied absorbers (2 cm by 2.8 cm). 95

Figure 4.10 Reconstructed Ex fields at the PCB plane with absorber. 96

Figure 4.11 Reconstructed Ey fields at the PCB plane, with absorber. 97

Figure 4.12 Setup for TRP measurement in a reverberation chamber. 98

Figure 4.13 TRP spectrums comparison with and without the absorber material. 98

Figure 4.14 Absorber material below the heatsink (a) Top view (b) side view................ 99

Figure 4.15 Calibration setup from TRP measurement. 100

Figure 4.16 Actual DUT measurement setup from TRP measurement. 101

Figure 4.17 TRP spectrums comparison with and without the absorber material from experiment and simulation. ... 101

Figure 4.18 Actual placement of the absorber material. ... 102

Figure 4.19 Reconstructed Ex and Ey field magnitude on the DUT without any absorber material. ... 103

Figure 4.20 Reconstructed Ex and Ey field magnitude on the DUT with the absorber material below the ASIC heatsink. ... 103

Figure 4.21 Reconstructed Ex and Ey field magnitude on the DUT with the absorber material around the PHY heatsink. ... 104

Figure 4.22 Reconstructed Ex and Ey field magnitude on the DUT with the absorber material around the PHY heatsink and below the ASIC heatsink. ... 104

Figure 4.23 TRP results for DUT1 with and without the absorber below ASIC heatsink. ... 105

Figure 4.24 TRP results for DUT1 with and without the absorber around PHY heatsink. ... 105

Figure 4.25 TRP results for DUT1 with and without the absorber around PHY heatsink and below ASIC. ... 106

Figure 4.26 Reconstructed Ex fields at the PCB plane, without absorber. ... 108

Figure 4.27 Reconstructed Ey fields at the PCB plane, without absorber. ... 109

Figure 4.28 Reconstructed Ex fields at the PCB plane, with absorber. ... 110

Figure 4.29 Reconstructed Ex fields at the PCB plane, with absorber. ... 110

Figure 4.30 FPGA board phase measurement setup. ... 112

Figure 4.31 Measured Ex field magnitude ratio on a rectangular grid at 10 cm height. 113

Figure 4.32 Measured Ey field magnitude ratio on a rectangular grid at 10 cm height. 113

Figure 4.33 Reconstructed Ex field magnitude ratio on the source plane. ... 114

Figure 4.34 Reconstructed Ey field magnitude ratio on the source plane. ... 114

Figure 4.35 Reconstructed Ex field magnitude ratio on the source plane. ... 115

Figure 4.36 Reconstructed Ey field magnitude ratio on the source plane. ... 116

Figure 4.37 DUT with vertical PCB. ... 117

Figure 4.38 Measurement setup. ... 117

Figure 4.39 Measured field magnitude on the scanning plane at lower height. ... 118

Figure 4.40 Measured field phase on the scanning plane at lower height. ... 118

Figure 4.41 Reconstructed fields on the source plane. ... 119

Figure 4.42 Measured field phase on the scanning plane at 175mm. 119
Figure 4.43 Reconstructed fields on the source plane. 120
Figure 4.44 Time-domain based phase measurement setup. 122
Figure 4.45 Measured field magnitude and phase at 100 mm height. 123
Figure 4.46 Reconstructed Ex field magnitude on the PCB plane. 124
Figure 4.47 Reconstructed Ey field magnitude on the PCB plane. 124

LIST OF TABLES

Page

Table 3.1 Variation in maximum E-field tangential component (dbV/m)........................ 54

Table 3.2 Variation in maximum Etheta value (dbV/m) 55

Table 3.3 Variation in maximum Total radiated power (dBm) 55

Table 4.1 Table showing the reduction in the TRP with absorber material at different locations 106

Table 4.2 Table showing the reduction in the TRP with absorber material below the main ASIC heatsink 111

1. INTRODUCTION

1.1. MOTIVATION

An important step for EMI debugging generally includes locating the sources of EMI and then applying a fix to reduce the radiated emission. But for complex and large systems with multiple sources it is often difficult to locate the source of radiation. Near-field electromagnetic scanning often is used for root cause diagnosis by determining near-field radiation patterns and coupling mechanisms. Near-field scanning may provide information about the surface current, tangential fields and the reactive near-field distribution on the device under test (DUT) [1][2]. The near-field contains both evanescent and propagating fields. In the vicinity of the DUT evanescent waves are dominant, which may lead to the misinterpretation of the dominant sources contributing to the far-field. In practice, however, engineers mainly are concerned about only the sources of electromagnetic interference (EMI) contributing to far-field radiation. To identify these sources, engineers must depend upon their experience or trial and error.

Another limitation of near-field scanning is that the probe may not be able to access all locations near the PCB due to the complex geometry and high component density. Placing the probe very close to the DUT may perturb the field under measurement due to coupling between the probe and the DUT. This leads to the incorrect measurement of fields at different vertical distances from the PCB. However, the advantage of near-field scanning is that it can achieve better resolution depending upon the scanning step and the probe size.

Electromagnetic imaging techniques are commonly used for non-destructive testing, medical, geophysics, radar and remote sensing applications [1]-[12]. Such

techniques have also been used for microwave imaging to detect concealed objects, structural defects and detecting embedded targets in layered media [6]-[8]. Qualitative imaging techniques mainly use migration algorithms to reconstruct the target image. Migration algorithm such as synthetic aperture radar technique migrate the fields back to the source to create a focused image.

In field of antenna measurement, microwave holography is widely used for antenna radiation pattern measurement using near-field scanning, antenna diagnosis and alignment of phase array antennas [9]-[23]. In microwave holography the back propagation is mainly performed to know the details about the structure of the aperture. In [14]-[16] authors have used microwave holography to detect the faulty antennas in antenna arrays. In [16] the authors perform two phase-synchronized near-field measurements and take the difference of the measured fields back to the source plane. Due to this the error amplitude peaks at the faulty antenna elements in the array. Another application is the reconstruction of surface currents by scanning very close to the PCB [43]. The method emphasizes on capturing the maximum evanescent spectrum to reconstruct the fine details of the surface current distribution. Investigators in [42] have demonstrated similar method to detect radiating sources, but they fail to discuss about spectral filtering and spatial sampling requirements without which the algorithm would not work

Errors in measurement such as probe positing and alignment of the probe can be compensated using methods presented in [19]-[23]. Also the scanning plane truncation can lead to a reduction in the accuracy of the reconstructed images [20]. Other factor leading to degradation in the reconstructed images include biased error in scanning plane;

scan plane distance uncertainty, phase and amplitude drift of the measured signal, receiver dynamic range [21][22]. The probe is kept far away from the DUT to avoid mutual coupling and disturbing the fields of the DUT. Other uncertainties such as probe relative pattern and cable phase stability may be difficult to control.

Standard or conventional SAR methods uses reflected signals from target and received by a scanning antenna to reconstruct the target's image [1]-[4]. To overcome the limitations of near-field scanning in locating active EMI radiation sources, the emission source microscopy (ESM) technique derived on methods employed in microwave imaging is presented in this work. The fields from the active radiation sources with amplitude and phase are measured on planar surface away from the DUT. In principle, the fields can be obtained simultaneously using antennas or probe arrays; however, this is difficult to achieve. A more practical approach is to use a moving probe or antenna and sample the field sequentially from point to point. In this case, the scanning plane can be thought of as a synthetic aperture of a large antenna.

The main contributions of this work are the application of emission source microscopy to locate active source of EMI radiation on a PCB. A measurement methodology is presented to overcome challenges associated with identifying sources relevant to EMC applications. In this technique the phase and magnitude of the fields are measured on a planar surface a few wavelengths away from the DUT to be outside the reactive-near field region of the DUT. The scanned fields are back-propagated to the source plane after spectral filtering to identify the radiation sources. Different phase measurement using frequency and time-domain approaches have been shown. Another contribution is to show that individual sources can be identified and isolated. Using near-

field to far-field, far-field contribution from each source can be calculated. In addition, the total radiated power can be calculated for individual sources to determine the source contributing to maximum radiation. The parameters that may affect the accuracy of the ESM methodology are also discussed and presented. Publications related to the work discussed in this dissertation are:

1) P. Maheshwari, V. Khilkevich, D. Pommerenke, "Application of Emission source microscopy to EMI source localization," to be published at the *IEEE Symposium on Electromagnetic Compatibility*, 2014.
2) X. Jiao, P. Maheshwari, V. Khilkevich, J. Drewniak, D. Pommerenke, "EMI mitigation with lossy material at 10 GHz," to be published at the *IEEE Symposium on Electromagnetic Compatibility*, 2014.
3) P. Maheshwari, V. Khilkevich, D. Pommerenke "Emission Source Microscopy to EMI source localization" to be submitted to the *IEEE Transactions on Electromagnetic Compatibility*.

Other publications resulting from doctoral studies are:

4) (Book chapter) D. Pommerenke and P. Maheshwari, "Soft fail and PCB Design Measures," in System Level ESD Co-design" to be published by Wiley.
5) S. Sedigh, A. Faza, J. Lin, P. Maheshwari, N. Jarus, "Modelling of Cyber-Physical Systems: A Survey of Challenges and Methods," submitted to ACM Computing Surveys (under revision).
6) Z. Li, P. Maheshwari, D. Pommerenke, "Measurement Methodology for Field Coupled Electrostatic Discharge Induced Soft Errors in Integrated Circuits,"

submitted to the *IEEE Transactions on Electromagnetic Compatibility* (under revision).

7) P. Maheshwari, S. Sedigh, D. Pommerenke, "Software-Based Detection of Electrostatic Discharge Effects," submitted to the *IEEE Transactions on Instrumentation and Measurement.*

8) P. Maheshwari, V. Khilkevich, D. Pommerenke, "Directional Noise Injection for IC Immunity Testing Using an Amplified Dual-Channel Arbitrary Waveform Generator," submitted to the *IEEE Transactions on Electromagnetic Compatibility.*

9) H. Hui, P. Maheshwari, D. Pommerenke, "Development of EM-Field Probing Systems to Allow for Manual Scanning with Capability of Near Field and ESD Current Spreading Visualization" to be submitted to the *IEEE Transactions on Instrumentation and Measurement.*

10) Sabatini, N. Jarus, P. Maheshwari, S. Sedigh, "Software instrumentation for failure analysis of USB host controllers," in Proc. of the *IEEE International Instrumentation and Measurement Technology Conference (I2MTC), pp.* 1109-1114, 6-9 May 2013.

11) P. Maheshwari, T. Li, J.-S. Lee, B.-S. Seol, S. Sedigh, and D. Pommerenke, "Software-based analysis of the effects of electrostatic discharge on embedded systems," *in Proc. of 35th Annual IEEE Computer Software and Applications Conference (COMPSAC)*, pp. 436-441, 18-22 July, 2011.

12) P. Maheshwari, B.-S. Seol, J.-S. Lee, J.-D. Lim, S. Sedigh, and D. Pommerenke, "Software-based instrumentation for localization of faults caused by electrostatic discharge," *in Proc. of the 13th International Symposium on High-Assurance Systems Engineering (HASE)*, pp. 333-339, 10-12, Nov, 2011.

13) Radchenko, D. Pommerenke, G. Chen, P. Maheshwari, S. Shinde, V. Pilla, Y. R. Zheng, “Real-time bridge scour monitoring with magneto-inductive field coupling,” in *Proc. of SPIE Smart Structures and Materials and Nondestructive evaluation and health monitoring*, 2013.

14) P. Maheshwari, B. Orr, H. Gossner, D. Pommerenke, W. Stadler, “A systematic method for determining soft-failure robustness of a subsystem,” in *Proc. of the 35th Electrical Overstress/Electrostatic Discharge Symposium (EOS/ESD),* pp. 1-8, 2013.

15) H. Hui, P. Maheshwari, A. Radchenko, D. Pommerenke, “EM radiation estimation using an automatic probe position recording system coupled to hand scanning,” in *Proc. of the IEEE International Symposium on Electromagnetic Compatibility (EMC), pp. 348-353, 5-9 Aug. 2013*.

16) V. Pilla, P. Maheshwari, T. Li, D. Pommerenke, J. Maeshima, H. Shumiya, T. Yamada, K. Araki, “Investigation of the ESD induced clock disturbances in portable electronics products,” in *Proc. of the IEEE International Symposium on Electromagnetic Compatibility (EMC),* pp. 343-347, 5-9 Aug. 2013.

17) S. Yang, P. Maheshwari, V. Khilkevich, D. Pommerenke, “Coupling path visualization using a movable scatterer,” to be published at the *IEEE Symposium on Electromagnetic Compatibility*, 2014.

18) H. Hui, P. Maheshwari, D. Pommerenke, “Optical Tracking-based EM-field probing system for EMC Near-field manual scanning,” to be published at the *IEEE Symposium on Electromagnetic Compatibility*, 2014.

19) B. Orr, P. Maheshwari, D. Pommerenke, H. Gossner, W. Stadler, "Analysis of current sharing in large and small-signal IC pin models," to be published at the *IEW EOS/ESD Symposium,* 2014.

20) X. Ren, P. Maheshwari, Y-.J. Zhang, V. Khilkevich, J. Fan, "The Impact of Near-field scanning size on the accuracy of Far-field Estimation," to be published at the *IEEE Symposium on Electromagnetic Compatibility,* 2014.

21) G. Li, V.A.K. Prabhala, A. Saxena, Q. Wang, P. Maheshwari, D. Pommerenke, "A Methodology to Generate a Time-varying Adjustable Wave Impedance inside a TEM Cell," to be published at the *IEEE Symposium on Electromagnetic Compatibility*, 2014.

2. EMISSION SOURCE MICROSCOPY METHOODLOGY

2.1. INTRODUCTION TO ALGORITHM

In this algorithm, the scanning hardware is used to move the antenna on the scanning plane and it collects fields over a synthetic aperture. Conventional Synthetic aperture radar uses migration algorithms like back-propagation to migrate the fields from scanning plane back to the source. The fields are compensated by adding a time delay or phase shift corresponding to the back-focused distance for time domain or frequency domain respectively. The focused image on the source plane provides the information about the sources of radiation. So, this method can be used to scan outside the reactive near-field and locate the EMI sources. Here the translation can be achieved by transforming the fields from spatial to spatial frequency domain. On the source plane, they are back converted to spatial domain to retrieve the focused image. For this transformation a computationally efficient algorithm such as Fast Fourier Transform (FFT) is utilized.

2.2. ANALYTICAL FORMULATION OF THE ESM ALGORITHM

To apply the ESM algorithm, the fields from the sources are scanned on a planar surface approximately a few wavelengths from the DUT in order to be outside the DUT's reactive near-field and to achieve the minimal effect of the probe on the DUT's fields. Observing the field pattern on the scan plane yields very limited information about the location and number of radiation sources.

The scanned fields on the observation plane can be expanded using plane wave spectrum theory, which states that any monochromatic but otherwise arbitrary wave can

be represented as a superposition of plane waves travelling in different directions with different amplitudes, but of the same frequency. According to [24], the electric field intensity in a source-free region on a plane (x, y, 0) can be represented as a superposition of plane waves in the form of Fourier transform,

$$\boldsymbol{E}(x, y, 0) = \frac{1}{4\pi^2} \int_{-\infty}^{\infty} \int_{-\infty}^{\infty} \boldsymbol{f}(k_x, k_y) e^{-j(k_x x + k_y y)} dk_x dk_y \tag{1}$$

where $\boldsymbol{f}(k_x, k_y, 0)$ is the plane wave spectrum of $\boldsymbol{E}(x, y, z)$ as given by,

$$\boldsymbol{f}(k_x, k_y) = \int_{-\infty}^{\infty} \int_{-\infty}^{\infty} \boldsymbol{E}(x, y\, , 0)\, e^{j(k_x x + k_y y)} dxdy \tag{2}$$

Here k_x and k_y are the spectrum wavenumbers in x and y directions, respectively. It can be shown that the spectrum of the field on any plane parallel to $(x, y, 0)$ can be found using,

$$\boldsymbol{f}(k_x, k_y, z) = \boldsymbol{f}(k_x, k_y) * e^{-jk_z z} \tag{3}$$

where $k_z = \sqrt{{k_0}^2 - {k_x}^2 - {k_y}^2}$ is the z component of the propagation vector, $k_0 = 2\pi/\lambda$ is the free-space wavenumber, and λ is the wavelength of the active source radiation.

Therefore, if the field on the plane (x, y, z) is known, the field on the plane $(x, y, 0)$ can be found using,

$$E(x, y, 0) = \boldsymbol{F}^{-1}[\boldsymbol{F}\{\boldsymbol{E}(x, y, z)\} * e^{jk_z z}] \tag{4}$$

where z is vertical distance of the scanning plane from the source plane, **F** and $\mathbf{F}^{-1}$ are forward and reverse Fourier transform operators, respectively.

Equation 4 allows back-propagation of the field on one plane to another. If the fields are measured on the plane parallel to the antenna aperture or any other planar source, (4) then the fields on the source plane can be reconstructed. In reality, the fields are not available in the form of continuous functions, as in (1) and (2), but instead are sampled at discrete locations. In the case of uniform sampling, (4) would result in discrete rather than continuous Fourier transforms. Equation (4) serves as the basis of the ESM algorithm.

2.2.1. Test of Methodology on Analytical Data. For the analytical validation, dipoles can be used as excitation sources and 2D ESM algorithm can be applied to determine the location of the dipoles on the source plane. For this purpose, the dipoles are placed at a distance of few wavelengths away from the scanning plane to be out of the reactive near-field of the dipoles. Here the field components are calculated over the x-z plane as shown in Figure 2.1. The fields due to dipole on the scanning plane can be calculated using the following equations from [24],

$$H_{\Phi} = j\frac{kI_o l sin\theta}{4\pi r}\left[1+\frac{1}{jkr}\right]e^{-jkr} \quad (5)$$

$$H_r = H_\theta = 0$$

$$E_r = \eta\frac{kI_o l cos\theta}{2\pi r^2}\left[1+\frac{1}{jkr}\right]e^{-jkr}$$

$$E_\theta = j\eta\frac{kI_o l sin\theta}{4\pi r}\left[1+\frac{1}{jkr}+\frac{1}{(kr)^2}\right]e^{-jkr}$$

$$E_\Phi = 0$$

Here for example, two dipoles are located at (-100, 0, 0) mm and (100, 0, 100) mm respectively. The excitation frequency of the dipoles is 10 GHz. The E-field components calculated at 10 cm away from the source plane. As seen the pattern is nothing but an inference pattern created due to the linear superposition of fields from each of the dipoles. By observing this pattern no information about the location of the dipoles can be derived.

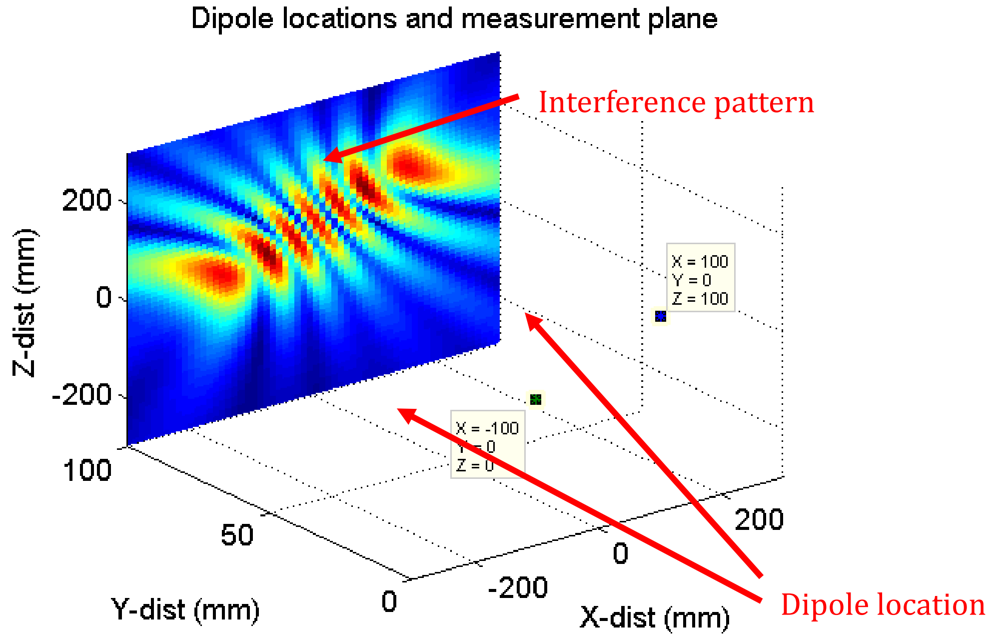

Figure 2.1 Dipole location and measurement plane.

The field components are measured over the rectangular grid on the scanning plane. The rectangular scanning plane is divided into a grid of N x M points. The sampling points on the scanning grid are chosen to be less than λ/2 apart in order to satisfy the Nyquist spatial sampling criterion [26]. Although the Nyquist rate is not required for reconstruction, uniformly sampled data at the Nyquist rate reduces the overall complexity of the reconstruction algorithm. [28]. At grid sample points, the tangential electric field components E_x and E_y are measured.

The measured E-field component is then converted to frequency domain using Equation 4. It can also be computed using a computationally efficient algorithm such as FFT. Also the x and y axis are converted to spatial frequency domain as k_x and k_y.

$$\Delta k_x = \frac{2*\pi}{\Delta x.N} \quad (6)$$

$$\Delta k_y = \frac{2*\pi}{\Delta y.N}$$

$$k_x = (0: length(x)) * \Delta k_x$$

$$k_y = (0: length(y)) * \Delta k_y$$

In the spectral domain it is multiplied by phase terms corresponding to the distance we want to translate the image as shown in Equation (3). To reconstruct the spatial image of the target, an inverse Fourier transform can be applied on the shifted spectrum image as given in Equation (4). By reconstruction the fields at different distance from the source plane, we can observe the focusing effect of the ESM algorithm as shown in Figure 2.2. As shown in Figure 2.2, on the dipole plane, correct location of dipoles can be determined. Here the spatial scanning resolution is 2 mm and resolution of reconstructed image is 1.6 cm. Also dipoles at the placed at different heights with respect to the scanning plane and focusing can be performed at different heights. Here dipole 2 is kept at a distance of 2 wavelength from the scanning plane instead of 2.5 wavelength kept for dipole 1. The exact locations for dipole 1 and dipole 2 would be (-100, 15, 0) mm and (100, 0, 100) mm respectively. By reconstruction the fields at different distance from the source plane, we can observe the focusing effect of the ESM algorithm as shown in Figure 2.3. As seen, due to the dipoles being at different heights they come in focus at different focusing plane. Here the spatial scanning resolution is 2 mm and resolution of reconstructed image is 1.6 cm.

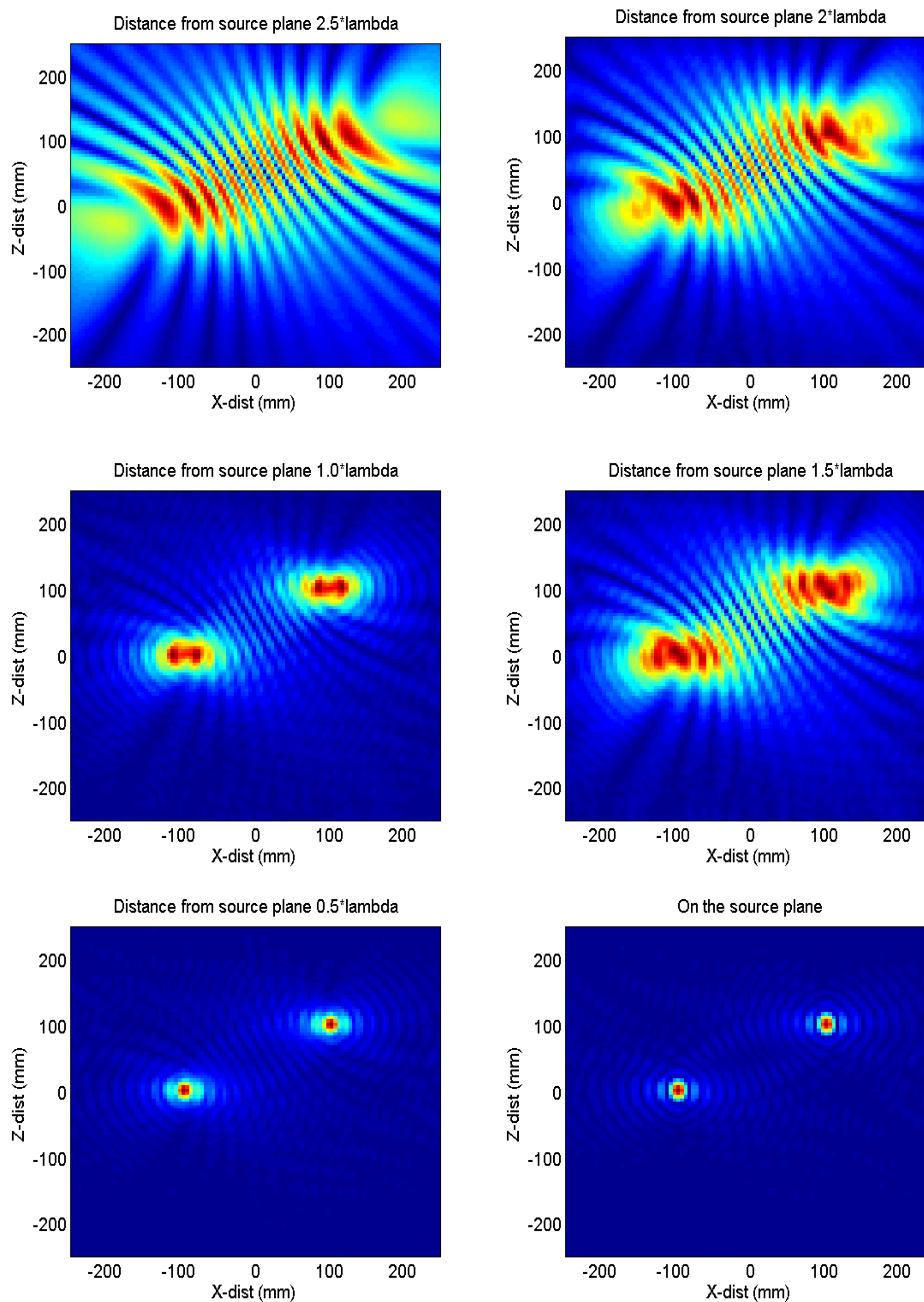

Figure 2.2 Focused fields at different distance with dipoles at same height.

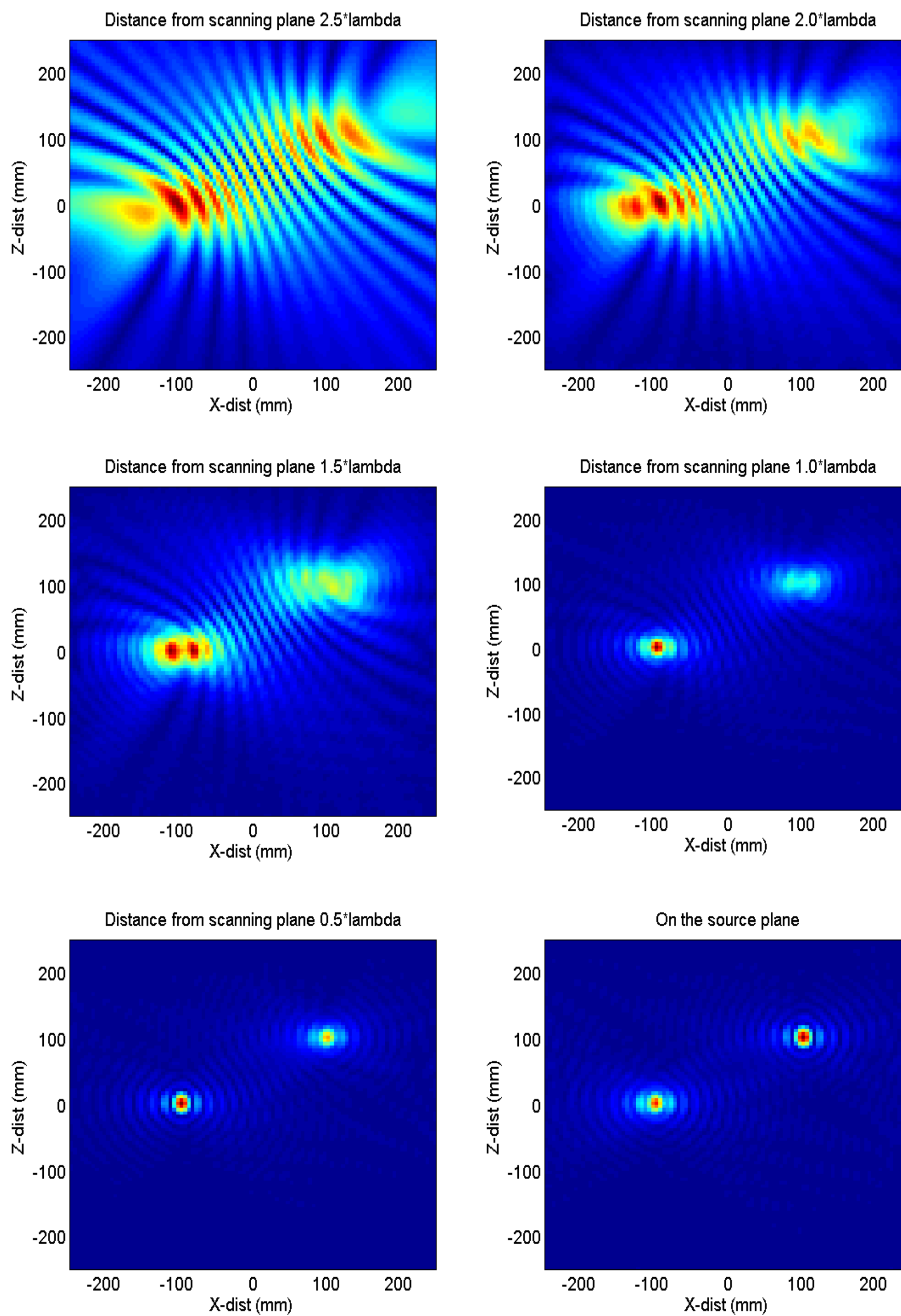

Figure 2.3 Focused fields at different distances with dipoles at different height.

2.2.2. Resolution of Reconstructed Image. The resolution of scanning, height of the scanning plane, and frequency of operation affects the final resolution of the reconstructed image. From optics [26] [27], the numerical aperture of the lens is given as,

$$N.A. = n * \sin\theta \quad (7)$$

where 'n' is the refractive index of the medium, and 'θ' is one-half of the aperture angle in radians, as shown in Figure 2.4.

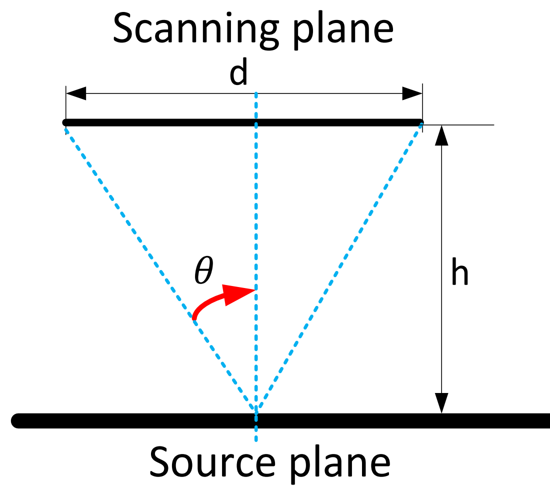

Figure 2.4 Aperture angle given by the span of the scan plane.

Here 'd' represents the length of the smallest side in meters, and 'h' is the height of the scanning plane above the DUT in meters. Based on the numerical aperture in (5), the resolution of the reconstructed image can be given as,

$$R = \lambda/(2 * N.A.) \tag{8}$$

This limits the resolution that can be achieved in the reconstructed image. For an infinitely wide scanning plane, the aperture angle would be 90 degrees, and with air as the medium, the maximum N.A. would be 1. This limits the maximum resolution to λ /2. This limitation does not allow distinguishing the sources placed closed as compared to wavelength at lower frequencies. So the method is mainly useable above 5 GHz for real-cases. For example, with a scanning area of 0.5m x 0.5m, at 10 GHz frequency at a height of 10 cm away from PCB plane, the numerical aperture is given as,

$$N.A. = 1 * \left(\frac{0.25}{0.2693}\right) = 0.9283$$

$$Resolution = \frac{0.03}{2 * 0.9283} = 0.0162\ m$$

2.2.3. Suppression of Evanescent Wave Component. The spectrum of the near-field of electromagnetic fields consists of two different portions, the evanescent waves and the propagating waves [44]. The component of the wave in z direction $\boldsymbol{K_z}$ is given as,

$$k_z = \sqrt{k^2 - {k_x}^2 - {k_y}^2}\ if\ \ {k_x}^2 + {k_y}^2 \le k^2 \tag{9}$$

$$k_z = -j\sqrt{{k_x}^2 + {k_y}^2 - k^2}\ if\ \ {k_x}^2 + {k_y}^2 > k^2 \tag{10}$$

Equation (9) indicates propagating waves, whereas equation (10) indicates a decaying wave or evanescent wave. For the far-field region, most of the energy is concentrated within the circle of $k_x^2 + k_y^2 = k_0^2$ in spectrum domain; which means most of the wave components are just propagating waves. Antennas have a near reactive field region in which the dominant energy is composed of inhomogeneous or evanescent waves that decay exponentially with distance from the aperture. This field may extend up to length of a wavelength away from the surface of the DUT.

These waves can be separated in the spatial frequency domain and are completely suppressed during the reconstruction of the images. This allows to visualize area on the PCB with are contributing to far-field.

2.3. PLANAR NEAR-FIELD TO FAR-FIELD TRANSFORMATION

Using the FFT method, far-field can be computed from near-field data [24],[33]. This transformation is from planar surface to spherical far-field. The plane wave spectrums $f_x(k_x, k_y)$ and $f_y(k_x, k_y)$ can be calculated from sampled near-field data using the 2D Fourier transforms,

$$f_x(k_x, k_y) = \int_{-b/2}^{b/2} \int_{-a/2}^{a/2} E_{xa}(x', y', z' = 0) e^{-j(k_x x' + k_y y')} dx' dy' \quad (11)$$

$$f_y(k_x, k_y) = \int_{-b/2}^{b/2} \int_{-a/2}^{a/2} E_{ya}(x', y', z' = 0) e^{-j(k_x x' + k_y y')} dx' dy' \quad (12)$$

where $E_{xa}(x', y', z' = 0)$ and $E_{ya}(x', y', z' = 0)$ are represent the tangential components of electric field on the scanning plane.

The spatial resolution ($\Delta x,\ \Delta y$) and spectral resolution ($\Delta k_x, \Delta k_y$) can be related by the following equations,

$$\Delta k_x = \frac{2\pi}{M\Delta x}$$

$$\Delta k_y = \frac{2\pi}{N\Delta y}$$

where the scanning grid size is given by M × N points.

Using stationary phase method, the far-field **E** can be written as,

$$E_\theta(r,\theta,\varphi) \approx j\frac{ke^{-jkr}}{2\pi r}(f_x cos\varphi + f_y sin\varphi) \tag{13}$$

$$E_\varphi(r,\theta,\varphi) \approx j\frac{ke^{-jkr}}{2\pi r}cos\theta(-f_x sin\varphi + f_y cos\varphi) \tag{14}$$

To determine the far-field angles from k_x and k_y, following relation is used,

$$k_x = ksin\theta cos\varphi \tag{15}$$

$$k_y = ksin\theta sin\varphi \tag{16}$$

Next the angles are converted from spherical to Cartesian coordinates to plot the computed fields. The far-field components E_x, E_y and E_z in the far-field are a function of theta, rho and phi.

The total radiated power can be computed from the radiation intensity which can be given as,

$$U(\theta,\phi) = \frac{r^2}{2\eta}\left[|E_\theta(r,\theta,\phi)|^2 + \left|E_\phi(r,\theta,\phi)\right|^2\right]. \tag{17}$$

The total radiated power can be obtained by integration of the radiation intensity over as the hemisphere as,

$$P_{rad} = \oiint_{\Omega} U \, d\Omega = \int_0^{2\pi} \int_0^{\pi} U \, sin\theta \, d\theta \, d\phi \qquad (18)$$

where dΩ is the element of solid angle = sinθ dθ dϕ.

2.4. MASKING OF INDIVIDUAL SOURCES

The main goal of masking of individual sources after applying the ESM transformation is to estimate the contribution of individual sources to far-field radiation. This will help in identifying the dominant source contributing to far-field radiation. For this firstly the fields are scanned at a distance of few wavelengths from the DUT. The measured fields can then be back-propagated back to source plane using the ESM algorithm. Using image processing techniques, individual sources can be masked. This will allow observing isolated sources on the source plane. Using the near-field to far-field transformation discussed in the previous section, the contribution of this isolated source to far-field radiation can be estimated. The algorithm is shown in Figure 2.5.

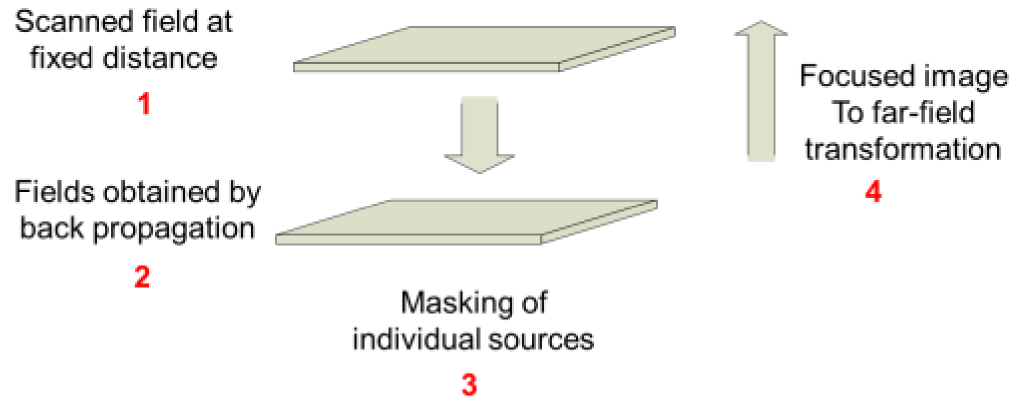

Figure 2.5 Algorithm to determine individual source contribution.

The process is shown using an example of three dipoles placed on the source plane. On the scanning plane, the dipoles create an interference pattern. The fields on the scanning plane with respect to the source plane are shown in Figure 2.6.

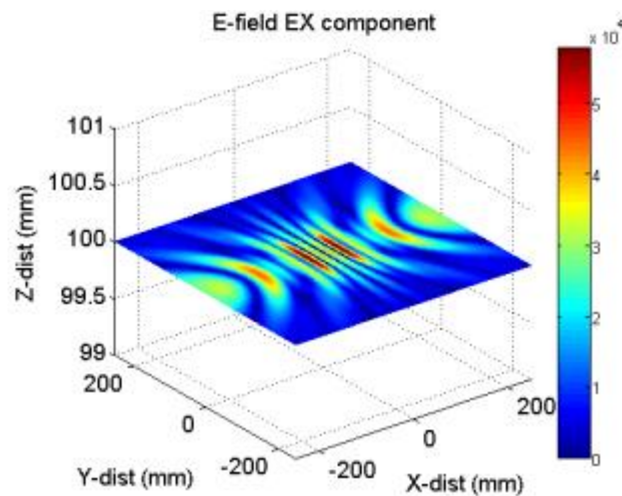

Figure 2.6 Recorded fields on the scanning plane.

Here after calculating the fields on the scanning plane, zero padding is applied in both the dimensions to increase the scanning area. Zero-padding is performed on the scanned data to increase the aperture angle. Large value of k_x and k_y axis in the spectrum domain leads to increased spectral discretization in the far-field, thus improving the accuracy of the results [33]. The scanned field after the zero padding is shown in Figure 2.7. Using the 2D ESM algorithm, the fields can be reconstructed on the source plane, thus locating the 3 dipole sources, as shown in Figure 2.8.

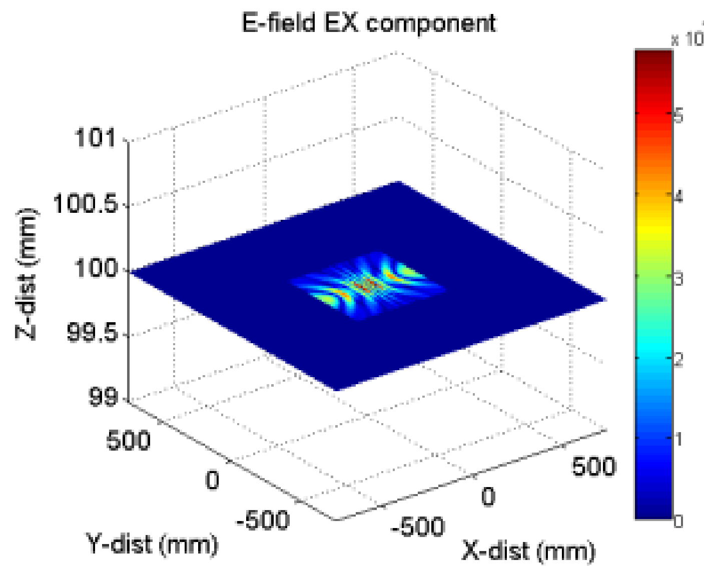

Figure 2.7 Recorded fields after zero padding.

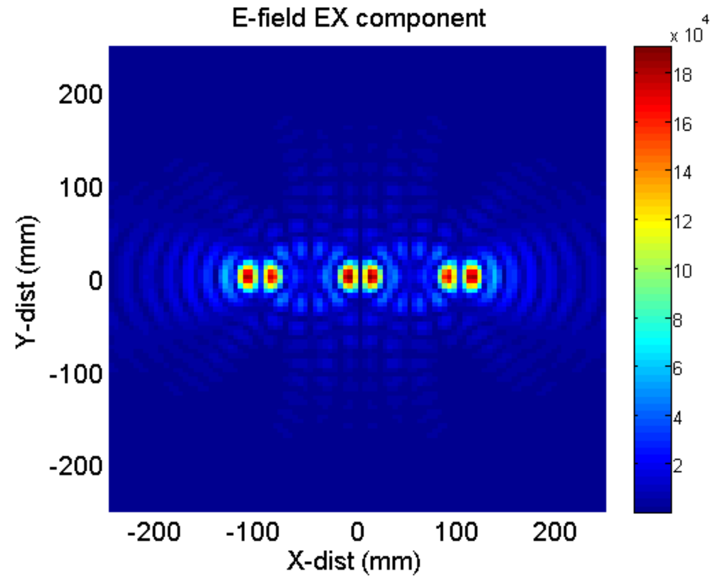

Figure 2.8 Focused fields on the source plane.

The far-field computed from reconstructed planar fields on the source plane containing the three dipoles using equation (9) is shown in Figure 2.9 . Also the far-field computed using the analytical solution for dipoles (Figure 2.10) show a good agreement between the results. The maximum Etheta component calculated from the far-field obtained from reconstructed fields is 85.5dB whereas from the analytical solution is 85.08db. This is done to validate the far-field computation using the FFT method.

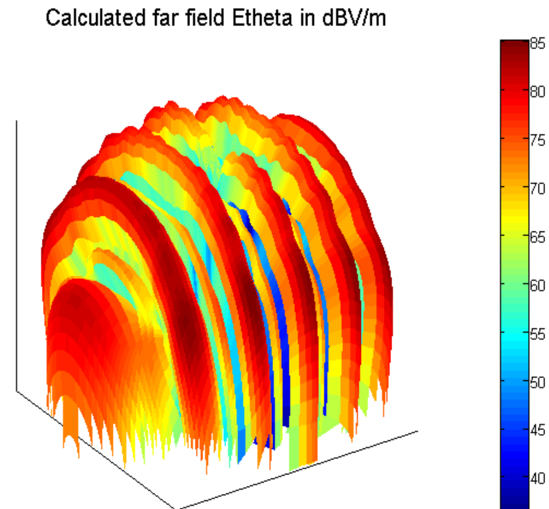

Figure 2.9 Calculated far-field pattern obtained from recorded fields.

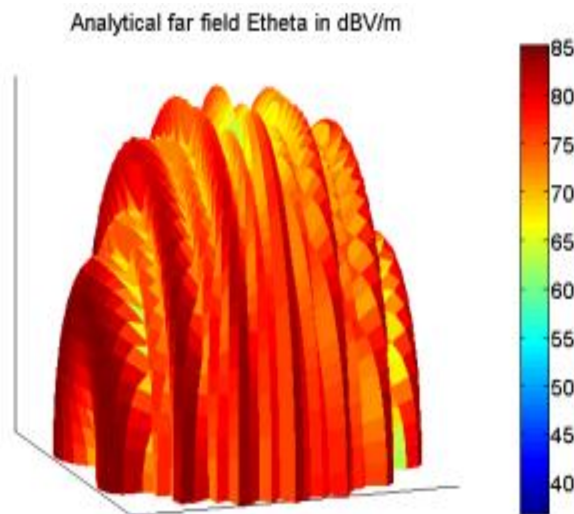

Figure 2.10 Calculated far-field pattern obtained analytical formula.

For masking, a window can be applied over the source of interest such that other sources are masked. The results before and after masking are shown in Figure 2.11.

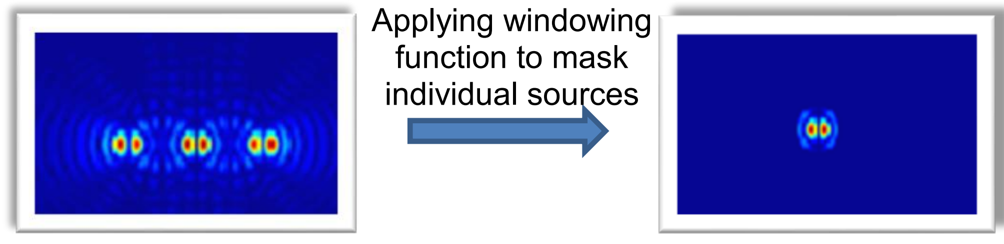

Figure 2.11 Masking sources to isolate only one dipole source.

Far-field calculated from masked image is shown in Figure 2.12. The maximum Etheta component from the calculated far-field from masked image is 73.80 dB whereas using analytical solution for a single dipole is 75.96 dB.

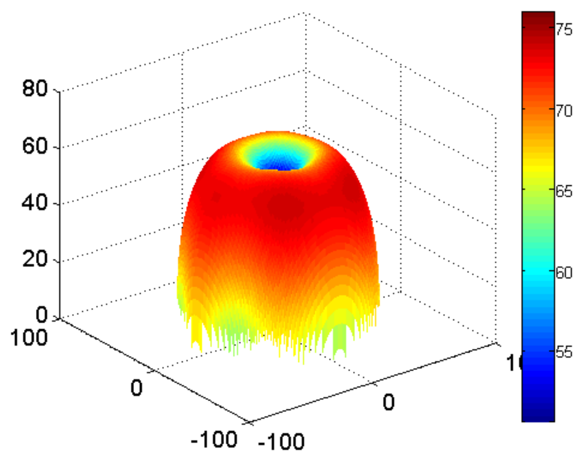

Figure 2.12 Far-field from masked image (containing single dipole contribution).

This shows that the after masking the far-field can be accurately estimated to determine the contribution to far-field from individual sources.

2.5. ACCURACY ESTIMATION IN ESM ALGORITHM

The different errors that affect the results in the ESM algorithm are as follows:

2.5.1. Measurement Plane Truncation. Truncation of the scan plane in spatial domain due to measurement limitation is same as using a rectangular window function in the spatial domain. This would lead to convolution with a 2D sinc-like function in the spatial spectrum domain. This leads to observation of ripples around the sources in the reconstructed fields on the source plane. To reduce the effect of the truncation of the scan plane, windowing function can be applied before transformation to spectrum domain to force the edge to taper to zero. A plot of aperture angle versus the maximum error in the magnitude of the far zone Etheta component is shown in Figure 2.13. Here the height of the scanning system is kept constant at 1.5*lambda and scanning step is lambda/6. As seen the error in the calculated far-field E-field component is below 0.1 dB only for aperture angle greater than 80 degrees.

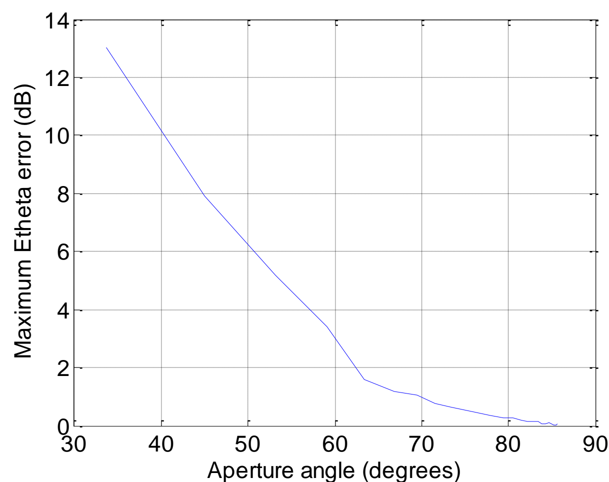

Figure 2.13 Error in the far-field Etheta component versus aperture angle.

2.5.2. Cable Amplitude and Phase Variation. Due to the mechanical flexing of the cable connected` to the scanning antenna with the probe movement throughout the scanning plane, leads to the change in the insertion loss of the cable. Also temperature changes during the measurement can lead to variation in amplitude and phase of the measured fields on the scanning plane. Typically for a good quality cable at high frequency, the change in the insertion loss is less than 1%.

2.5.3. Non-Planarity of the Measurement Surface. The movement of the scanning probe may not be completely parallel to the plane of the DUT. This introduces a biased phase error in the measurement. This biased error would lead to error in location of the source.

2.5.4. Scan Plane Distance Uncertainty. The exact height is scanning antenna above the source plane is usually measured using a tape measure. Also the phase center of the antenna and the source on the DUT might not be known. This may lead to an uncertainty in the scan plane distance above the DUT. Although this would not introduce an error in the far-field parameters or the total radiated power but would lead to error in the maximum amplitude of the focused fields. To quantify the error, a dipole source is scanned with a scanning plane at a height of 2*lambda. The spatial scanning resolution is kept as lambda/6. Next height of the scanning plane is changed and the difference in the maximum amplitude of the focused field and the focused fields from different distance is recorded. The plot of the maximum error in the focused field as compared to the scan plane distance uncertainty expressed in percentage is shown in Figure 2.14. As shown the error is below 0.1 dB for scan plane distance uncertainty less than 12 percent.

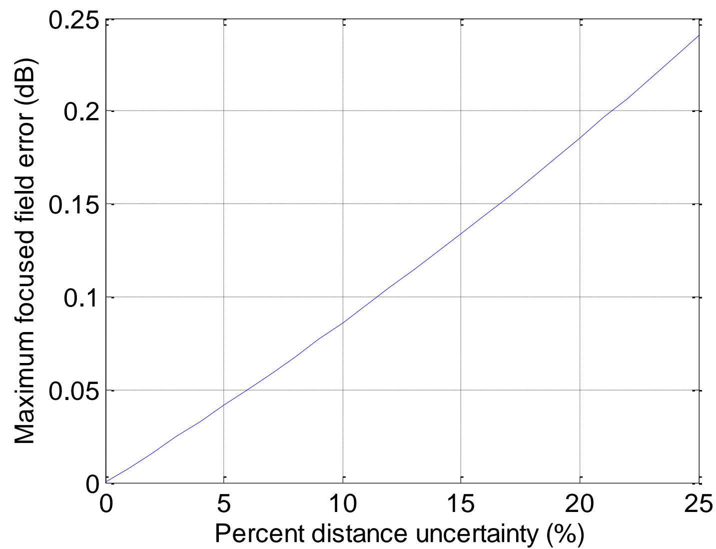

Figure 2.14 Error in the maximum amplitude of the focused field with scan plane distance uncertainty.

2.5.5. Uncorrelated Phase Error. Due to the measurement environment and non-linearity of the measurement components, random phase noise is introduced in the measurement. This noise in the scanned fields can propagate to the focused fields and can destroy the reconstructed fields, such that source location cannot be determined. An experiment is performed with two dipoles orientated in the z direction are placed on the source plane placed at (0, 0, 0) m and (-0.1, 0, 0) m respectively. The scan height is kept as 1.5*lambda and the spatial scanning resolution is lambda/6. Different percentage of the phase noise as compared to the maximum phase is introduced in the scanned data and it is focused back on the source plane. The error in the maximum amplitude of the focused fields is recorded for different percent of random phase added and plotted as shown in Figure 2.15 and Figure 2.16.

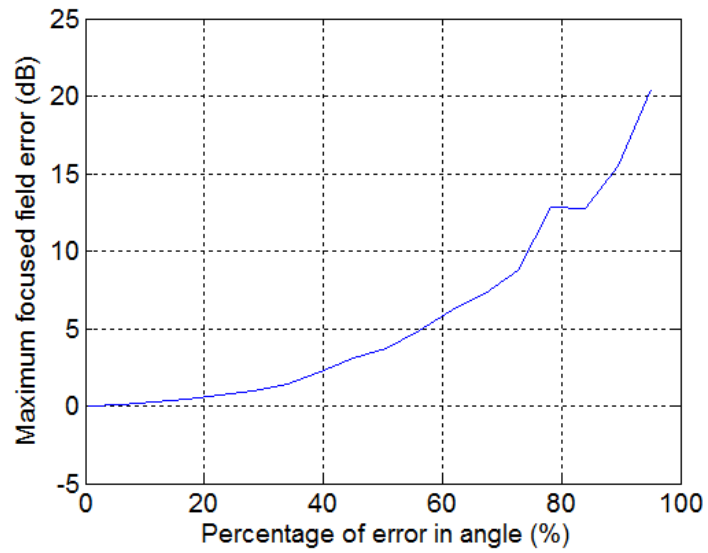

Figure 2.15 Error in the maximum amplitude of the focused E_x field with addition of random phase variations.

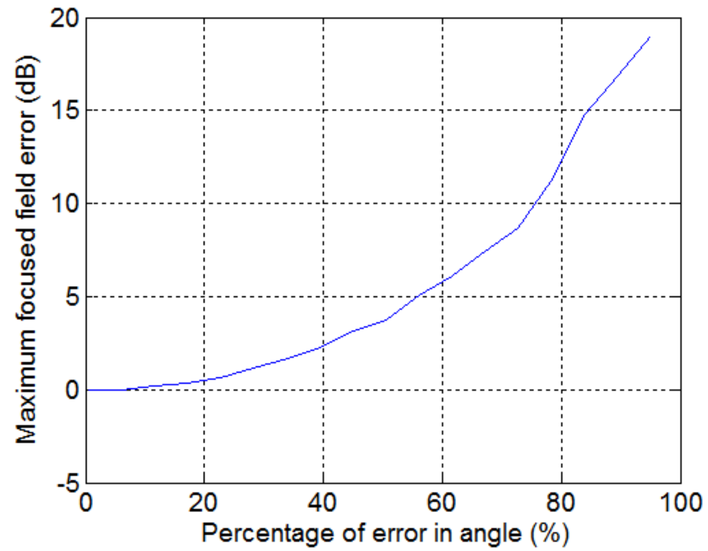

Figure 2.16 Error in the maximum amplitude of the focused E_y field with addition of random phase variations.

3. VALIDATION OF METHODOLOGY

3.1. SIMULATION ON A CUSTOM PCB

To test the usefulness of the proposed method for EMC applications a custom PCB with several patch antennas and transmission lines is built. Figure 3.1 shows the full wave model of the PCB built in CST Microwave studio full-wave simulation tool [32]. The model is built to be able to compare the experimental results to the simulation results. The patches and traces on the PCB can be excited and terminated individually or simultaneously. The PCB is 254 mm x 152 mm in size, having two 20 mm x 20 mm center feed patches. The smaller patches are 10 mm x 10 mm in size. The ground plane is set as PEC in the simulation and the dielectric material between the trace/patches and ground plane is FR-4 with ε_r = 4.3. The thickness of the dielectric layer is 1.6 mm. The copper layer thickness is 0.035 mm. The simulation is performed at 8.2 GHz using the time-domain solver.

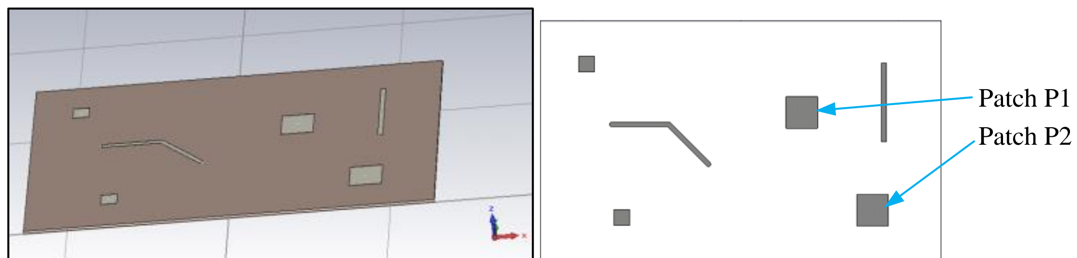

Figure 3.1 Model of Custom PCB.

The return loss of the large patch is plotted against frequency as shown in Figure 3.2. Here the first resonance of the patch is seen around 6.79 GHz.

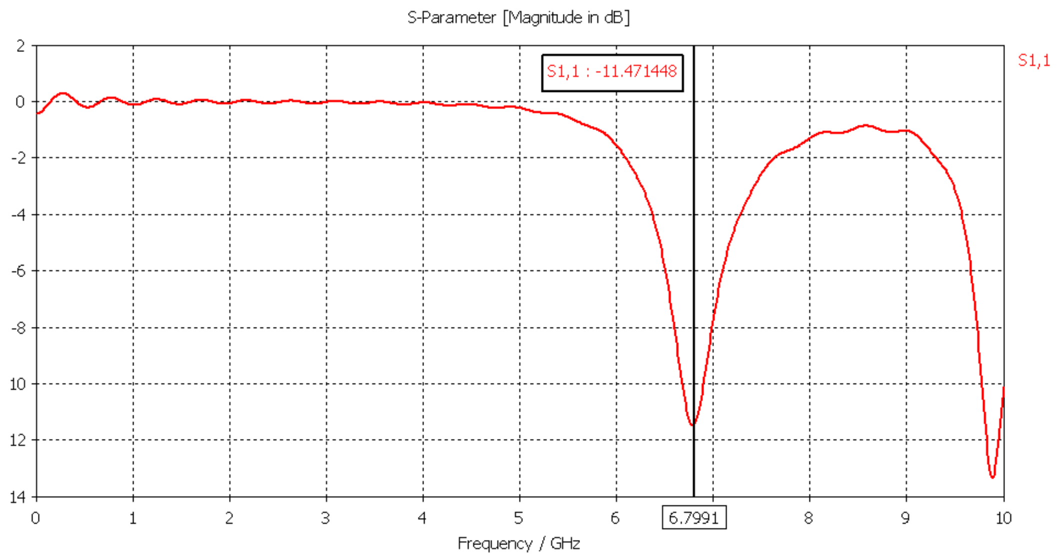

Figure 3.2 Simulated return loss of the larger patches.

For validation of the method, the patches P1 and P2 are excited simultaneously. The input excitation power to each patch is set as 1W. The excitation frequency is kept as 8.2 GHz. This is done to be able to use X-band (8.2-12.4 GHz) open-ended waveguides for measurement purpose. Using the time-domain simulation in CST, the tangential electric fields E_x and E_y are recorded at different heights above the above the DUT in the X-Y plane.

The recorded fields magnitude and phase for E_x and E_y field components at electric fields are obtained from simulation results at 1.5*lambda (54.9 mm) height and plotted as shown in Figure 3.3 and Figure 3.4.

The spatial scanning resolution of the rectangular plane is kept at lambda/6 (6.1 mm), which is enough to satisfy the Nyquist spatial sampling criteria at this frequency. The image of the PCB is overlapped and aligned with the image of the recorded fields to observe the underlying physical sources of radiation. As seen from Figure 3.3 and Figure 3.4, no particularly useful information about the source of radiation can be obtained by observing the fields.

The ESM algorithm is then applied to the recorded fields and the fields are back-propagated to the source plane. The reconstructed E_x and E_y fields magnitude and phase on the PCB plane are shown in Figure 3.5 and Figure 3.6. As seen, the two patches that form the radiation structure can be localized to their correct locations.

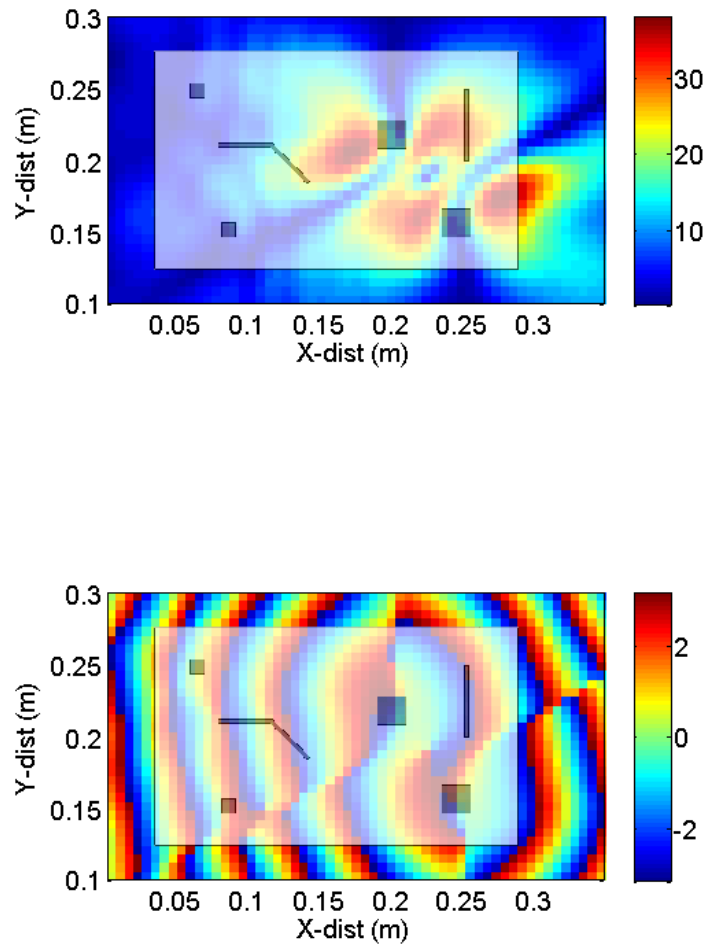

Figure 3.3 Recorded E_x magnitude (V/m) field and phase (rad) from simulation.

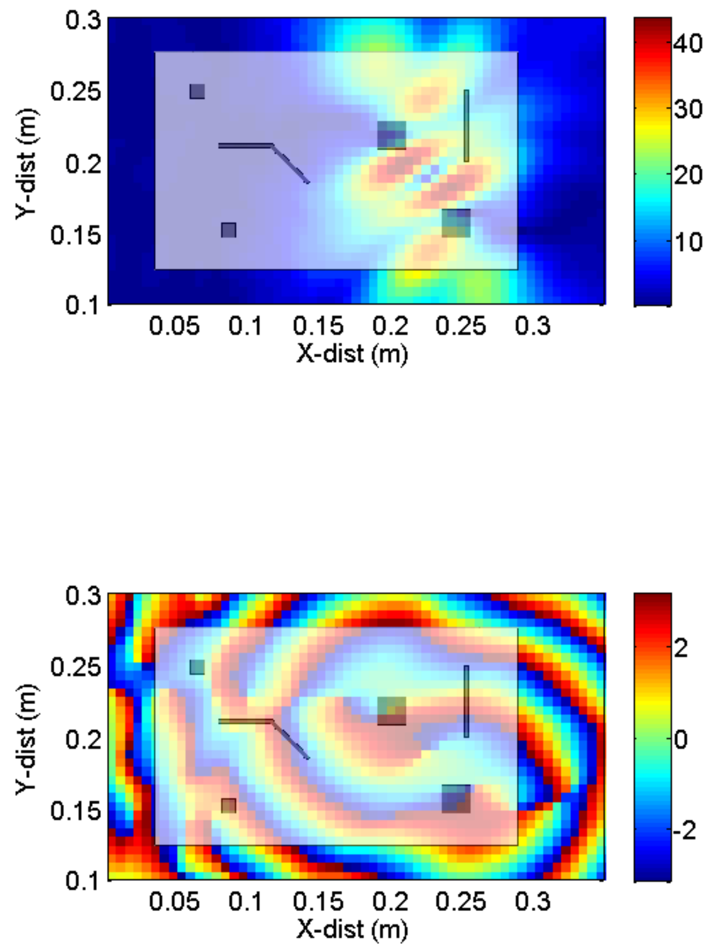

Figure 3.4 Recorded E_y magnitude (V/m) and phase (rad) field from simulation.

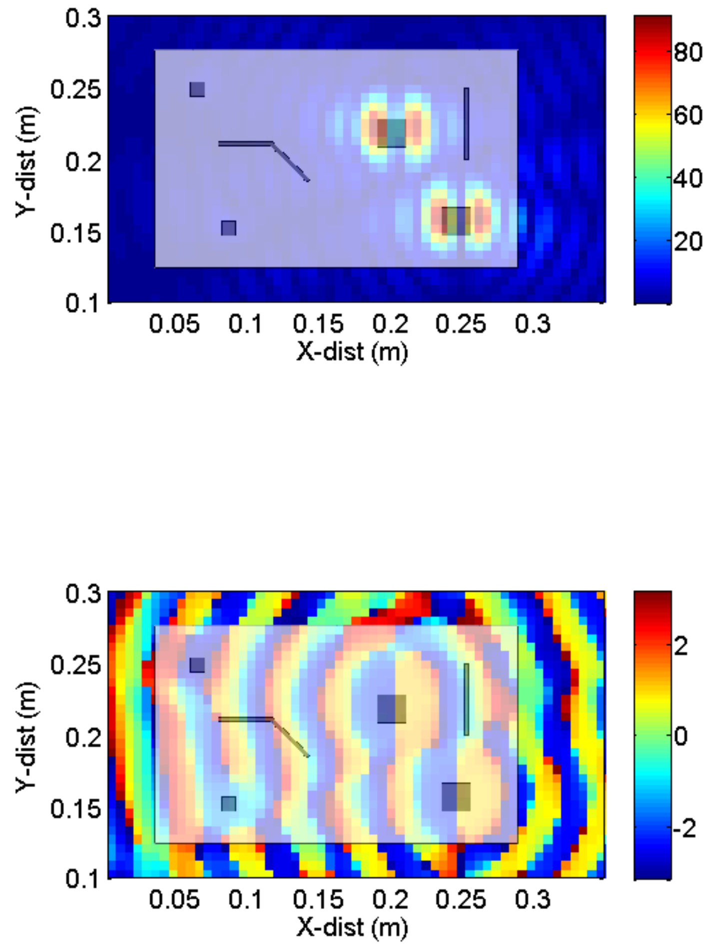

Figure 3.5 Reconstructed E_x field magnitude (V/m) and phase (rad) on the source plane.

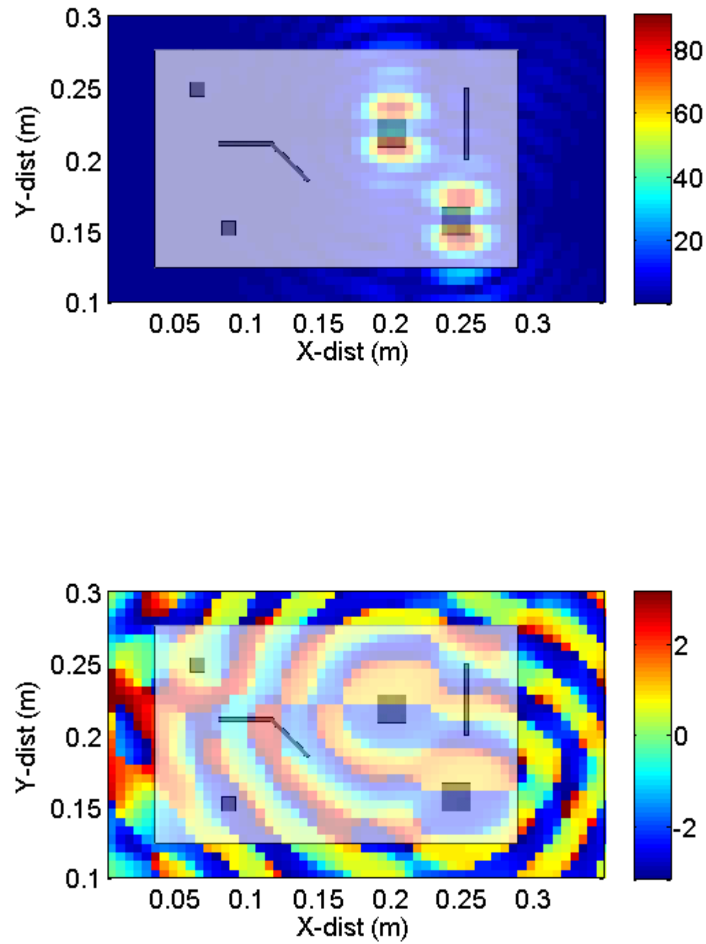

Figure 3.6 Reconstructed E_y field magnitude (V/m) and phase (rad) on the source plane.

The resolution of the reconstructed image is 1.9 cm. The ripples in the reconstructed images around the sources are actually diffraction rings, common to the optical microscopy.

The next step is to perform near-field to far-field and compare far-field parameters with the full wave simulation results. Using the NF-FF discussed in the previous section, the 3D E-field pattern is calculated from the focused complex tangential E-field components reconstructed on the PCB plane. The 3D E-field pattern plot in dBV/m for the Etheta component is shown in Figure 3.7. Also the far-field pattern from obtained from CST full wave simulation of the PCB is as shown in Figure 3.8. The far-field distance is kept as 1 m and it is calculated at 8.2 GHz.

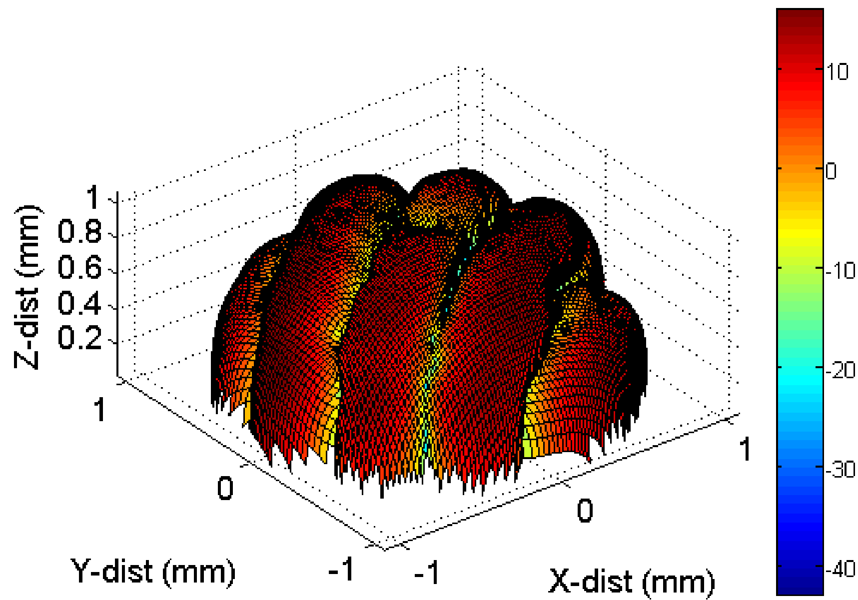

Figure 3.7 3D Far-field pattern using Etheta component (dBV/m) of the DUT calculated from NF-FF transform of the focused fields on PCB plane.

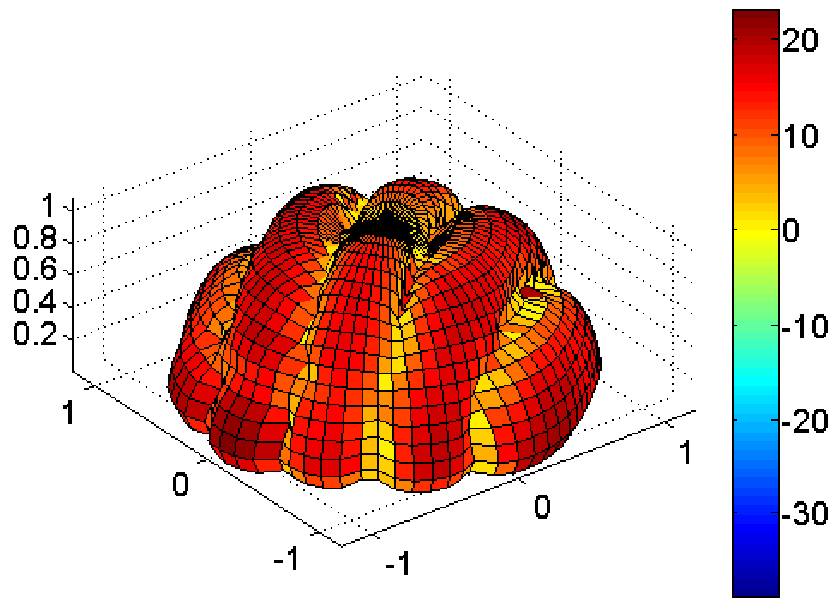

Figure 3.8 3D Far-field pattern using Etheta component (dBV/m) of the DUT obtained from full wave simulation tool.

The maximum value of the Etheta component from the calculated results is 15.84 dBV/m and from full wave simulation is 20.28 dBV/m. The difference for the discrepancy in the maximum values of E-field component is as a result of the radiation pattern of the DUT when both the patches are excited simultaneously. The radiation pattern in linear scale obtained from full wave simulation is shown in Figure 3.9.

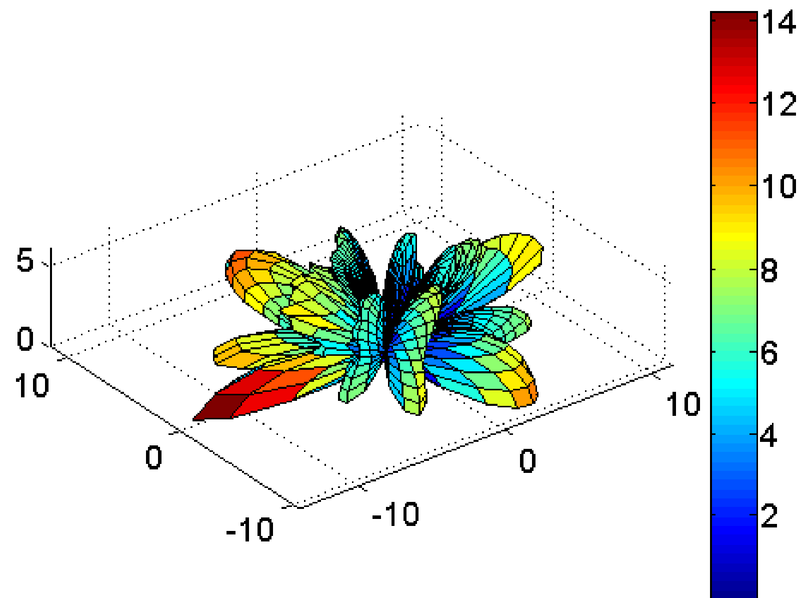

Figure 3.9 3D Far-field pattern using Etheta component (V/m) obtained from CST.

As seen in the pattern, the maximum occurs for large oblique elevation angles. In the ESM methodology, the fields are only obtained only a planar surface above the DUT at few wavelengths away. For field component at large oblique elevation angles to be calculated accurately using the NF-FF algorithm, the near fields are required to be computed over the entire Huygen box surrounding the DUT [34]. By performing the near-field scan on five sides of the box surrounding the DUT, the maximum value of the Etheta component for the above DUT can be obtained close to the full-wave simulation results. The aperture angle also determines the accuracy of the far-field when calculating the far-field from near-field as discussed in [33]. The aperture angle needs to be greater than 80 degrees to ensure the accuracy of FFT used for far-field calculation within 1dB

from full-wave simulation results. For 2D patterns also, only field components greater than 75 degrees are compared to the full wave simulation results. The 2D cross sections of the calculated NF-FF far-field pattern for different constant phi and theta angles are compared with full wave simulations results. The 2D cross-sections of far-field pattern for Etheta component in V/m are as shown in Figure 3.10 - Figure 3.13. As seen the calculated far-field patterns match closely with the full-wave simulation results.

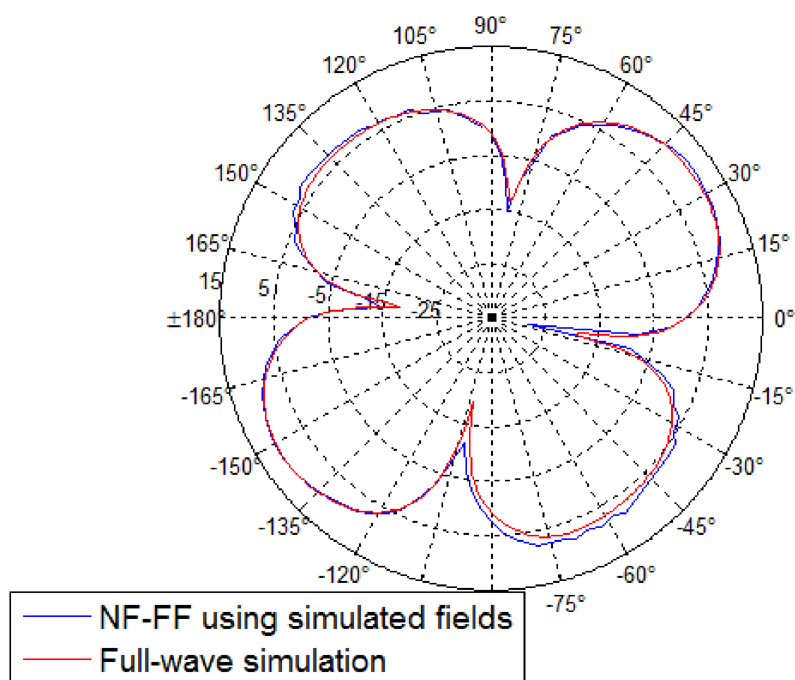

Figure 3.10 Constant Theta = 20 pattern using Etheta component (dBV/m).

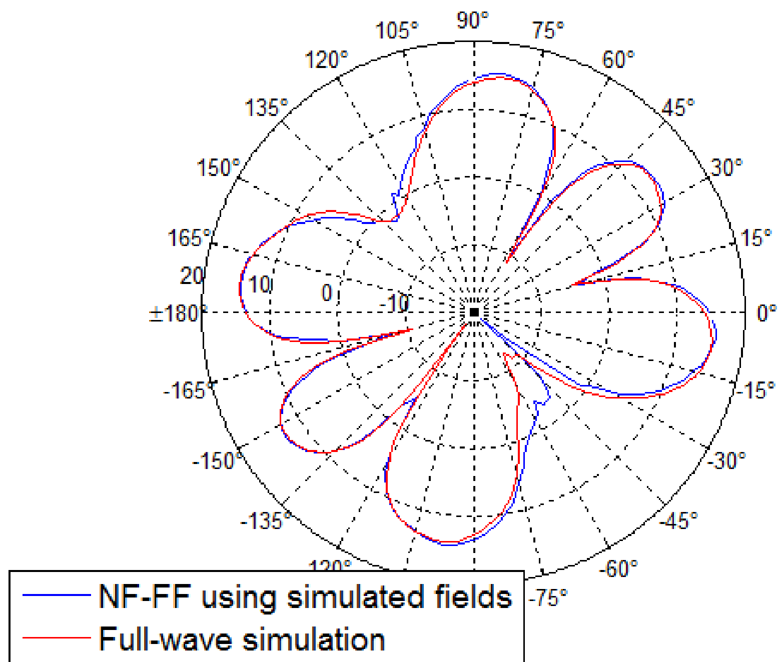

Figure 3.11 Constant Theta = 45 pattern using Etheta component (dBV/m).

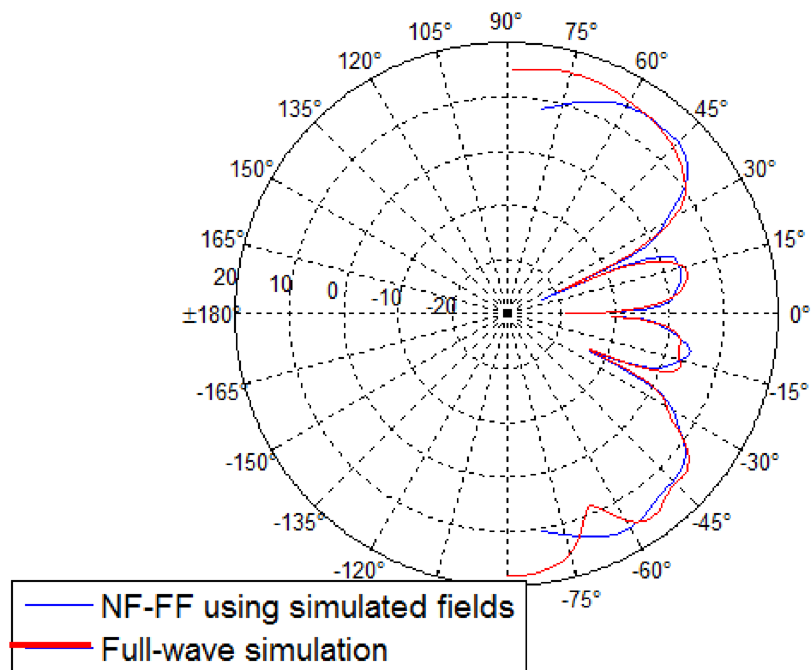

Figure 3.12 Constant Phi = 0 pattern using Etheta component (dBV/m).

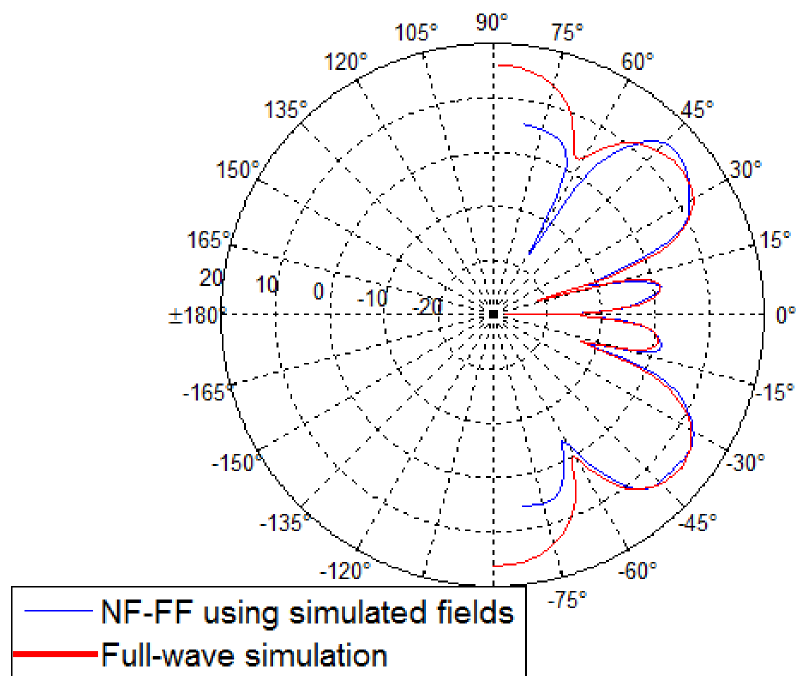

Figure 3.13 Constant Phi = 90 pattern using Etheta component (dBV/m).

The next step to validate the results is to calculate the total radiated power using the method discussed in the previous section. The total radiated power obtained from full wave simulation is 21.02 dBm. The total radiated power computed using the calculated far-field pattern is 20.99 dBm which is within 1 dB of the full wave simulation results. This shows that the total radiated power for a DUT can be predicted with sufficient accuracy by performing a planar near-field measurement and applying ESM methodology.

3.2. DETERMINING FAR-FIELD CONTRIUBTION FROM INDIVDUAL SOURCES

To determine the contributions from individual sources that are identified using the ESM algorithm, individual sources needs to be kept active while suppressing radiation from all other individual sources as shown with the dipole example. To do this a mask is applied which suppress all other except the desired sources. Here in the PCB example, two patches are excited and identified using the ESM methodology. Here each individual source is alternatively masked and far-field contribution from the other one is computed. These results are compared with the full-wave simulation results with that particular individual source to be active.

Firstly the source corresponding to patch P2 is suppressed while the source corresponding to patch P1 is kept active. This is done by applying a windowing function to the patch of appropriate size as shown in Figure 3.14 and Figure 3.15. The size of the window should be large enough to cover the hot spot identified by the ESM algorithm corresponding to the radiation source.

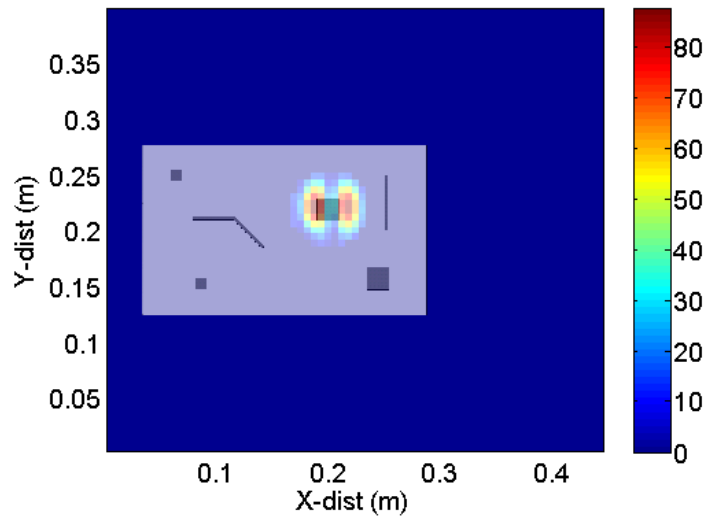

Figure 3.14 Reconstructed E_x field magnitude (V/m) with source corresponding to patch P1 kept active.

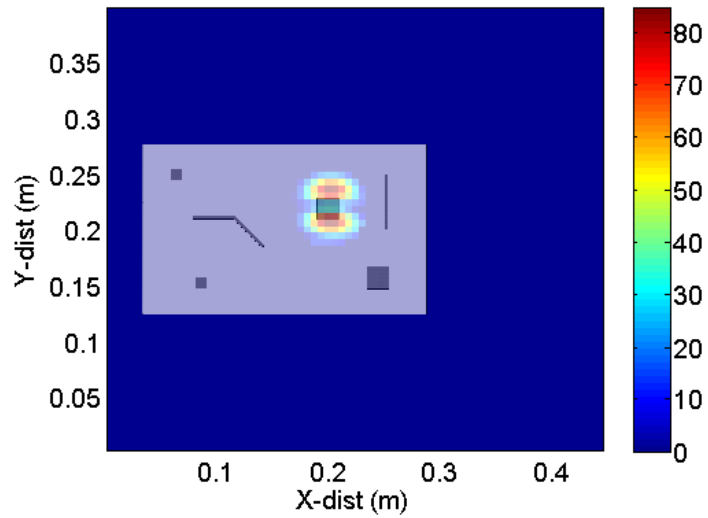

Figure 3.15 Reconstructed E_y field magnitude (V/m) with source corresponding to patch P1 kept active.

Next NF-FF transformation is performed for the masked field images and far-field pattern is obtained. This data is compared with the full wave simulation with only patch P1 as active. The computed 3D far-field plots for Etheta component in dBV/m are shown in Figure 3.16, whereas Figure 3.17 shows the far-field pattern obtained from full wave simulation. The maximum value of Etheta component using calculation is 8.9 dBV/m whereas using full wave simulation is 15.08 dBV/m. The total radiated power computed using the calculated far-field is 16.30 dBm whereas the one obtained from full-wave simulation is 17.98 dBm which is within 1 dB of the calculated results. This shows that the TRP can be predicted with good accuracy even after the sources are masked. So the contributions from individual sources can be calculated.

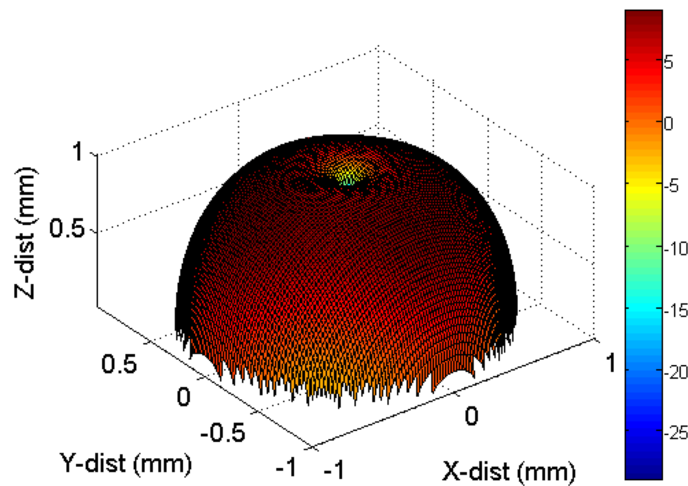

Figure 3.16 3D Far-field pattern for Etheta component (dBV/m) of the DUT obtained from masked fields.

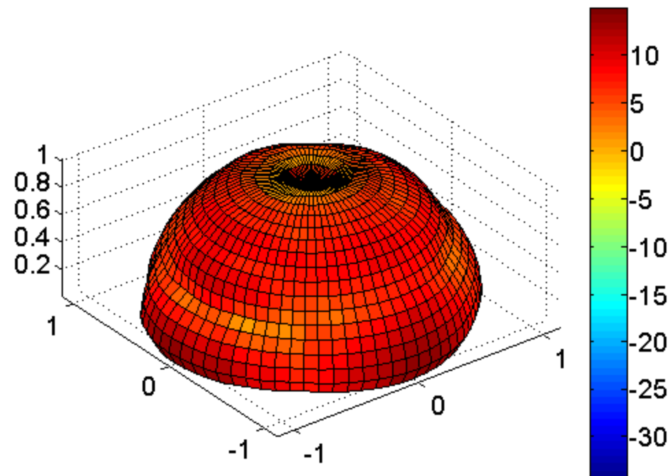

Figure 3.17 3D Far-field pattern for Etheta component (dBV/m) of the DUT obtained from CST with only Patch P1 active.

Next 2D patterns of the far-field plot calculated from NF-FF of the masked focused field image and compared with the results of full-wave simulation. The results for Etheta component 2D pattern for various constant theta and phi in V/m are plotted in Figure 3.18, Figure 3.19, Figure 3.20 and Figure 3.21.

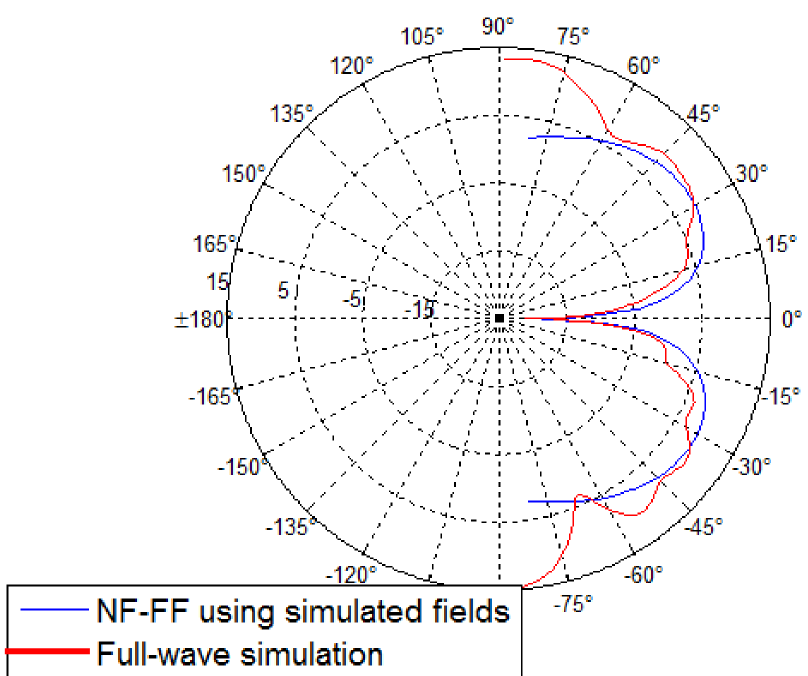

Figure 3.18 Constant Phi = 0 pattern using Etheta component (dBV/m).

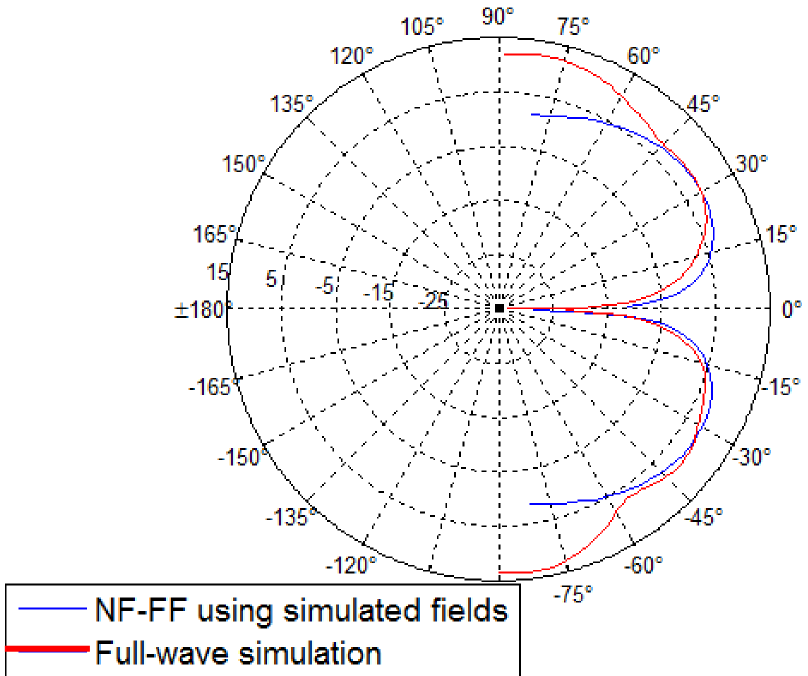

Figure 3.19 Constant Phi = 90 pattern using Etheta component (dBV/m).

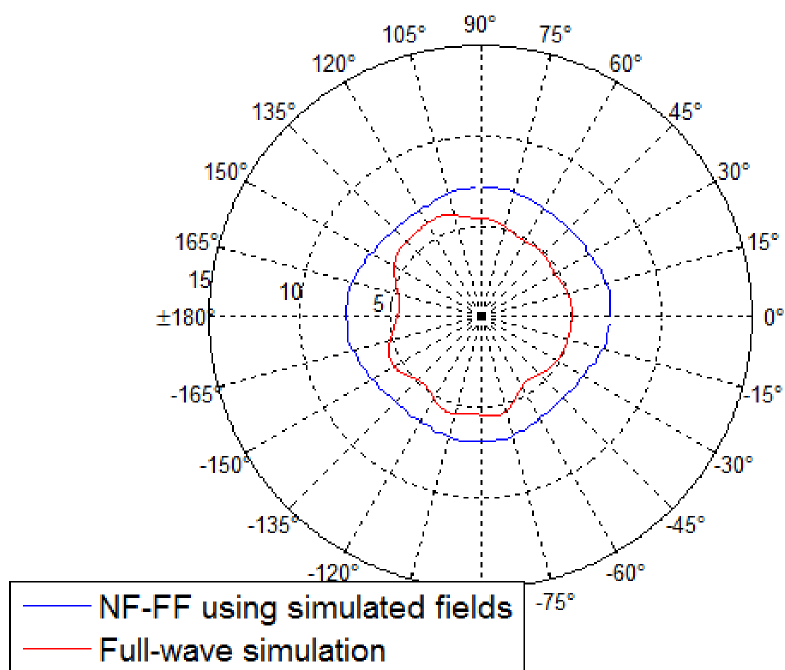

Figure 3.20 Constant Theta = 20 pattern using Etheta component (dBV/m).

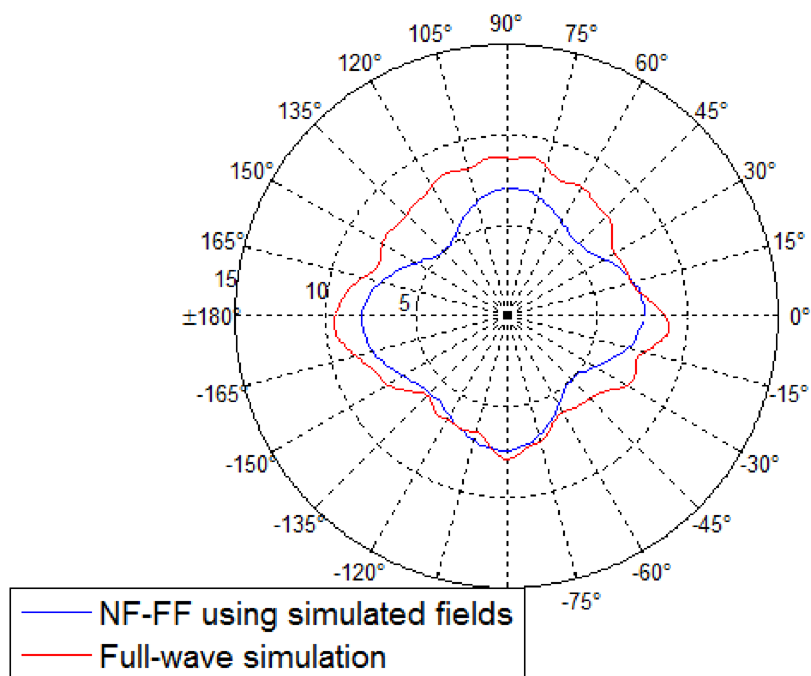

Figure 3.21 Constant Theta = 45 pattern using Etheta component (dBV/m).

Similar results are obtained by masking the source corresponding to Patch P1 and keeping the source corresponding to Patch P2 active and comparing with full wave simulation results with only Patch P2 active. The results are shown in Figure 3.22 and Figure 3.23.

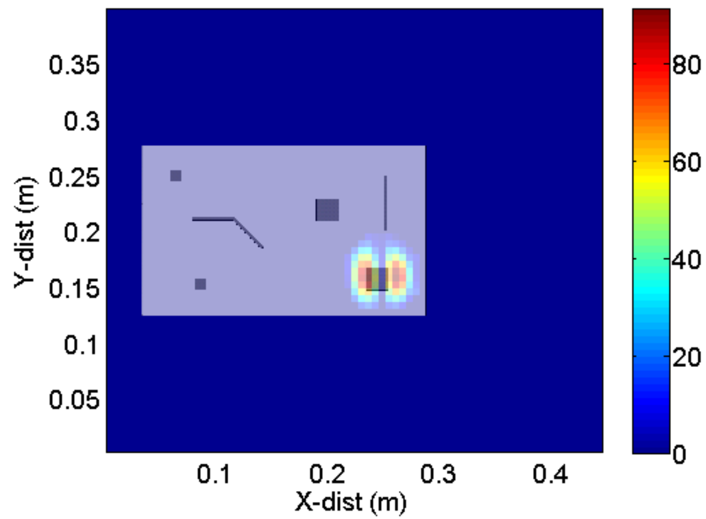

Figure 3.22 Reconstructed E_x field magnitude (V/m) with source corresponding to patch P2 kept active.

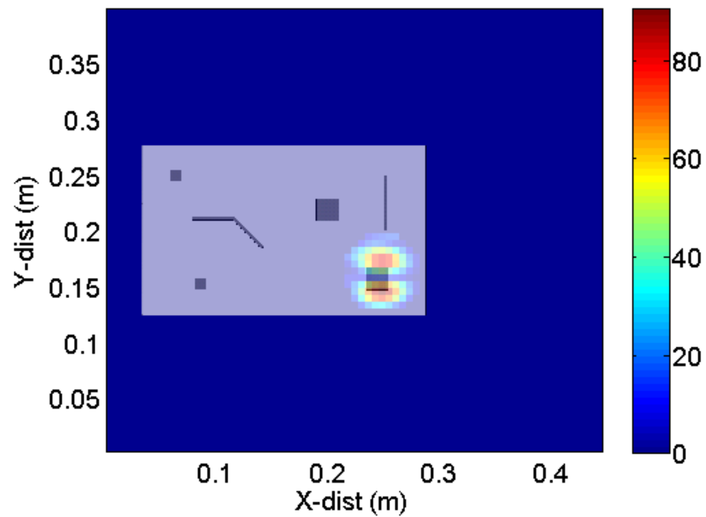

Figure 3.23 Reconstructed E_y field magnitude (V/m) with source corresponding to patch P2 kept active.

The computed 3D far-field plots for Etheta component in dBV/m are shown in Figure 3.24, whereas Figure 3.25 shows the far-field pattern obtained from full wave simulation. The maximum value of Etheta component using calculation is 8.9 dBV/m whereas using full wave simulation is 15.82 dBV/m. The TRP computed using the calculated far-field is 16.41 dBm whereas the one obtained from full-wave simulation is 17.98 dBm.

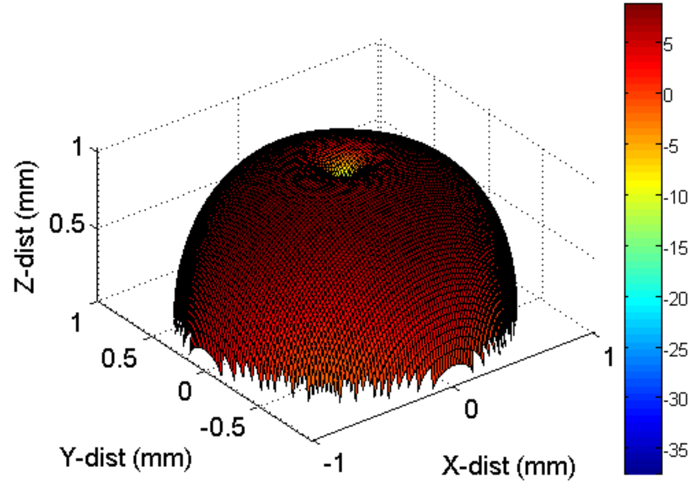

Figure 3.24 3D Far-field pattern for Etheta component (dBV/m) of the DUT obtained from masked fields.

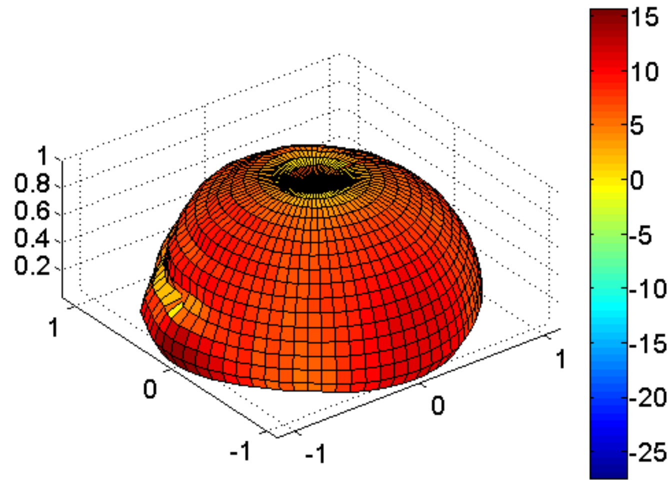

Figure 3.25 3D Far-field pattern for Etheta component (dBV/m) of the DUT obtained from CST with only Patch P2 active.

The results for Etheta component 2D pattern for various constant theta and phi in V/m are plotted in Figure 3.26 through Figure 3.29.

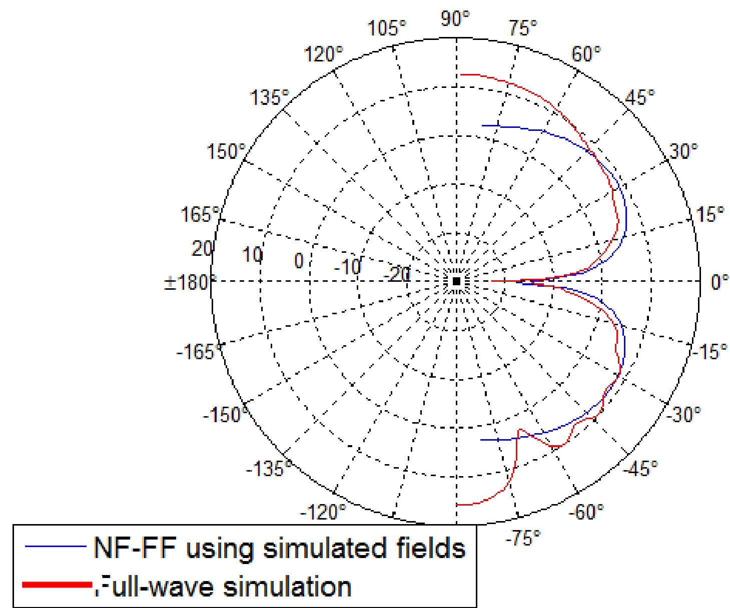

Figure 3.26 Constant Phi = 0 pattern using Etheta component (dBV/m).

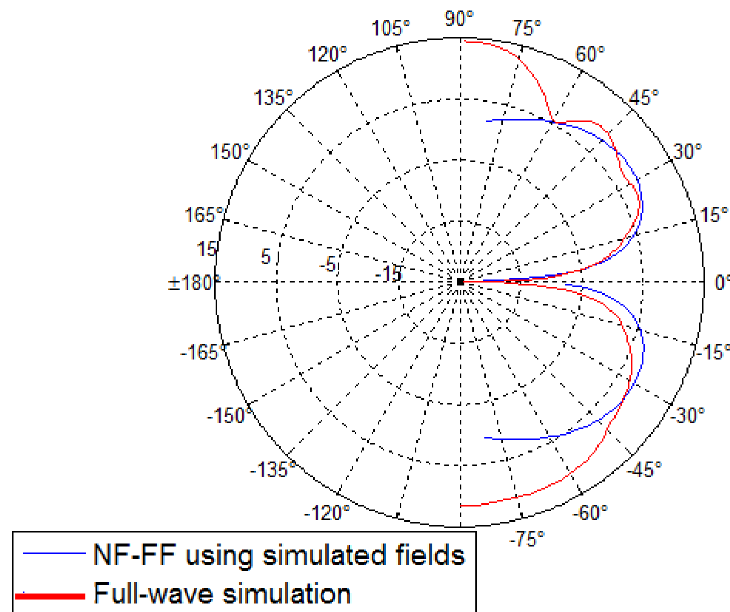

Figure 3.27 Constant Phi = 90 pattern using Etheta component (dBV/m).

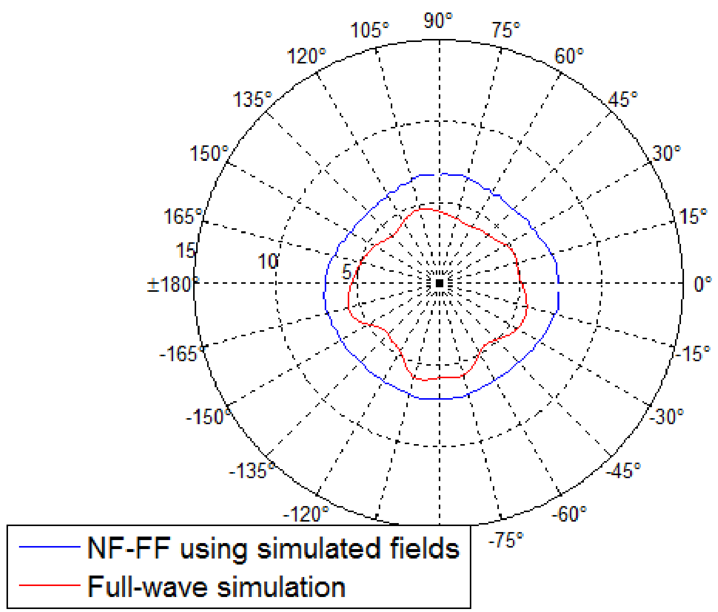

Figure 3.28 Constant Theta = 20 pattern using Etheta component (dBV/m).

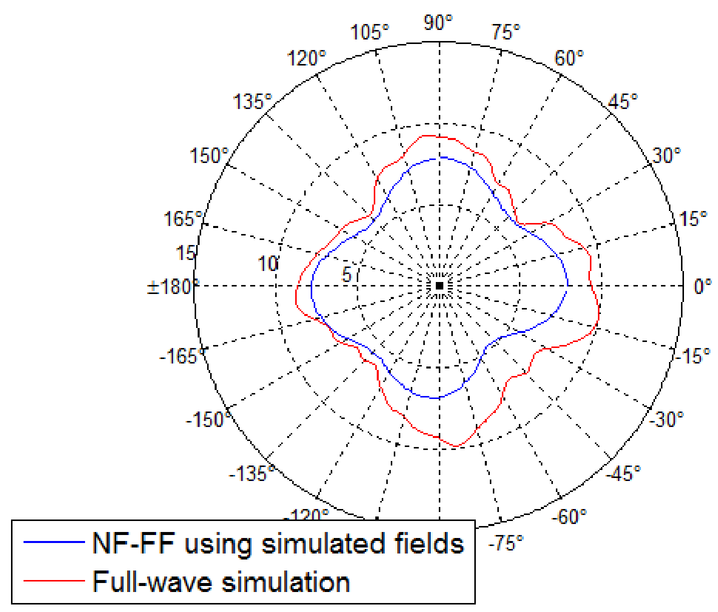

Figure 3.29 Constant Theta = 45 pattern using Etheta component (dBV/m).

3.3. EFFECT OF SCANNING PARAMETRS

It is important to determine the effect of different scanning parameters such the spatial scanning resolution and scan plane height on the reconstructed results, far-field parameters and the total radiated power. This will aid in selecting the criteria for scanning and will also help to indicate the accuracy of the results. For this experiment, only results from full wave simulation are used. This experiment aims to provide the optimal spatial scanning resolution and scan height parameters to achieve desired accuracy. The final accuracy of the measurement is not limited to these two parameters and may depend upon other factors. The results are calculated for spatial scanning resolution of λ/4, λ/6 and λ/8. The spatial scanning resolution is selected such that it satisfies the spatial Nyquist criteria. Also the scanned fields are obtained at different heights of lambda, 1.5×λ, 2×λ and 2.5×λ. The results are shown in Table 3.1, Table 3.2 and Table 3.3.

Table 3.1 Variation in maximum E-field tangential component (dbV/m).

Spatial resolution/ Scanning height	λ/4 (9.1 mm)	λ/6 (6.1 mm)	λ/8 (4.6 mm)
1×λ (36.6 mm)	42.7	42.9	43.0
1.5×λ (54.9 mm)	42.4	42.6	42.6
2×λ (73.2 mm)	42.2	42.1	42.2
2.5×λ (91.5 mm)	41.4	41.4	41.4

Table 3.2 Variation in maximum Etheta value (dbV/m).

Spatial resolution/ Scanning height	λ/4 (9.1 mm)	λ/6 (6.1 mm)	λ/8 (4.6 mm)
1×λ (36.6 mm)	19.5	19.5	19.5
1.5×λ (54.9 mm)	18.8	18.7	18.7
2×λ (73.2 mm)	18.7	18.8	18.7
2.5×λ (91.5 mm)	18.5	18.5	18.5

Table 3.3 Variation in maximum Total radiated power (dBm).

Spatial resolution/ Scanning height	λ/4 (9.1 mm)	λ/6 (6.1 mm)	λ/8 (4.6 mm)
1×λ (36.6 mm)	24.1	24.1	24.1
1.5×λ (54.9 mm)	23.48	23.5	23.4
2×λ (73.2 mm)	22.8	22.8	22.8
2.5×λ (91.5 mm)	22.1	22.1	22.1

As seen from the above results, it can be concluded that the change in the spatial scanning resolution beyond the spatial Nyquist criteria does not affect the E-field and far-field parameters significantly. The scanning resolution can be kept at minimum to minimize the scanning time. Other methods to minimize the scan time are discussed in future work section.

On the other hand the increase in the scanning height above the DUT reduces the aperture angle which leads to decrease in the accuracy of the far-field computation. The reason for reduction in the accuracy has been discussed in detail in section 3.2. For the maximum scan height a tolerance up to 2 dB in the different parameters can be expected.

3.4. MEASUREMENT METHODOLOGY AND RESULTS

3.4.1. Measurement Setup. For performing measurements, the total complex field needs to be measured thus requiring the magnitude as well as the phase data. Phase measurement can be achieved by using either a frequency domain or time domain approach. For measuring the custom PCB, the frequency domain approach is used with the setup as shown in Figure 3.30. More details about the different phase measurement methods are provided in section 4. A vector network analyzer (VNA) is used to measure the amplitude and phase of the scanned fields. One port of the VNA provides appropriate excitation source to the DUT. Another port is connected to the scanning antenna or probe to capture the response of the DUT. By performing a response measurement (S21), the amplitude and phase can be obtained. Further a transformation is required to obtain the exact field values from the probe output voltage. To validate the simulation results for the PCB with patches as shown before, a PCB with the same dimension is built. SMA connectors feed the patches from the bottom of the PCB. For measurement purpose, Port 1 of the VNA is used to excite the patches simultaneously. This is achieved by feeding the output of VNA to a 0 degree resistive splitter and then feeding the splitter output to the patches. The output RF power on the VNA is kept at 0 dBm. Port 2 is connected to an open-ended waveguide antenna mounted on the API 3-axis EMI scanning system [29] using a custom 3D printed probe holder. The scanning area is limited in size as compared to the simulation due to limited range of the scanning system. The setup for measurement is shown in Figure 3.30. The open-ended waveguide along with the probe holder can be seen in Figure 3.31.

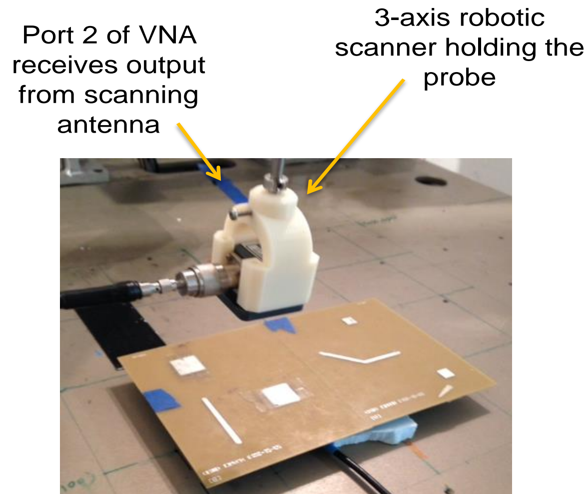

Figure 3.30 Measurement setup.

Figure 3.31 Open-ended waveguide used as scanning antenna.

The open ended waveguide is an X-band waveguide that operates from 8.2 – 12.4 GHz. It offers a wide beam width so it can collect maximum radiated energy at oblique angles too. Also it provides higher gain and closed form solution exist for calculating various parameters of the antenna. That makes it a suitable choice for performing ESM measurement.

3.4.2. Antenna Factor Compensation. While performing near-field measurement using non-ideal probes, probe correction is needed. If the measurement of the fields is performed in the far-field of the DUT, the use of only gain parameter for probe correction would yield sufficiently accurate results. In the ESM application, an open-ended waveguide is used for measuring fields in the near radiating region of the DUT. This requires the probe's far-field pattern be known. For a first order approximation only the gain can be used to perform probe compensation. The gain of the antenna can be either analytical calculated using close form solution for an open-ended waveguide [35][36] or can be obtained from the full wave model. The analytical gain of the waveguide is given as,

$$gain = 21.6 * f * w = 4.049$$

where w is the width of the large side, (here 22.86 mm), f is the frequency in GHz.

For determining the gain, a full wave simulation model of the waveguide is built and simulated to get antenna far-field parameters. The full wave model for the antenna in the top and side view is as shown in Figure 3.32. The length of the larger side of the aperture is 22.86 mm and the shorter side is 10.16 mm.

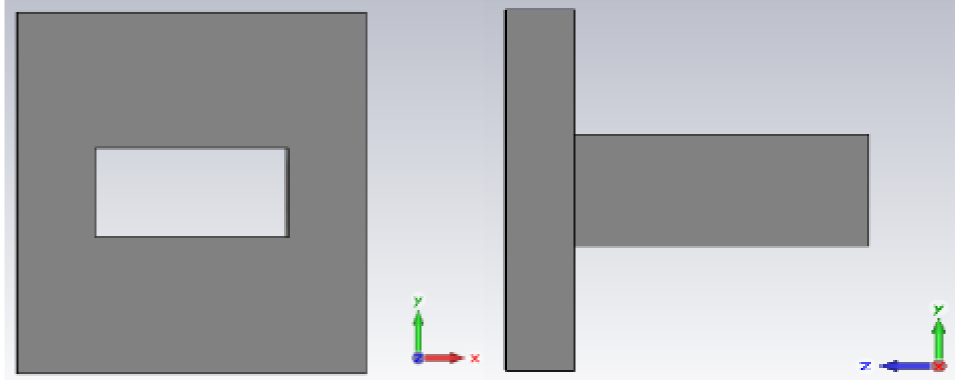

Figure 3.32 Open-ended waveguide CST model top and side view.

The gain of the open-ended waveguide from full wave simulation at 8.2 GHz is 4.821. Using the gain value, the antenna factor can be calculated as,

$$AF = \frac{9.73}{\lambda * \sqrt{G}}$$

where G is the gain of the waveguide.

Once the antenna factor is calculated, it can be applied to the recorded or measured fields to determine the field strength on the aperture of the antenna as,

$$Field\ strength = AF * probe\ output\ voltage$$

The obtained fields after applying the antenna factor are the radiated fields from the patches in response to per unit excitation (per Volt). Here the splitter loss is not taken into account as the calibration plane of the VNA is extended up to the input ports of the patches on port 1 and to the input port of the scanning antenna on port 2.

3.4.3. Measurement Results and Comparison with Simulated Data. The scanned fields from measurement over the PCB for both vertical and horizontal polarizations of the scanning antenna are shown in Figure 3.33 and Figure 3.34. Here the spatial scanning resolution is lambda/6 (6.1 mm) and resolution of reconstructed image is 2.05 cm. The height of the scan plane above the DUT surface is 2*lambda (73.2 mm).

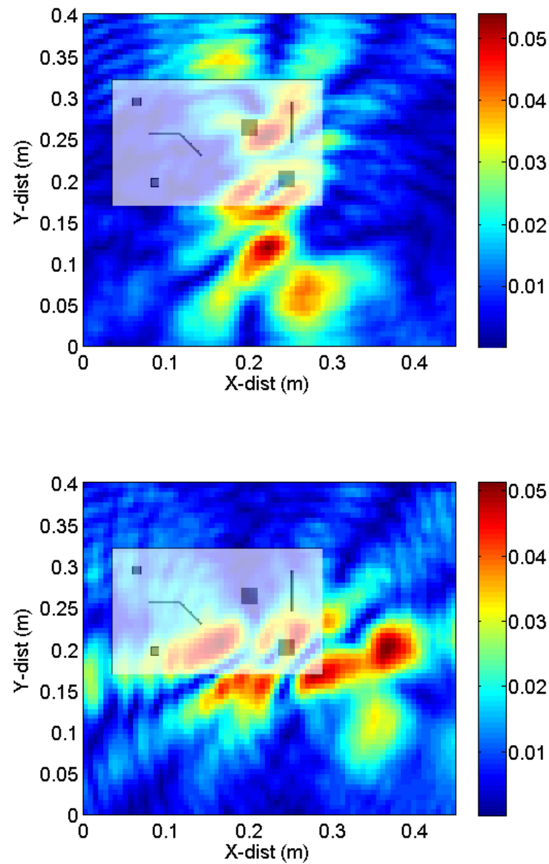

Figure 3.33 Measured |S21 | probe output on the scanning plane at 73.2 mm height for X and Y orientations of the antenna.

After applying the analytical gain of the antenna as the probe compensation factor, the fields values on the scanning plane can be derived. The measured magnitude for X and Y orientations of the antenna in V/m and measured phase in rad are shown in Figure 3.34 and Figure 3.35.

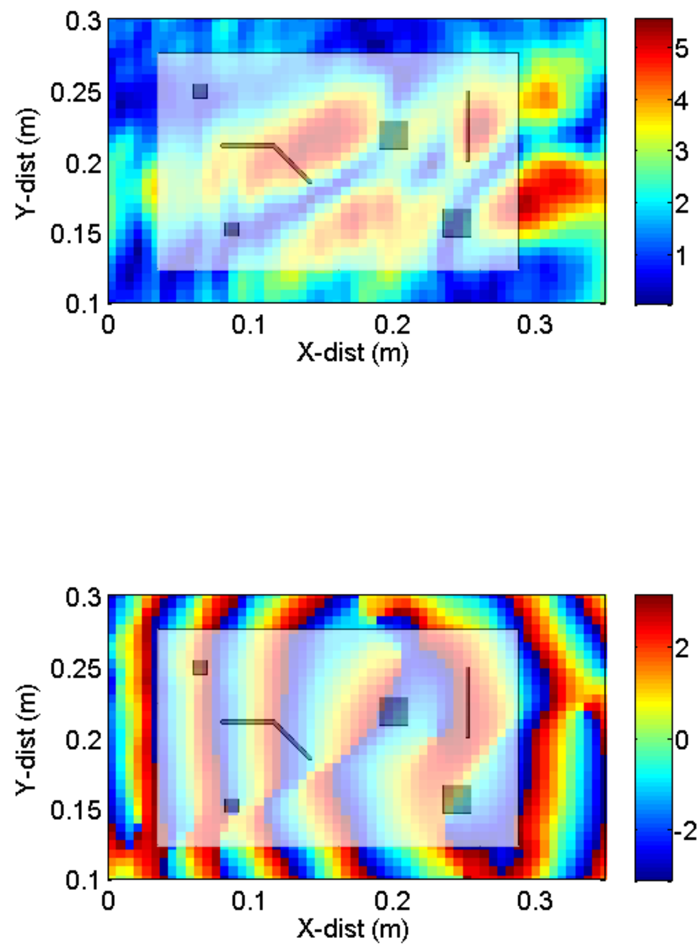

Figure 3.34 Measured E_x field magnitude (V/m) and phase (rad) at 73.2 mm height above the DUT.

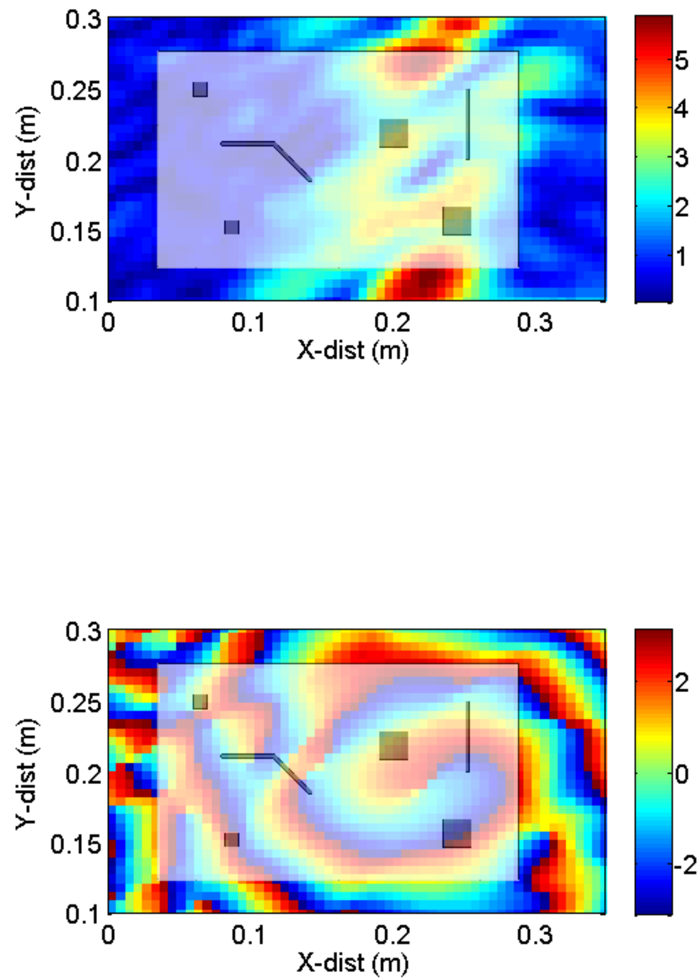

Figure 3.35 Measured E_y field magnitude (V/m) and phase (rad) at 73.2 mm height above the DUT.

This data can be compared by the full wave simulation results by normalizing the input excitation power with respect to measurement input. In simulation 0.5 W was used as input power which corresponds to 5 V, whereas in measurement an S21 measurement

was performed which can be considered as S21 per 1V input excitation. To normalize the measurement to 1V excitation, the input fields are divided by 5 V. The scanned fields from full wave simulation after normalizing to the measurement results are shown in Figure 3.36 and Figure 3.37.

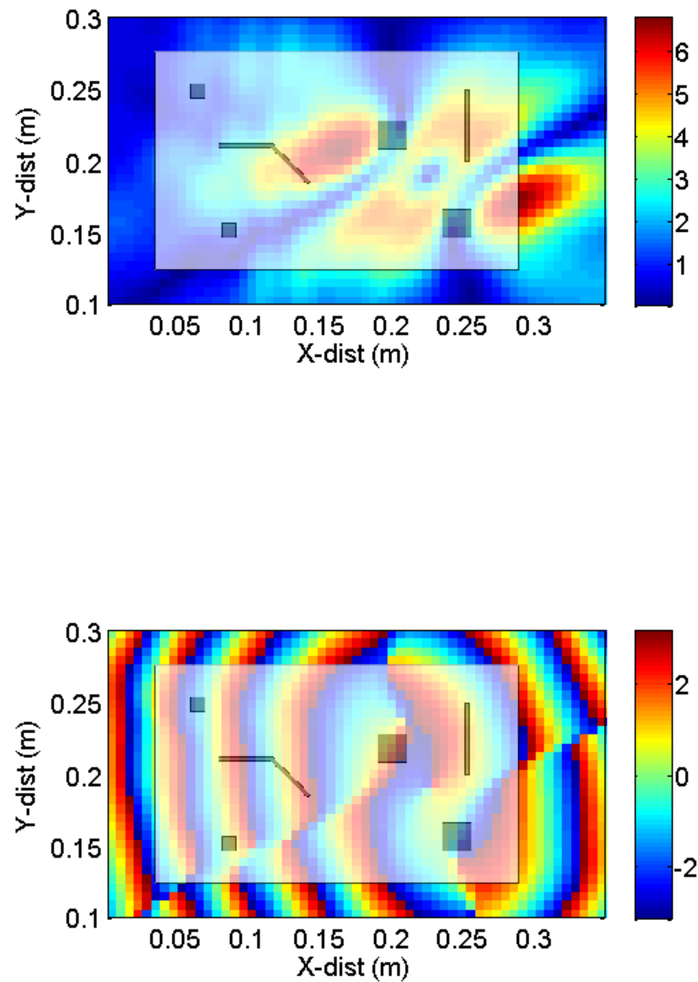

Figure 3.36 Simulated E_x field magnitude (V/m) and phase (rad) at 73.2 mm height above the DUT after normalizing.

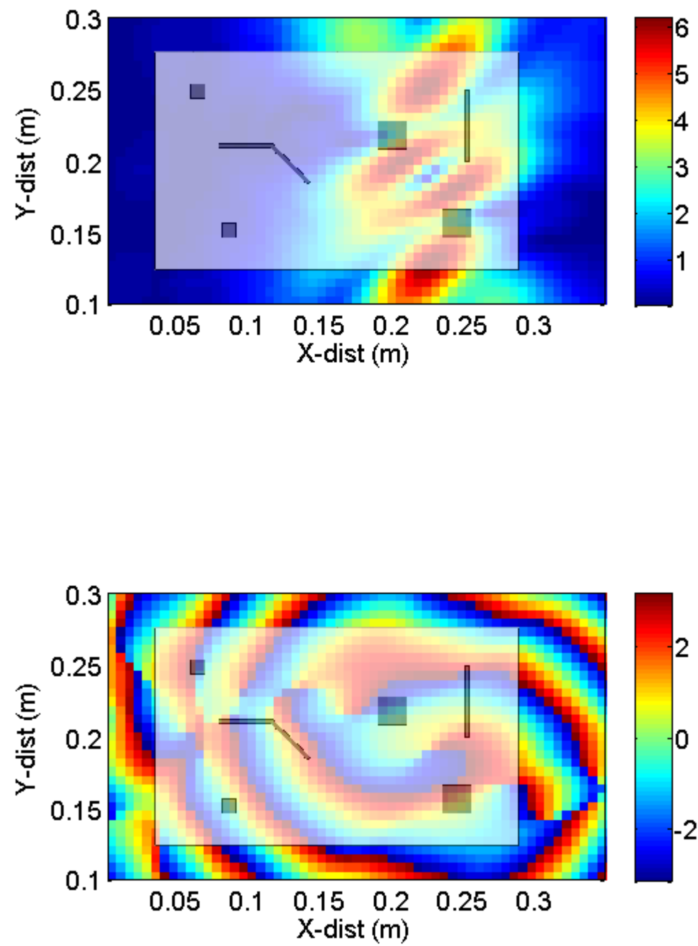

Figure 3.37 Simulated E_y field magnitude (V/m) and phase (rad) at 83.2 mm height above the DUT after normalizing.

Next the ESM algorithm is applied to the measurement as well as the simulated data to back-propagate the fields back to the source plane. The reconstructed fields on the source plane for E_x and E_y component using measured scanned are shown in Figure 3.38

and Figure 3.39. The reconstructed fields from the recorded scanned fields are shown in Figure 3.40 and Figure 3.41.

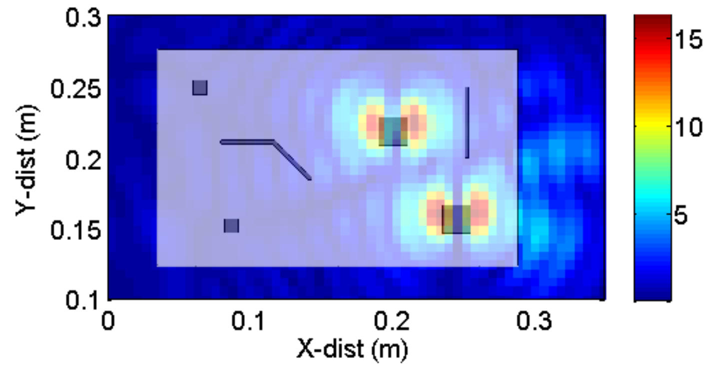

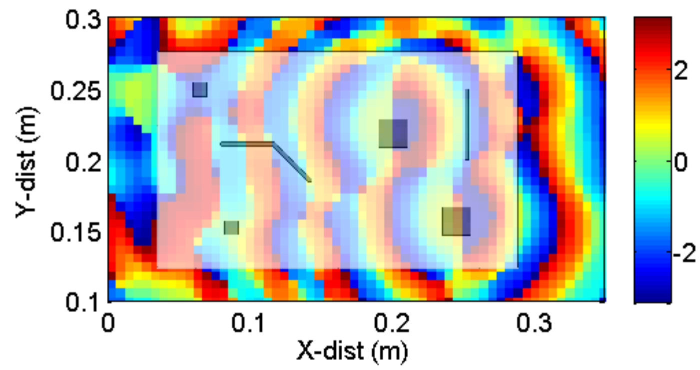

Figure 3.38 Reconstructed Ex field magnitude (V/m) and phase (rad) on PCB plane from measurement.

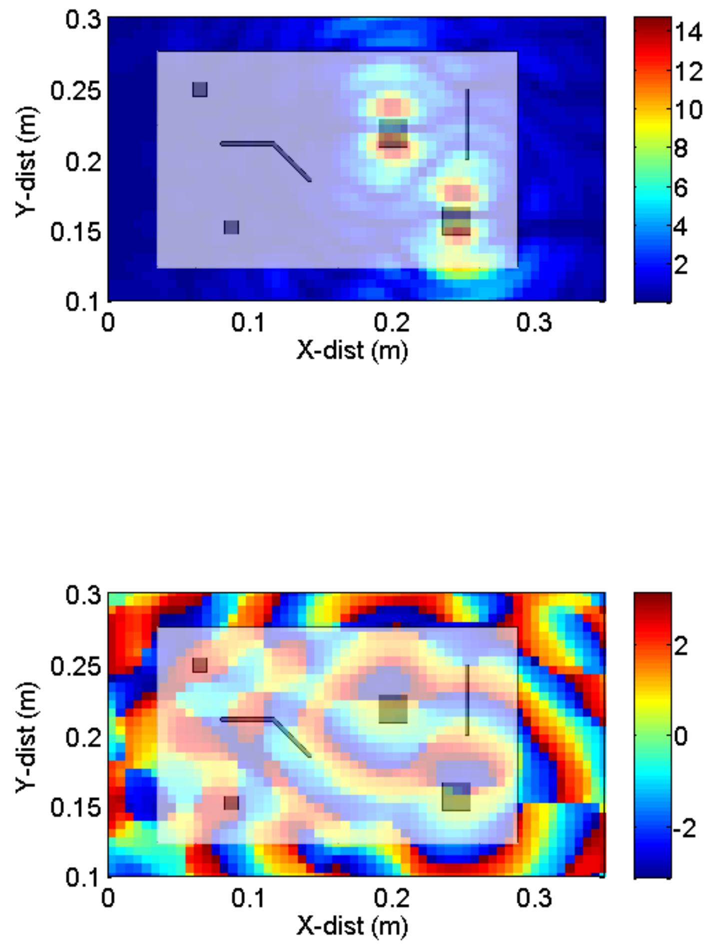

Figure 3.39 Reconstructed E_y field magnitude (V/m) and phase (rad) on PCB plane from measurement.

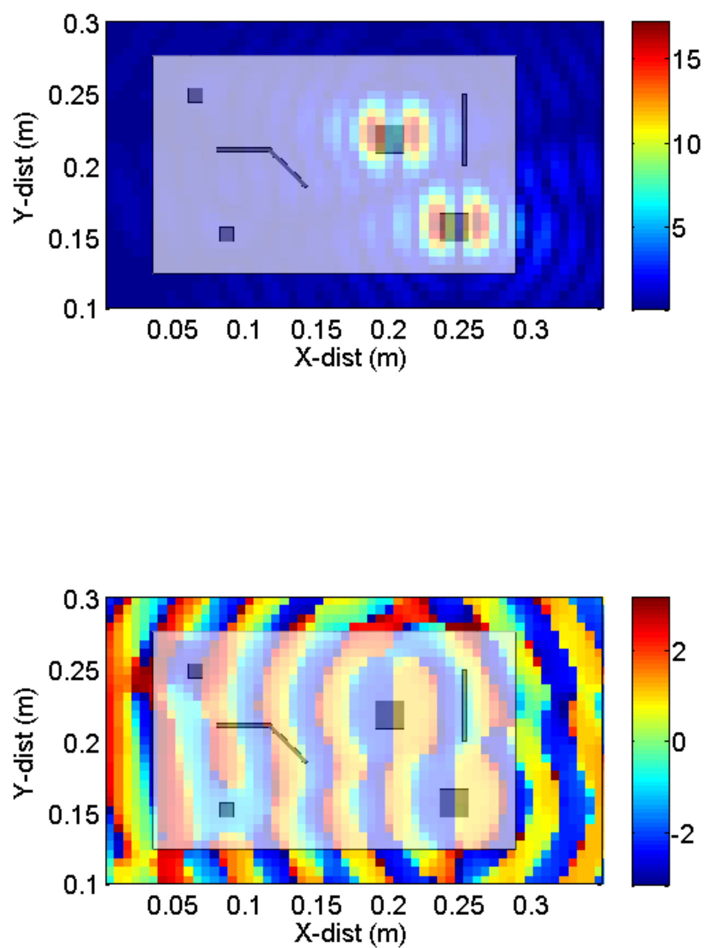

Figure 3.40 Reconstructed E_x field magnitude (V/m) and phase (rad) on PCB plane from full-wave simulation.

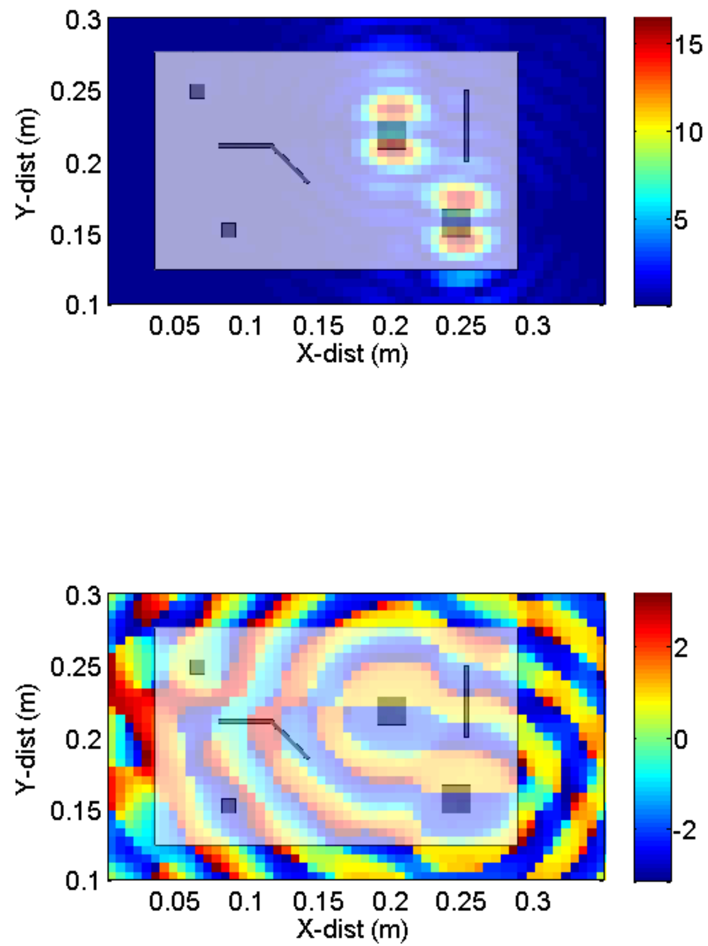

Figure 3.41 Reconstructed E_y field magnitude (V/m) and phase (rad) on PCB plane from full-wave simulation.

As seen the measurement and simulation results have a good agreement in the field values as well as in the localization of the sources. It can be concluded that using the

ESM methodology the radiating structures corresponding to the patches can be localized with high accuracy.

The difference in the measurement and simulation values maybe due to multiple reasons. Firstly the antenna gain value is derived from simulation. To get the actual gain value, antenna gain measurements needs to be performed. Also to improve the accuracy further, the complete probe correction needs to be applied by de-convolution of the response of the scanning antenna from the probe output voltage. Also to calculate the exact power delivered to the patches during excitation, the reflection loss needs to be compensated.

The next step is to perform near-field to far-field from the measured scanned fields and compare the far-field parameters with those computed from simulated scanned fields. The 3D far-field pattern computed for Etheta component in dBV/m using the measured focused fields on the PCB plane is shown in Figure 3.42, whereas Figure 3.43 shows the result from simulation.

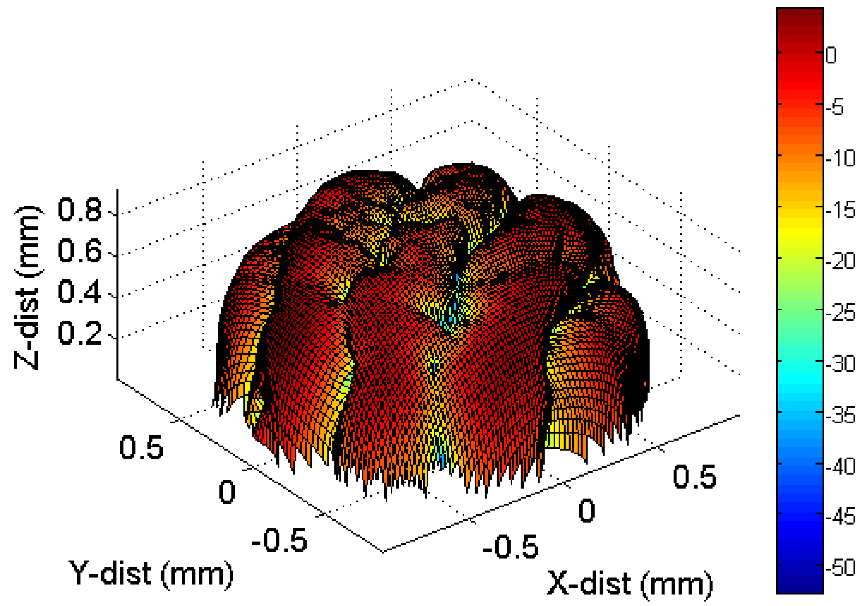

Figure 3.42 3D Far-field pattern using Etheta component (dBV/m) of the DUT calculated from NF-FF transform of the measured focused fields on PCB plane.

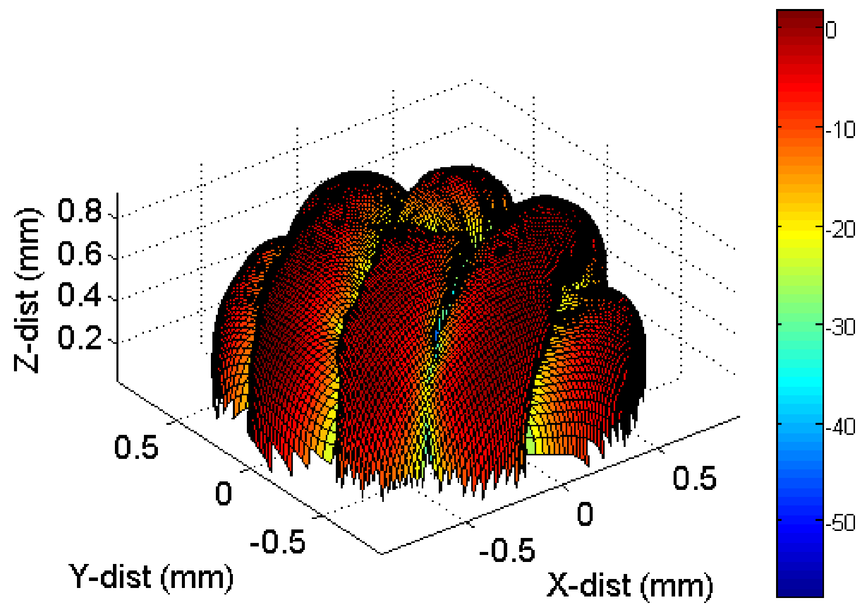

Figure 3.43 3D Far-field pattern using Etheta component (dBV/m) of the DUT calculated from NF-FF transform of the simulated focused fields on PCB plane.

The maximum value of the Etheta component from the measurement results is 2.73 dBV/m and from full wave simulation is 1.7 dBV/m. The total radiated power from simulation is 6.3 dBm whereas from measurement result is 7.0 dBm. So as seen, the results from the measurement agree with 2 dB with the simulated results. The comparison of 2D far-field patterns in dB scale from simulation and measurement are shown in Figure 3.44 through Figure 3.47.

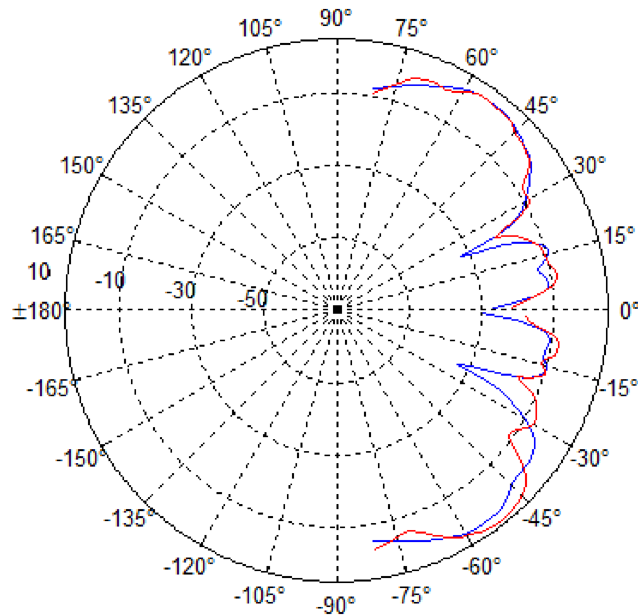

Figure 3.44 Constant Phi = 0 pattern using Etheta component (dBV/m).

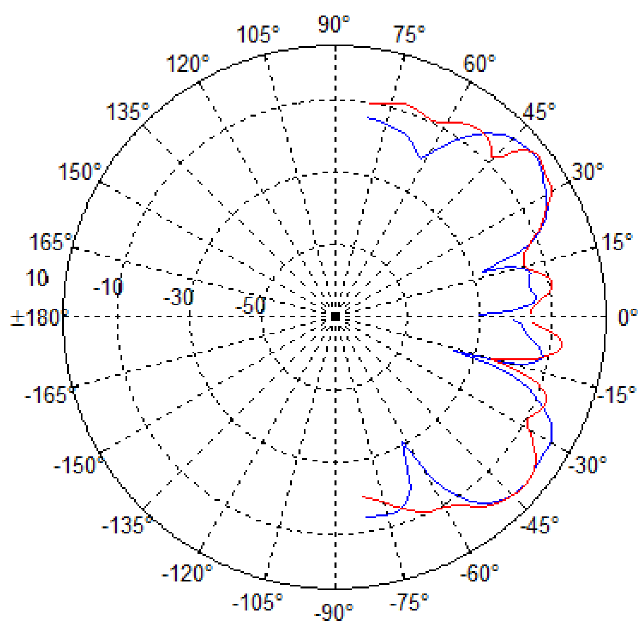

Figure 3.45 Constant Phi = 90 pattern using Etheta component (V/m).

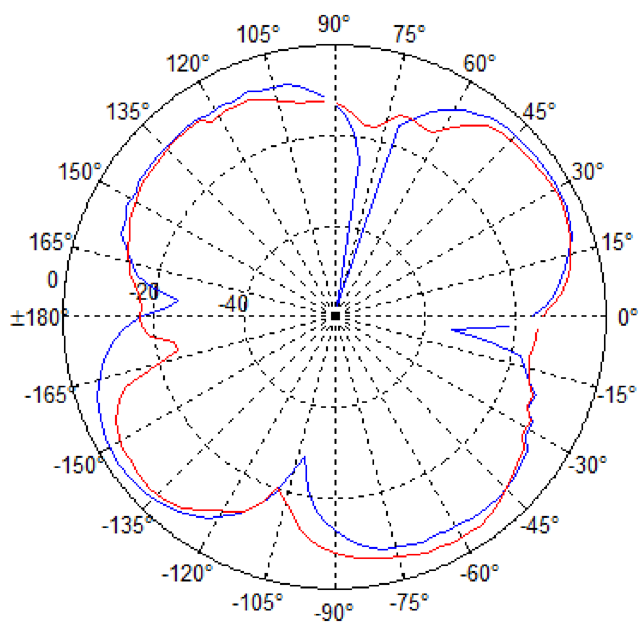

Figure 3.46 Constant Theta = 20 pattern using Etheta component (V/m).

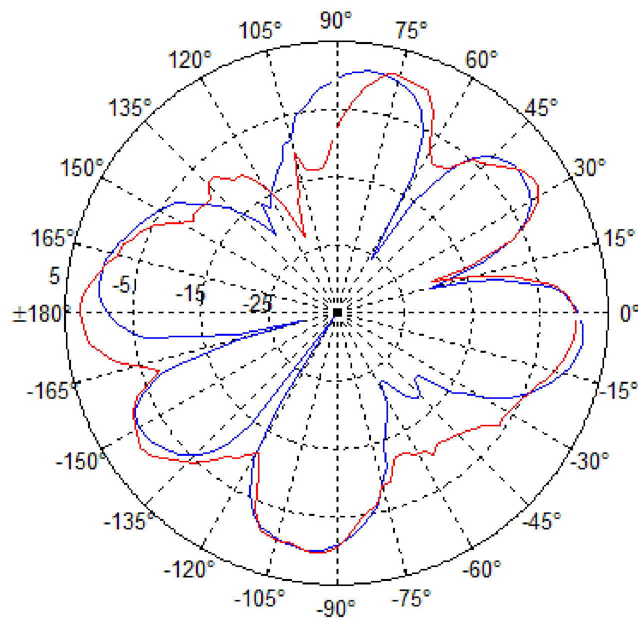

Figure 3.47 Constant Theta = 45 pattern using Etheta component (V/m).

As seen the 2D far-field patterns from simulation and measurement match closely.

3.4.4. Determining Far-Field Contribution from Individual Sources. Similar to the masking shown before for only simulation results, masking can also be applied to measurement data to determine contribution from individual sources. The reconstructed field using simulation data with the source corresponding to patch P1 is as shown in Figure 3.48 and Figure 3.49. The reconstructed field using measurement data with the source corresponding to patch P1 is as shown in Figure 3.50 and Figure 3.51.

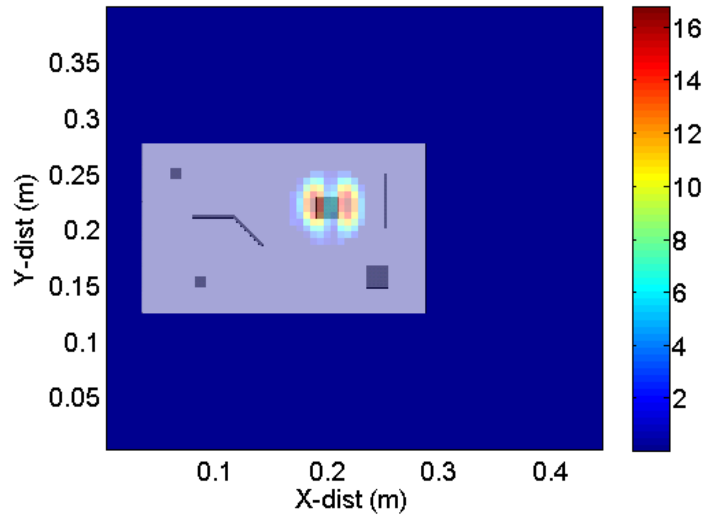

Figure 3.48 Reconstructed E_x field magnitude (V/m) with source corresponding to patch P1 kept active (simulation results).

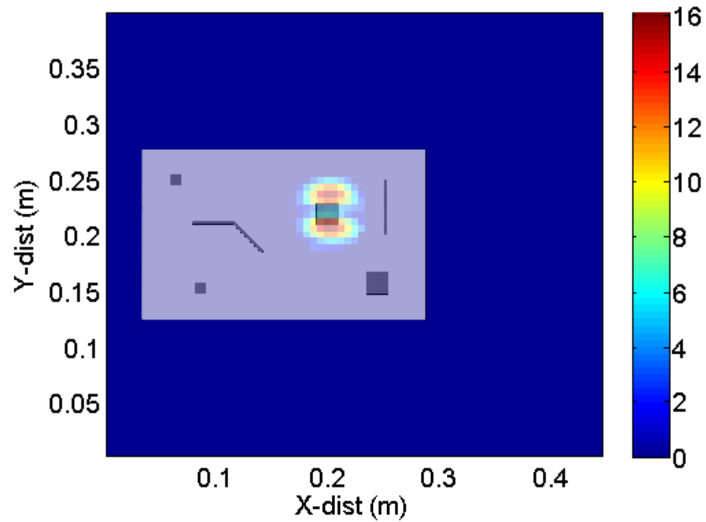

Figure 3.49 Reconstructed E_y field magnitude (V/m) with source corresponding to patch P1 kept active (simulation results).

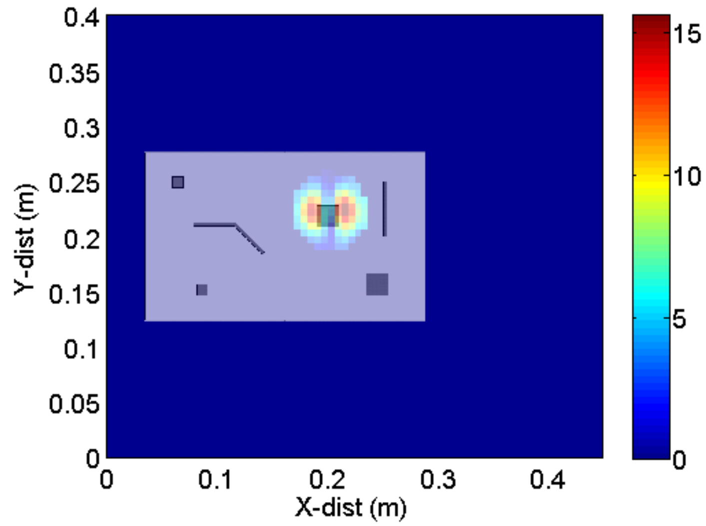

Figure 3.50 Reconstructed E_x field magnitude (V/m) with source corresponding to patch P1 kept active (measurement results).

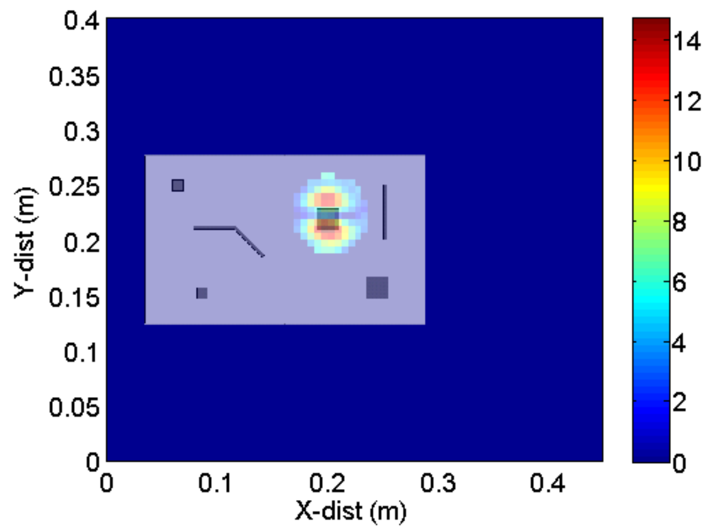

Figure 3.51 Reconstructed E_y field magnitude (V/m) with source corresponding to patch P1 kept active (measurement results).

Next NF-FF transformation is performed for the masked field images and far-field pattern is obtained. This data is compared with the full wave simulation with only patch P1 as active. The computed 3D far-field plots for Etheta component in dBV/m from measurement data are shown in Figure 3.52, whereas Figure 3.53 shows the far-field pattern obtained from simulation data. The maximum value of Etheta component using scanned masked fields is -5.2 dBV/m whereas using recorded masked fields is -6 dBV/m. The total radiated power computed using the recorded masked fields is 1.96 dBm whereas the one obtained from full-wave simulation is 1.19 dBm which is within 1 dB of the calculated results. This shows that the TRP can be predicted with good accuracy even after the sources are masked. So the contributions from individual sources can be calculated.

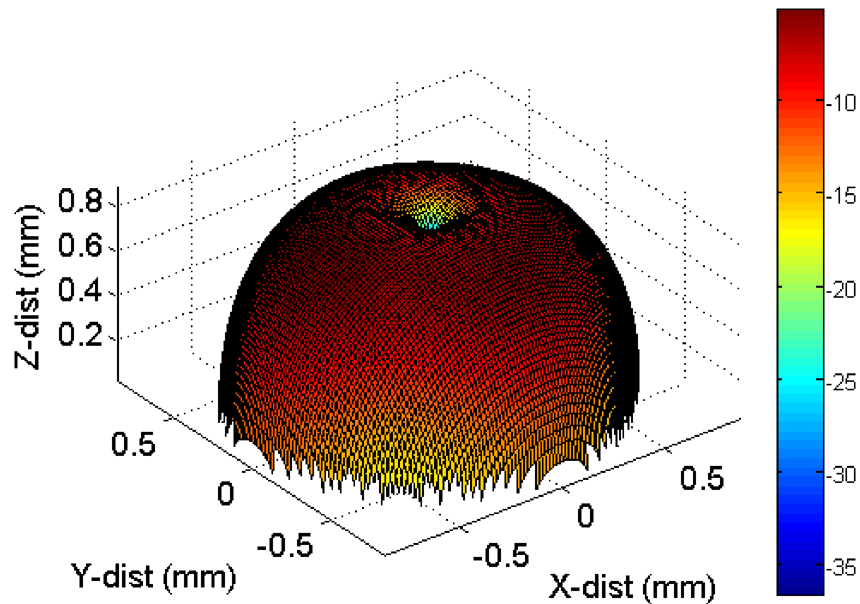

Figure 3.52 3D Far-field pattern for Etheta component (dBV/m) of the DUT obtained from masked fields (Using scanned fields).

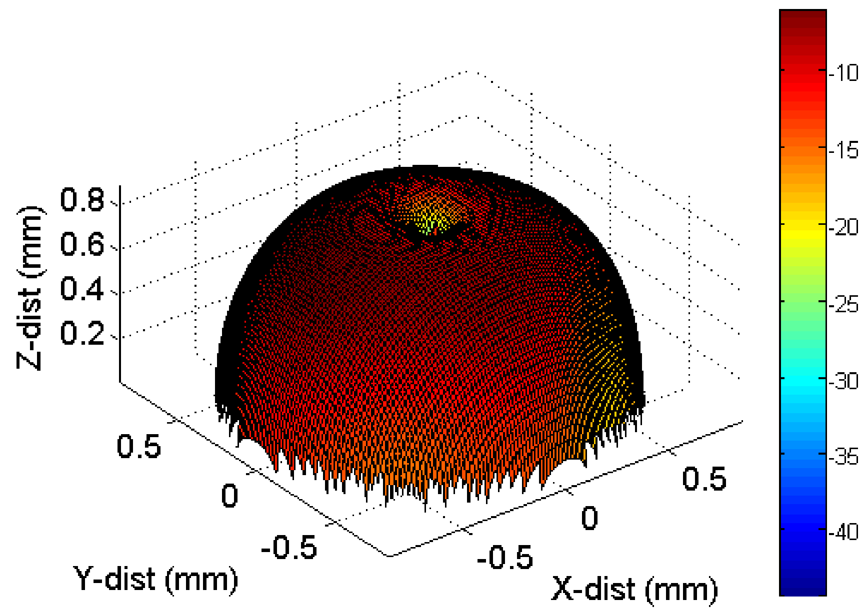

Figure 3.53 3D Far-field pattern for Etheta component (dBV/m) of the DUT obtained from masked fields (Using recorded fields).

Next 2D patterns of the far-field plot calculated from NF-FF of the masked recorded fields are compared with the results of masked scanned fields. The results for Etheta component 2D pattern for various constant theta and phi in V/m are plotted in Figure 3.54, Figure 3.55, Figure 3.56 and Figure 3.57.

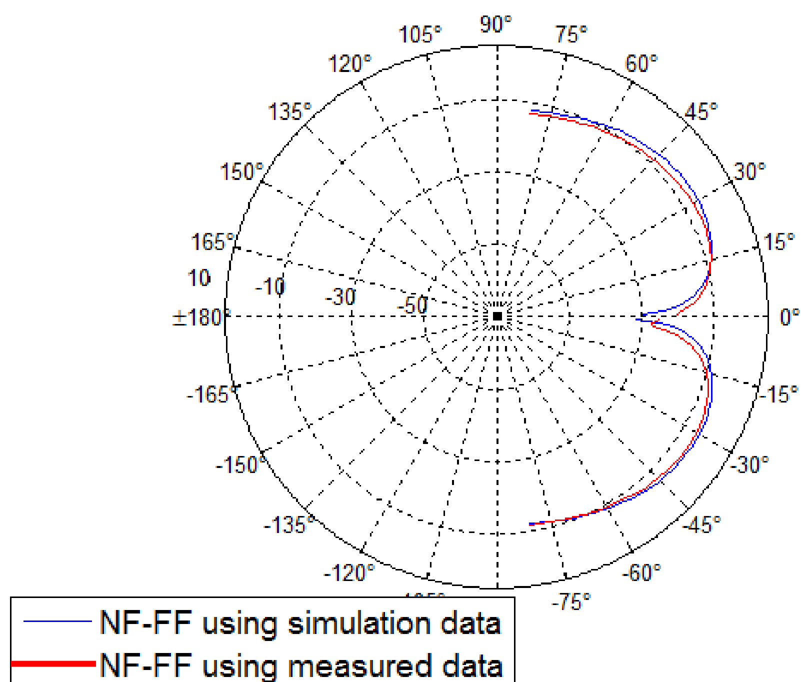

Figure 3.54 Constant Phi = 0 pattern using Etheta component (dBV/m).

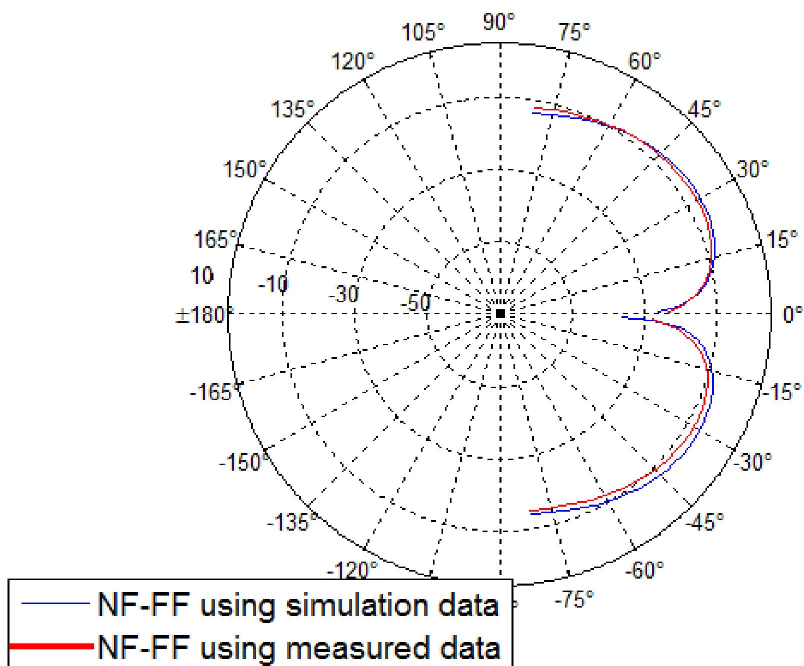

Figure 3.55 Constant Phi = 90 pattern using Etheta component (dBV/m).

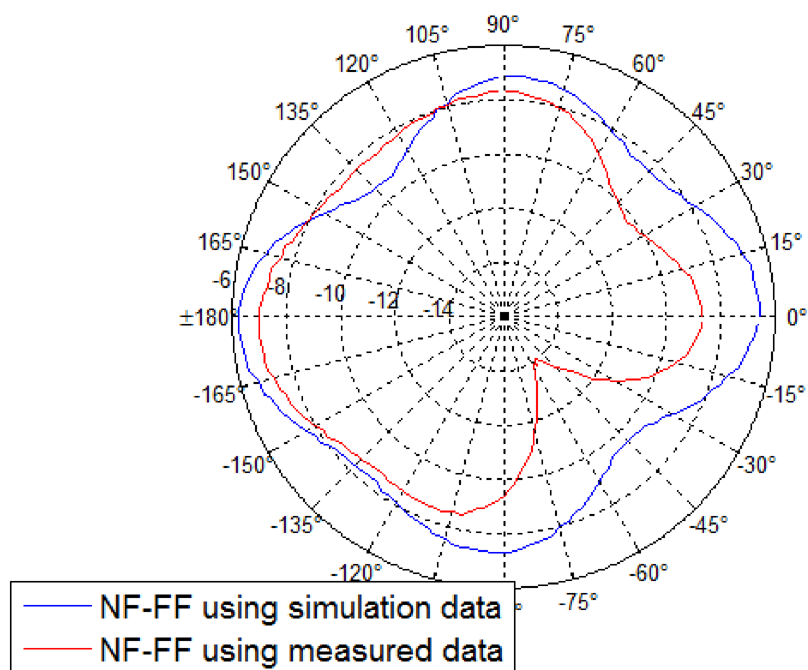

Figure 3.56 Constant Theta = 45 pattern using Etheta component (dBV/m).

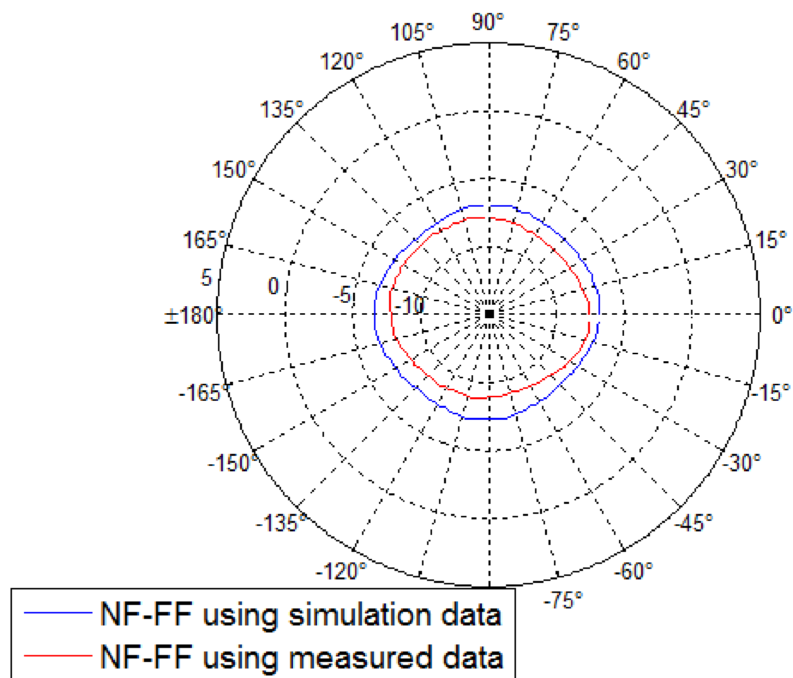

Figure 3.57 Constant Theta = 20 pattern using Etheta component (dBV/m).

3.5. EFFECT OF HEATSINK ON THE FAR-FIELD PARAMETRS

Another experiment was performed by placing a heatsink on top of one of the patches to observe the effect of change in radiation with the placement of heatsink. The heatsink is slightly larger than the patch size. The dimension of the heatsink are; each side = 25.64 mm and height = 37.85 mm. The heatsink is kept on top of patch P1 at a height of 1.32 mm with the help of a foam spacer. The fields were again measured at a height of 2*wavelength away (73.2 mm) above the PCB plane and ESM algorithm was applied as shown in Figure 3.58 through Figure 3.61.

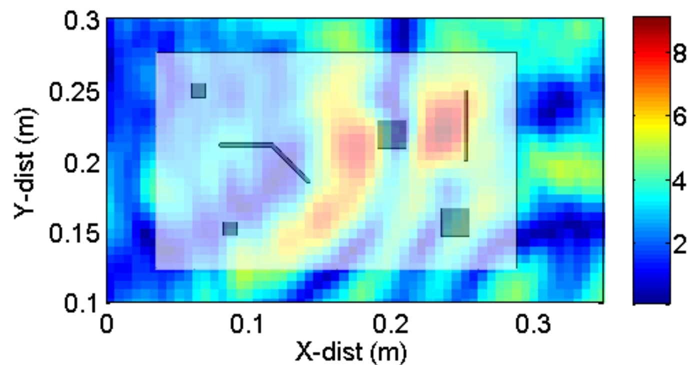

Figure 3.58 Measured E_x field magnitude (V/m) on a rectangular plane at 73.2 mm above the DUT with heatsink.

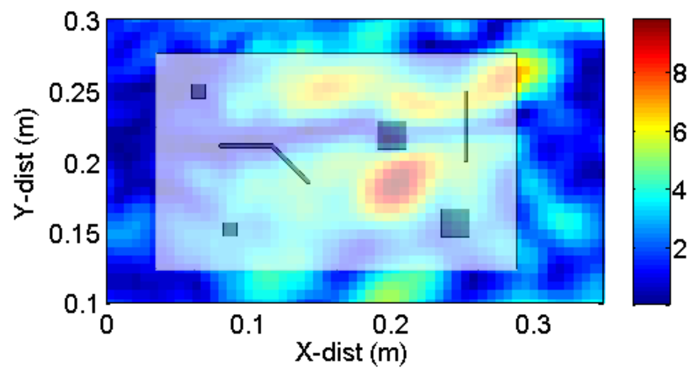

Figure 3.59 Measured E_y field magnitude (V/m) on a rectangular plane at 73.2 mm above the DUT with heatsink.

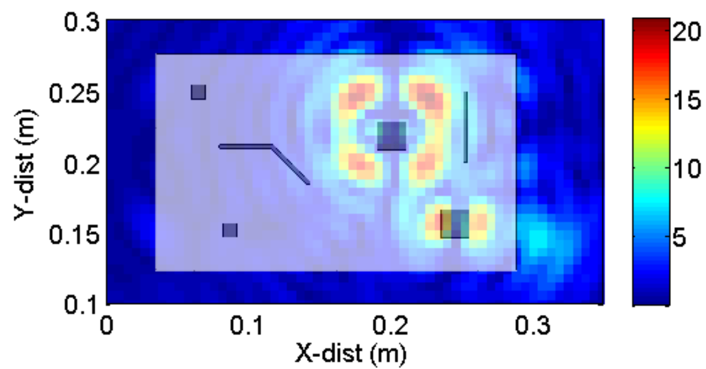

Figure 3.60 Reconstructed E_x field magnitude (V/m) on the PCB plane.

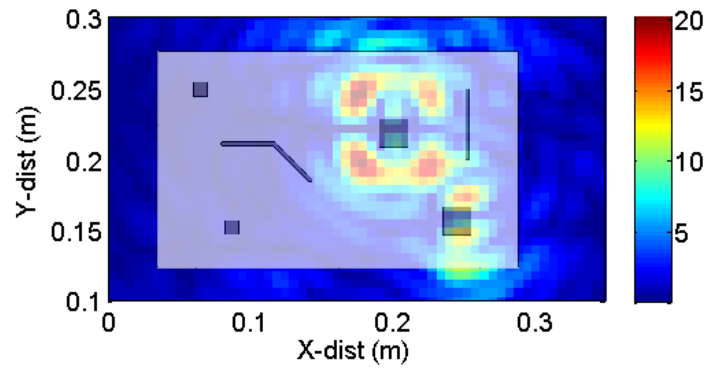

Figure 3.61 Reconstructed E_y field magnitude (V/m) on the PCB plane.

Using the reconstructed fields, the total radiated power of the DUT with heatsink can be calculated. The calculated TRP is 10.4 dBm which is an increase of over 3 dB from the case without the heatsink.

4. TEST OF METHODOLOGY ON ACTUAL DUT

The application of ESM methodology on a real DUT's is presented in this section. For a real DUT, both the scanned amplitude and phase must be measured. Different methods for phase measurement such as time-domain method [38] for spectrum analyzer based method are used in literature [37]. The drawback of the spectrum analyzer method for phase measurement is that it requires three scans to retrieve the complete amplitude and phase information. Additional investigation is required to improve the efficiency of the method.

For the time-domain phase domain method, the sampling frequency of the scope needs to be higher at least twice the frequency of the measured signal. If this is not possible a frequency down-conversion unit is required to get the measured signal frequency within the bandwidth of the measuring instrument. Also to obtain an optimal frequency resolution, a long time-record is required to be captured which leads to overhead in storage. To overcome the drawbacks of the above methods, a frequency domain phase measurement method is presented in this paper by using the tuned receiver mode in a vector network analyzer.

For phase measurement using VNA in the tuned receiver mode, the internal RF source is turned off, so the individual amplitudes and phase difference of the signals on the two ports can measured. For a real hardware board, a reference signal to one port of the VNA can be obtained either by tapping the signal from the board or using a stationary reference antenna. The other port of the VNA can be used as an input from the scanning antenna. The phase difference between the reference and the measurement channel

provides the phase value for the scanned fields. The amplitude from the scanning antenna can be measured directly.

4.1. REAL DUT 1 – NETWORK SWITCH

For testing the ESM methodology, measurements were performed on a real DUT. The first DUT used for analysis is an off-the-shelf networking device with default software configuration installed. Figure 4.1 shows the measured radiation spectrum from a real DUT used for this measurement. This measurement is performed by operating the DUT in a reverberation chamber and measuring the total radiated power using a spectrum analyzer. It can be seen that there are 15 peaks in the spectrum centered at 10.3125 GHz. Here the focus is only on identifying the source corresponding to a single frequency component. Once the source is identified, EMI mitigation measures using an absorber material are also presented. Similarly, the analysis is extended to other frequency components too.

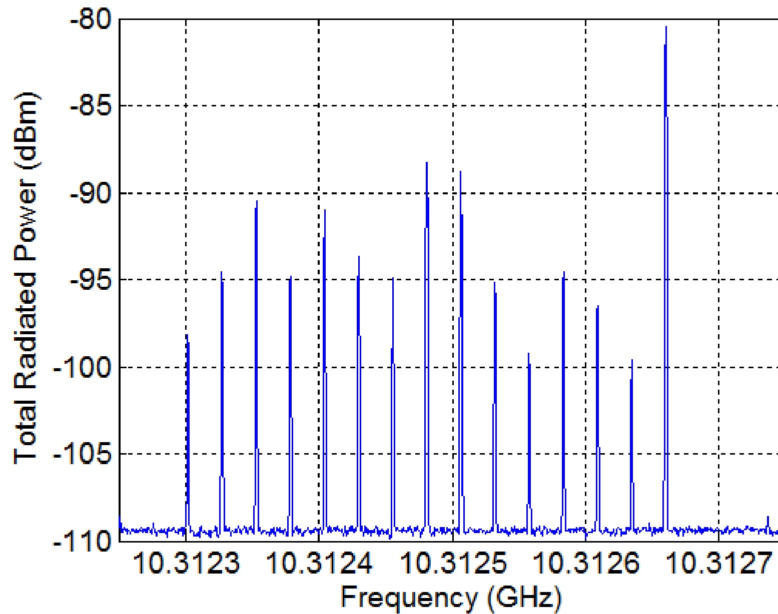

Figure 4.1 Radiation spectrum from the DUT.

The test setup for the hardware measurement using ESM technique is shown in Figure 4.2 and Figure 4.3. The DUT with dimensions of 45 cm × 40 cm × 4 cm is placed at the center of the API 3-axis scanning system [29]. The frequency to be used for demonstrating the ESM methodology is the one corresponding to peak # 12. At this frequency the required maximal spatial scanning step is 1.5 cm to satisfy the Nyquist criterion. In the actual measurement, a scanning resolution of 7 mm is used. The height of the scanning plane above the PCB is about 8.3 cm, which is between two to three wavelengths at the test frequency.

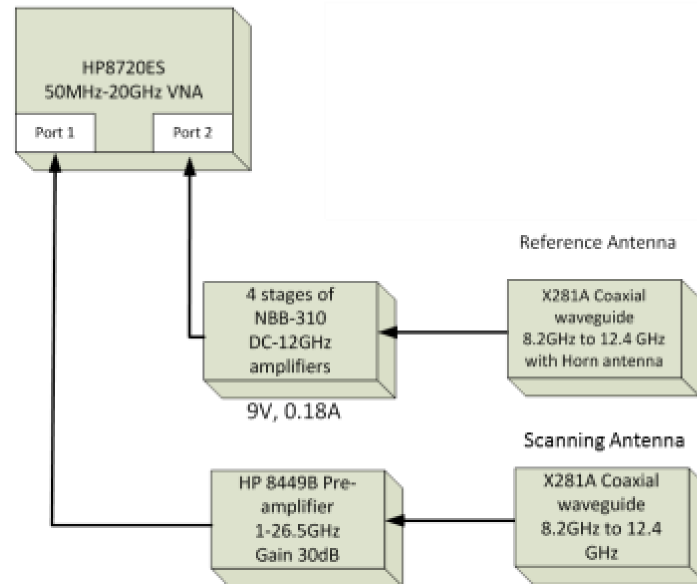

Figure 4.2 Measurement setup for phase and amplitude measurement.

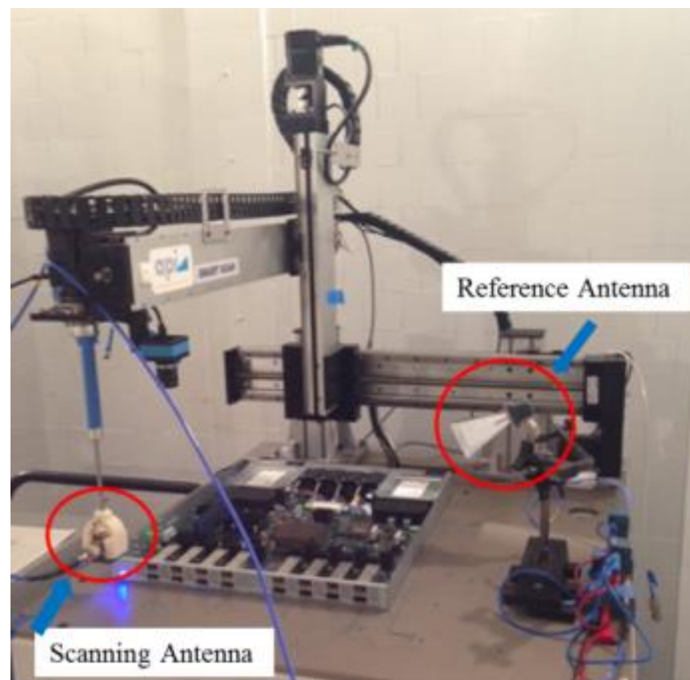

Figure 4.3 Actual Measurement setup.

For this measurement, the 8.2-12.4 GHz standard gain horn antenna was used as a reference antenna. This reference antenna is fixed at a distance away from the DUT in the direction to maximize the output at frequency #12. It is connected to port 2 of VNA through three cascaded DC-12 GHz amplifiers each providing 10 dB gain. The scanning antenna is an 8.2-12.4 GHz open-ended waveguide connected to the arm of the 3-axis robotic scanning system. The output of the waveguide is amplified by a low noise broadband amplifier with a gain of 30 dB before connecting to Port 1 of the VNA. The scanning antenna moves over a scanning plane in a rectangular grid and measures one tangential component of the field in one scan. To measure the orthogonal field component, the antenna is rotated 90 degrees and the scan is repeated.

For phase measurement, the VNA is used in a tuned receiver mode. The VNA is centered on the desired frequency and operated in zero span mode. The number of sweep points is set to 101 to obtain an average of the measured signal, which allows improving the signal-to-noise ratio. The IF bandwidth is kept at 300 Hz as a trade-off between the sweep time, signal to noise ratio and the need to accommodate the drift in the center frequency. It was observed that the drift in center frequency was much higher than 300 Hz. The IF bandwidth could not be increased due to the limited signal to noise ratio of the desired signal. So it was decided to introduce a calibration routine accounting for the drift in the frequency. The calibration routine changes the VNA span to 500 KHz from 0 Hz and searches for the exact peak corresponding to desired frequency. It then again designates it as the center frequency and continues measurement of phase and amplitude. This frequency tracking is performed after every 100 points are scanned.

The image of the DUT is overlapped and aligned with the image of the scanned fields to observe the underlying physical sources of radiation as shown in Figure 4.4 and Figure 4.5. In this figure, the DUT image has been replaced by the blocks due to the proprietary information. Four big black blocks represents the heatsinks in the DUT, 16 smaller blue blocks with the same size represents the physical layer transceiver (PHY), and 8 red rectangular blocks corresponds to the optical transceivers on the DUT. As observed, no detailed information about the source of radiation can be obtained from the scanned fields. The quantity plotted is the magnitude and phase of the signal at the VNA Port 1, and the units are dBV and radians respectively.

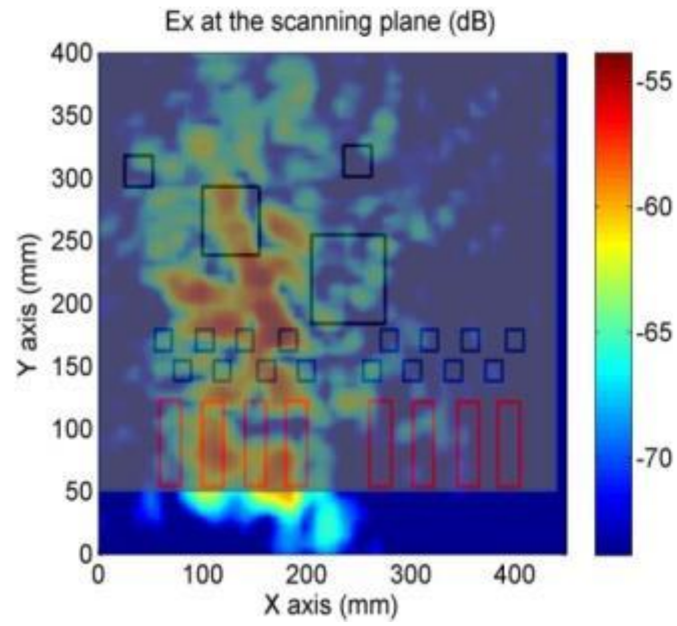

(a)

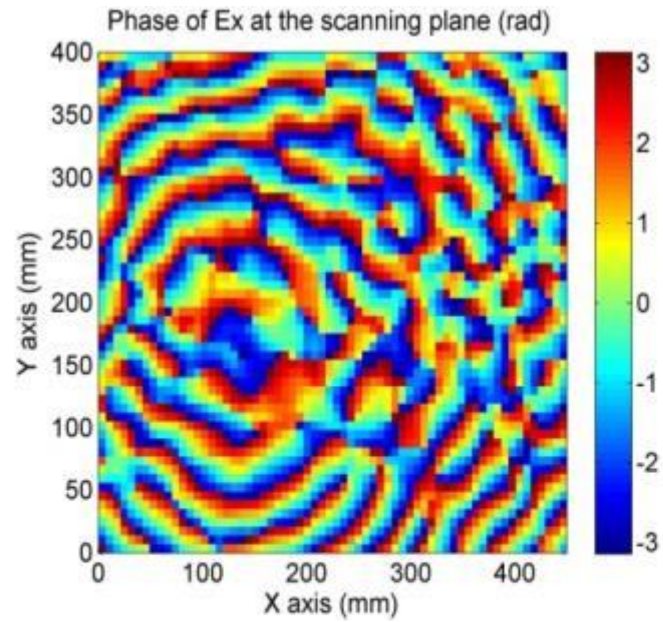

(b)

Figure 4.4 (a) Measured E_x field magnitude in dBV (b) Measured E_x field phase in rad.

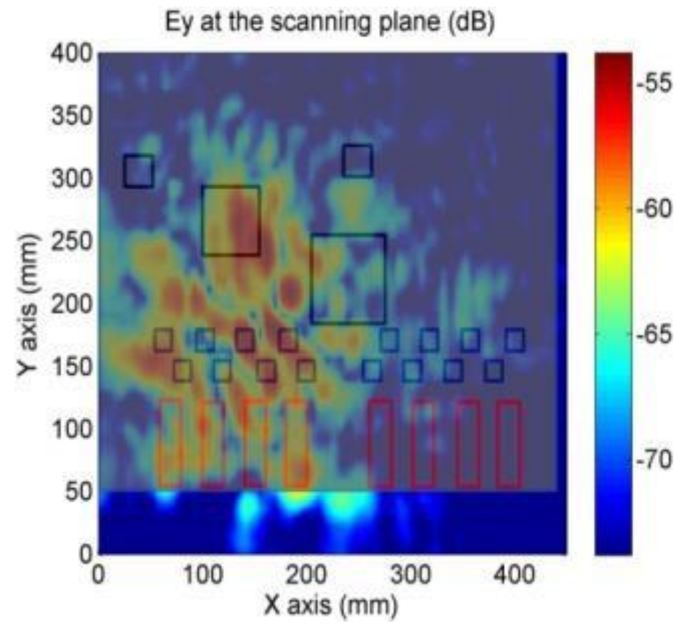

(a)

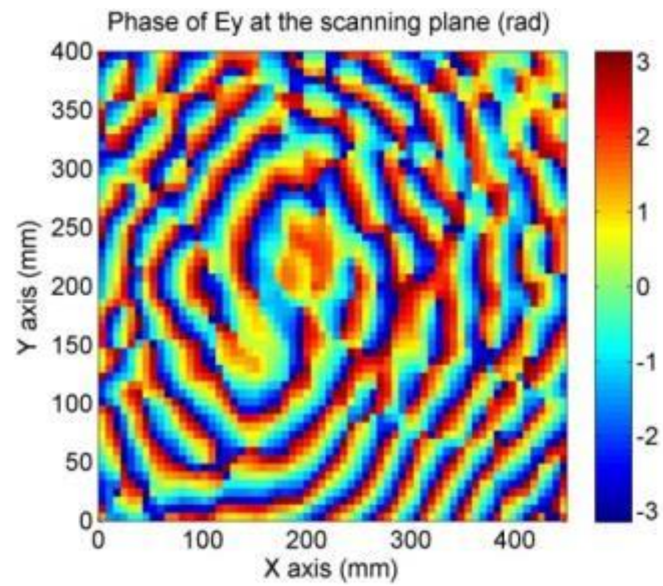

(b)

Figure 4.5 (a) Measured E_y field magnitude in dBV (b) Measured E_y field phase in rad.

After applying the ESM methodology, hot spots corresponding to the radiation sources are observed. The resolution of the ESM methodology is limited by the aperture angle and the noise in the system. To improve the resolution of the ESM methodology, a near-field scan can be performed in the limited area where the hot spots are observed. The spatial step for near-field scanning has to be 1 mm to be able to observe the field variation with a high resolution. Also the near-field scanning is performed 2 mm above the profile of the DUT. This would require the probe to retract back and forth while scanning. The scanning step and the retract action leads to a very large scanning time even for a small geometry. So it is advantageous to use the information provided by the ESM methodology to determine an area for near-field scanning. The near-field scanning results for the frequency # 12 using an EMI near-field magnetic field probe is as shown in Figure 4.6. For near-field scanning also, the frequency tracking algorithm is applied. It provides the surface current distribution corresponding to frequency # 12. It contains both the evanescent and propagating wave components. No particularly useful information about the radiating structure can be obtained from the field data. This is not enough to decide where exactly to put the absorbers to reduce the far-field radiation.

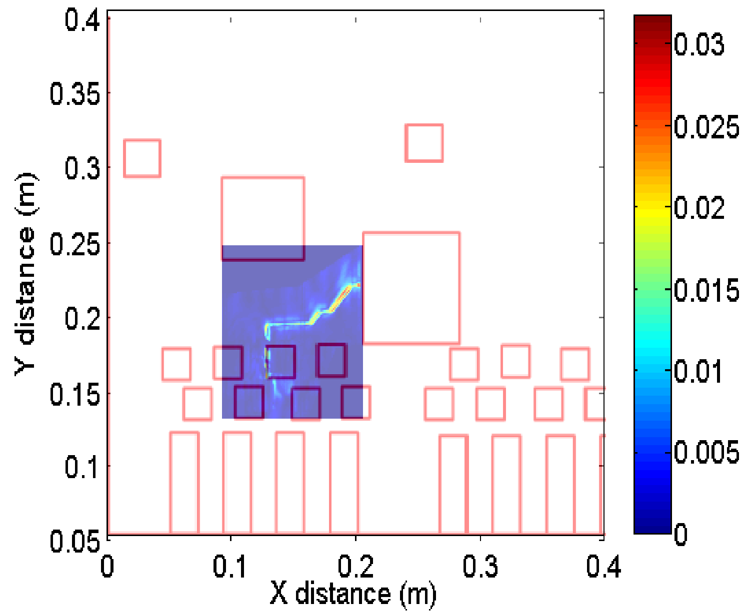

Figure 4.6 Measured total tangential field component magnitude in dBm.

To identify the source location, ESM algorithm as given by (1) is applied on the scanned fields shown in Figure 4.4 and Figure 4.5. The reconstructed fields on the source plane for both orientations of the antenna are shown in Figure 4.7 and Figure 4.8.

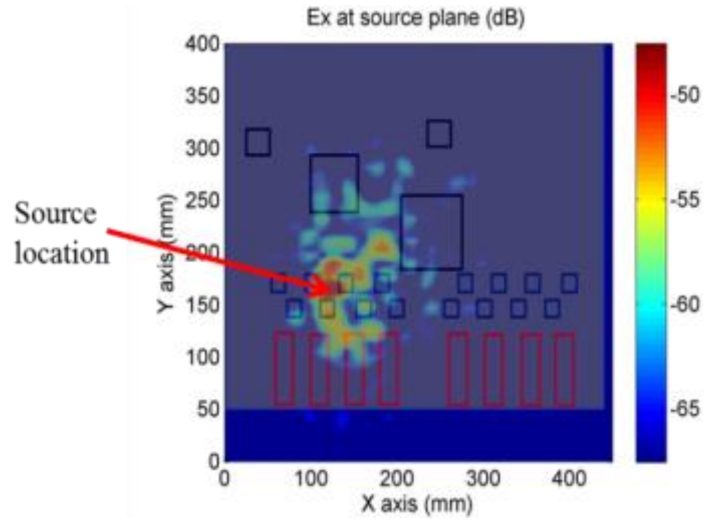

Figure 4.7 Reconstructed E_x field component magnitude in dBm at the PCB plane.

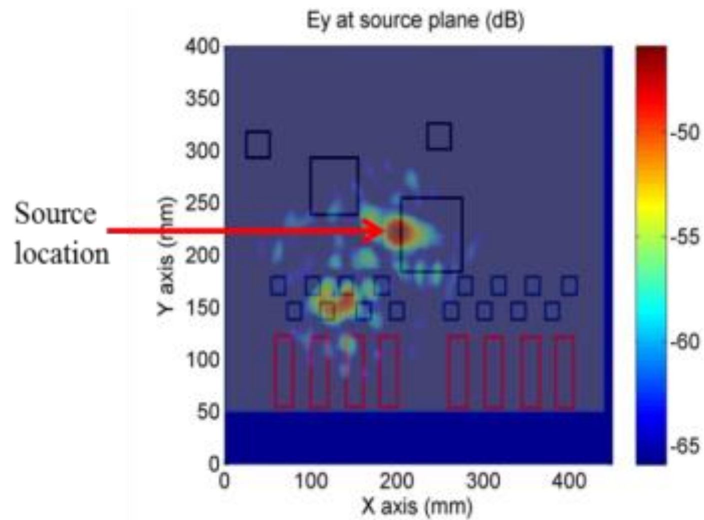

Figure 4.8 Reconstructed E_y field component magnitude in dBm at the PCB plane.

The resolution of the reconstructed image can be estimated as 1.5 cm according to equation (6). Here it can be seen that for the radiation in x direction, the source is mainly

located near one of the PHYs of the board; and for the radiation in y direction, the source is mainly located at the edge of the main heatsink.

Based on the information obtained from the ESM transformation, we can identify a suitable position for placing the absorber material to mitigate the radiation at frequency #12. The properties of the absorber material are defined by the permittivity and permeability. Any use of absorber involves a trade-off between material absorptivity and impedance matching at the surface [39]. Finding a suitable absorber material for the desired frequency range will improve the effectiveness of the absorber and thus reduce the total volume of the material required. In this work, for frequencies at 10 GHz, a non-conductive, magnetically lossy material (BSR-2) [40] was used for EMI mitigation. Four pieces of absorber material are placed on the edge of the main heatsink where the hot spot corresponding to the source of radiation can be observed as marked in Figure 4.8. Each piece of absorber material size is 2 cm by 2.8 cm, with the thickness 1 mm. The placement of the absorber material is as shown in Figure 4.9.

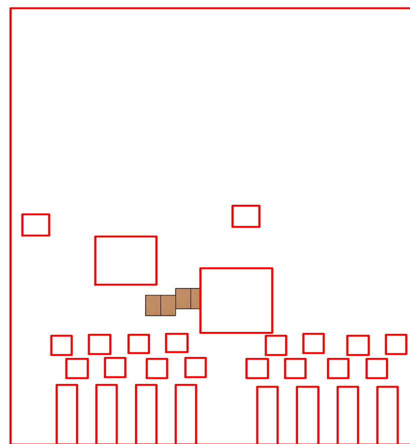

Figure 4.9 Applied absorbers (2 cm by 2.8 cm).

Figure 4.10 and Figure 4.11 shows the reconstructed image from the source plane, after the absorber materials are added at the source location. The color scale corresponding to the field strength in Figure 4.10 and Figure 4.11 is set to be the same as Figure 4.7 and Figure 4.8 and to facilitate comparison. It can be clearly observed that the field strength at the source location has been greatly reduced due to the effect of the absorber material. This validates the location of the source identified by the ESM algorithm to be accurate.

By comparing the reconstructed field strengths in the source plane with and without the absorber material, the maximum value of the source in the *x* orientation is reduced from -47.6 dB to -53.9 dB, when the absorber material is added; for the *y* orientation, the maximum value of the source is also reduced from -45.9 dB to -49.9 dB.

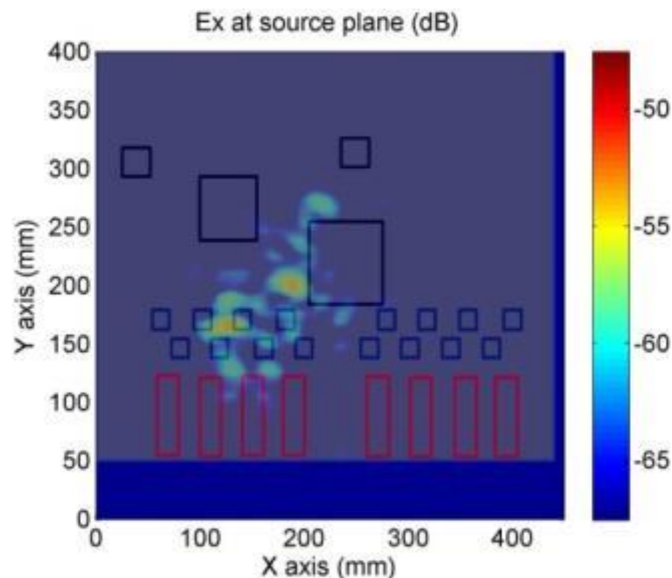

Figure 4.10 Reconstructed E_x fields at the PCB plane with absorber.

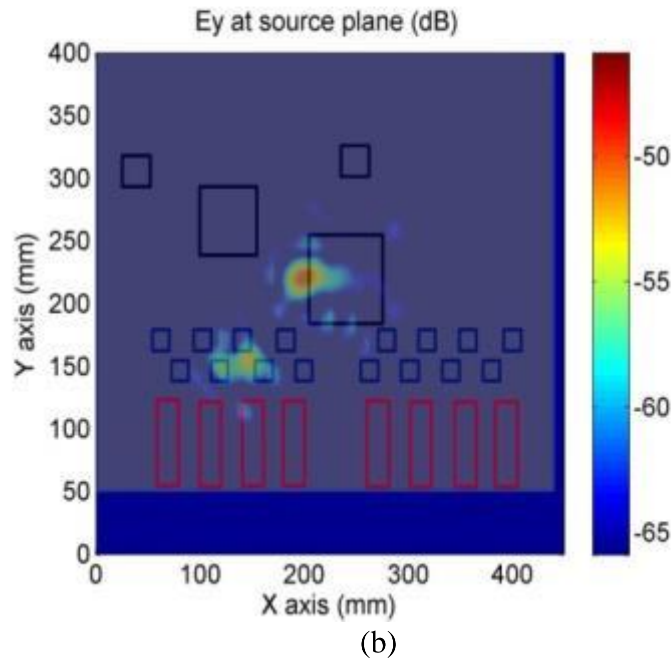

(b)

Figure 4.11 Reconstructed E_y fields at the PCB plane, with absorber.

As seen from the previous results, it can be observed that the source radiation is reduced by approximately 4 dB when the absorber material is placed at the location identified by the ESM algorithm. To validate these results in the far-field, a total radiated power measurement (TRP) is performed on the DUT using a reverberation chamber [41]. The reverberation chamber measurement is widely used for EMI testing and particularly effective in quantifying the total radiated power of the DUT. Figure 4.12 shows the setup for the TRP measurement of the DUT. A spectrum analyzer is used with center frequency at 10.3125 GHz and the span as 500 kHz. A low noise 30 dB broadband amplifier is used to increase the received signal strength. Figure 4.13 shows the averaged total radiated power spectrum comparison with and without absorber material.

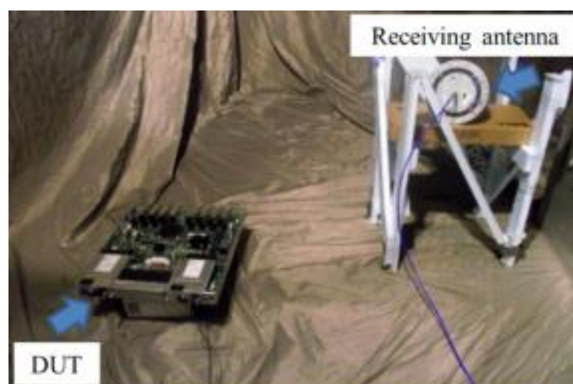

Figure 4.12 Setup for TRP measurement in a reverberation chamber.

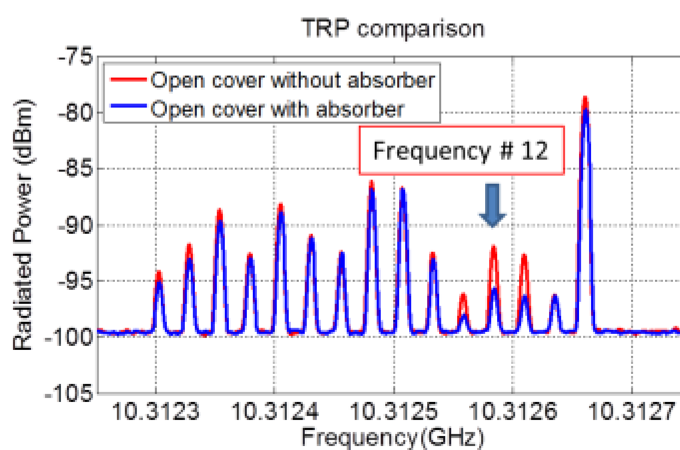

Figure 4.13 TRP spectrums comparison with and without the absorber material.

From the Figure 4.13, it can be seen that the peak value corresponding to frequency #12 has reduced about 4 dB, due to the absorber material, which validates the previous measurement using the ESM method. But as observed, most of the other frequencies are not affected by the placement of the absorber material. This reconfirms that the location of absorber material determined by the ESM algorithm mainly corresponds to the source of frequency # 12.

The next step is to determine the optimal size and placement of absorbing material to reduce the heatsink radiation. Using a picture frame structure below the heatsink it can be observed that the total radiation by the heatsink can be reduced. The picture frame structure below the heatsink is shown below in Figure 4.14.

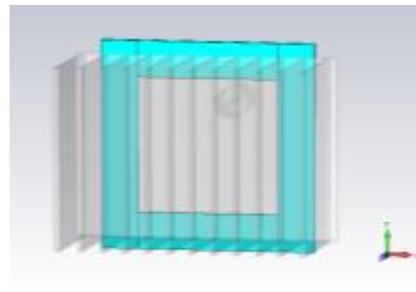

(a)

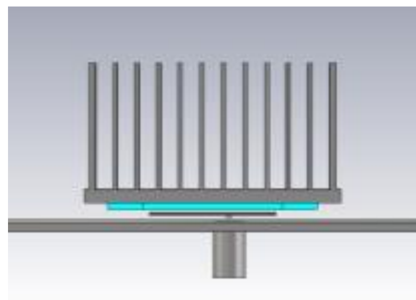

(b)

Figure 4.14 Absorber material below the heatsink (a) Top view (b) side view.

Simulation and measurement were performed for the cases with and without the picture frame absorber below the heatsink to compare the total radiated power. The total radiated power measurement was performed in a reverberation chamber as shown in

Figure 4.15 and Figure 4.16. The measurement results are shown in Figure 4.17. The chamber quality factor Q is a constant [41] at a given frequency, is given as,

$$Q = \frac{16\pi^2 V}{\lambda^3}\frac{\langle P_T \rangle}{\langle P_R \rangle} \rightarrow \frac{\langle P_T \rangle}{\langle P_R \rangle} = \frac{16\pi^2 V}{Q\lambda^3} = constant$$

where V is the volume of the chamber, P_T is the power transmitted by the DUT, P_R is the power received by the receiving antenna.

Using the above relation, the total radiated power of the DUT can be given as,

$$\langle P_{T(DUT)} \rangle = \frac{16\pi^2 V}{\lambda^3}\langle P_{R(DUT)} \rangle = \frac{\langle P_T^{CAL} \rangle}{\langle P_R^{CAL} \rangle}\langle P_R^{DUT} \rangle$$

where P_T^{CAL} is the transmitted power during calibration by the standard antenna, P_R^{CAL} is the power received by the receiving antenna during calibration.

In our case, the total radiated power of the heatsink can be obtained as,

$$\langle P_T^H \rangle = \frac{(1 - |S_{11}^A|^2)}{|S_{21}^A|^2}|S_{21}^H|^2 \approx \frac{|S_{21}^H|^2}{|S_{21}^A|^2}$$

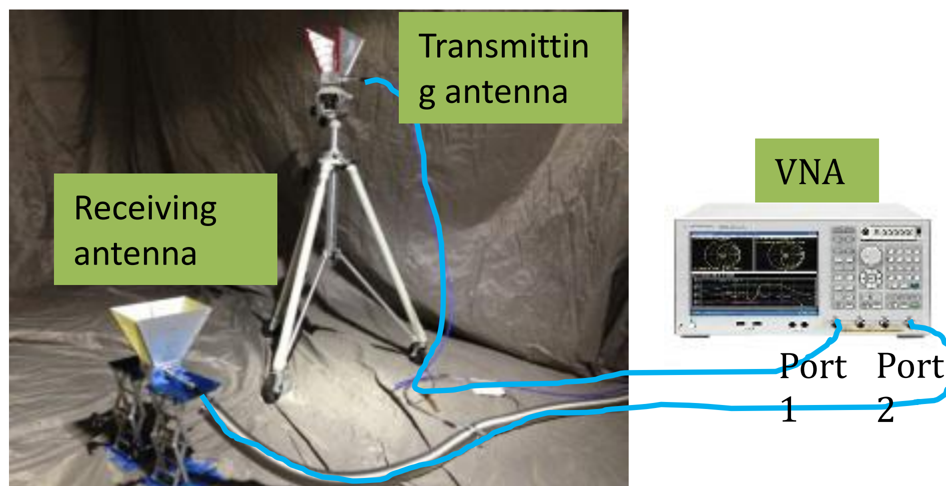

Figure 4.15 Calibration setup from TRP measurement.

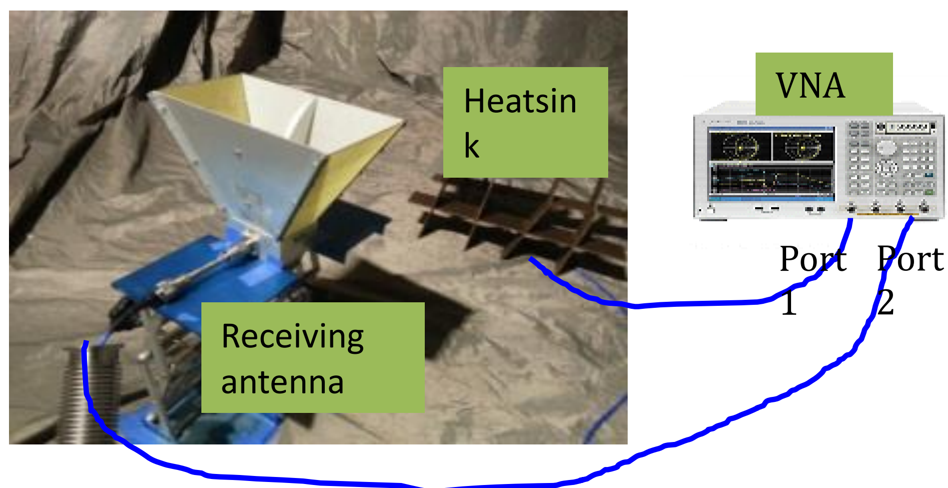

Figure 4.16 Actual DUT measurement setup from TRP measurement.

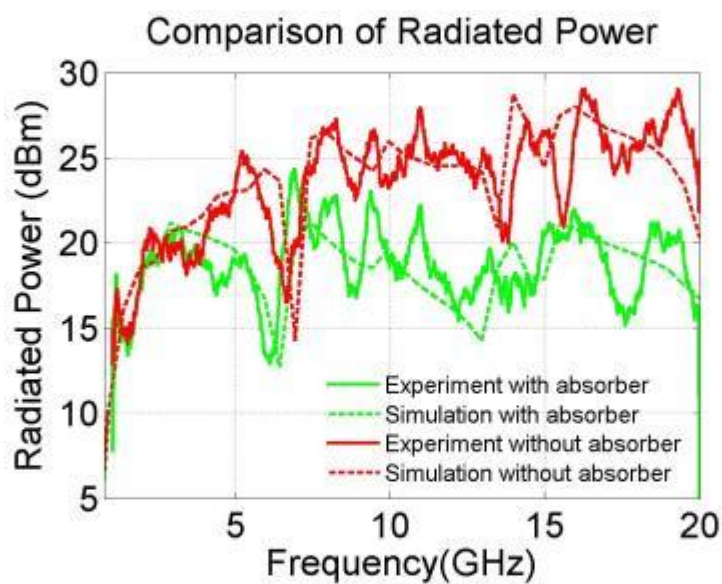

Figure 4.17 TRP spectrums comparison with and without the absorber material from experiment and simulation.

As seen from the measurement results, the TRP from the heatsink with the absorber material below it reduces to approximately 5 dB for frequencies higher than 5 GHz. Also the measurement results agree well with the simulation results.

Next for the DUT 1, a picture frame size absorber material is kept below the main heatsink corresponding to the ASIC. Also it is kept around the heatsink corresponding to PHY. Here it cannot be kept below the heatsink due to lack of space beneath it. The placement of the absorber material is as shown below in Figure 4.18.

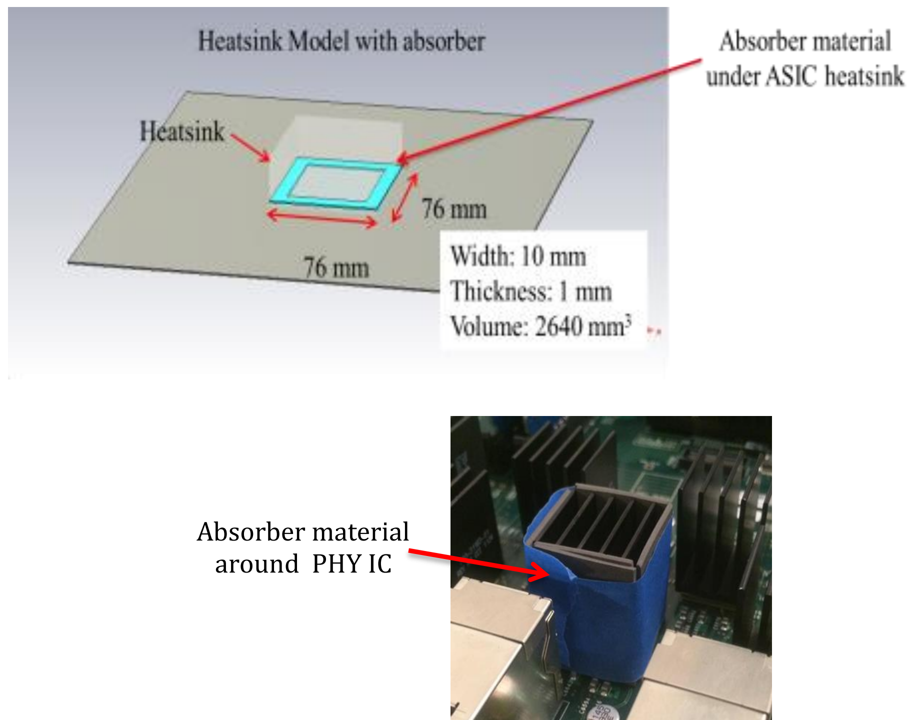

Figure 4.18 Actual placement of the absorber material.

As shown previously, ESM methodology is applied on the scanned fields for different cases without and with the absorbing material. The results are shown in Figure 4.19 through Figure 4.22. The color scale in all the figures has been normalized to the case without the absorber material for the sake of comparison.

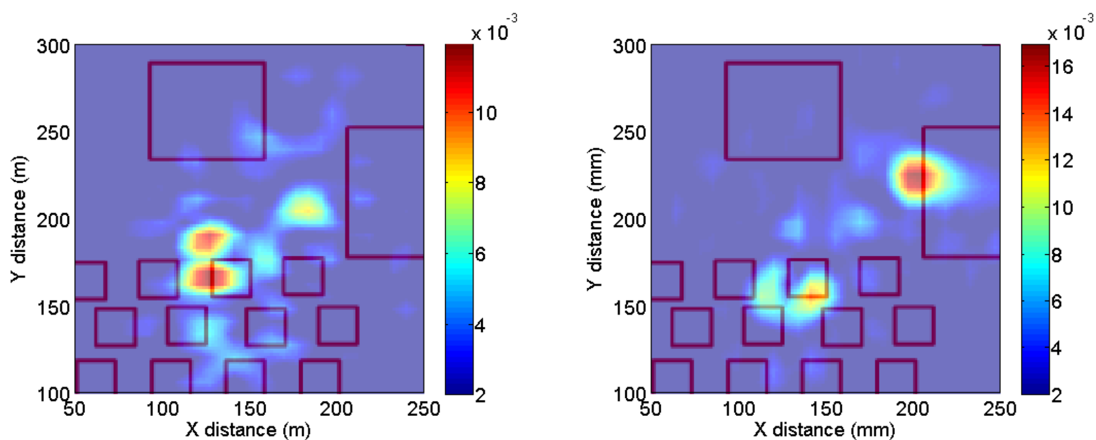

Figure 4.19 Reconstructed E_x and E_y field magnitude on the DUT without any absorber material.

As shown in the case without the absorber material, the main source of radiation is located near the main ASIC heatsink and near the PHY heatsink.

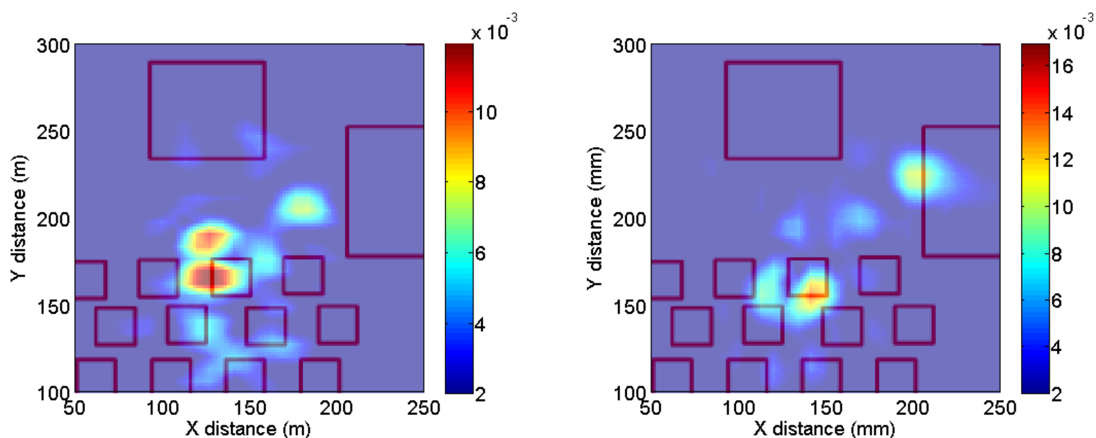

Figure 4.20 Reconstructed E_x and E_y field magnitude on the DUT with the absorber material below the ASIC heatsink.

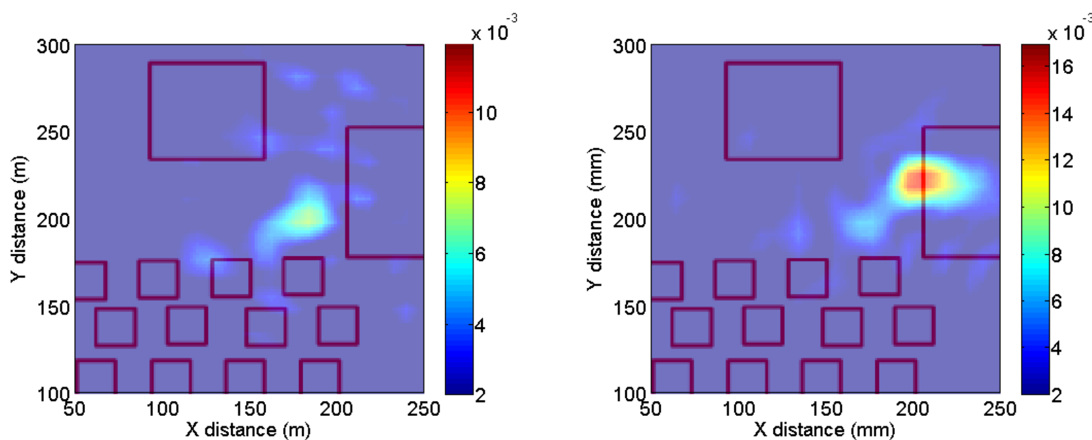

Figure 4.21 Reconstructed E_x and E_y field magnitude on the DUT with the absorber material around the PHY heatsink.

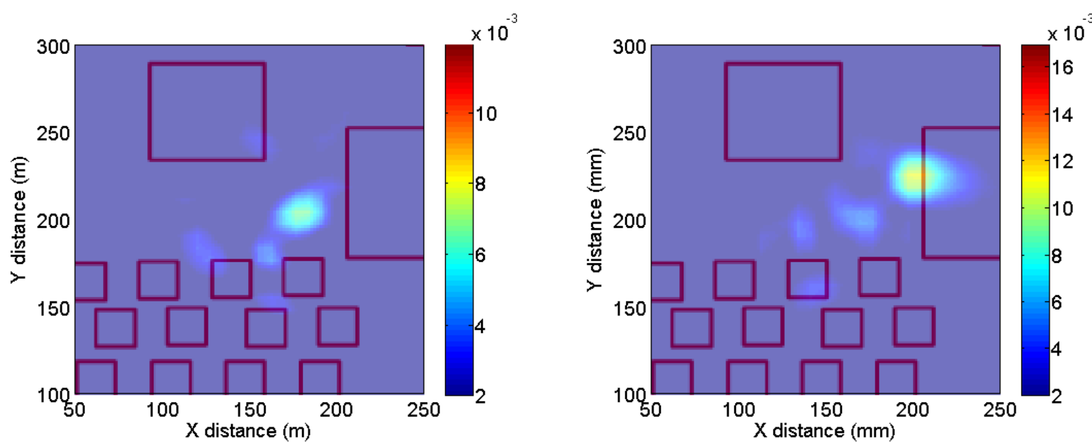

Figure 4.22 Reconstructed E_x and E_y field magnitude on the DUT with the absorber material around the PHY heatsink and below the ASIC heatsink.

To validate the reduction in the total radiated power from the ESM measurements, TRP measurement is also performed using a reverberation chamber method discussed previously. The TRP results are shown in Figure 4.23, Figure 4.24 and Figure 4.25.

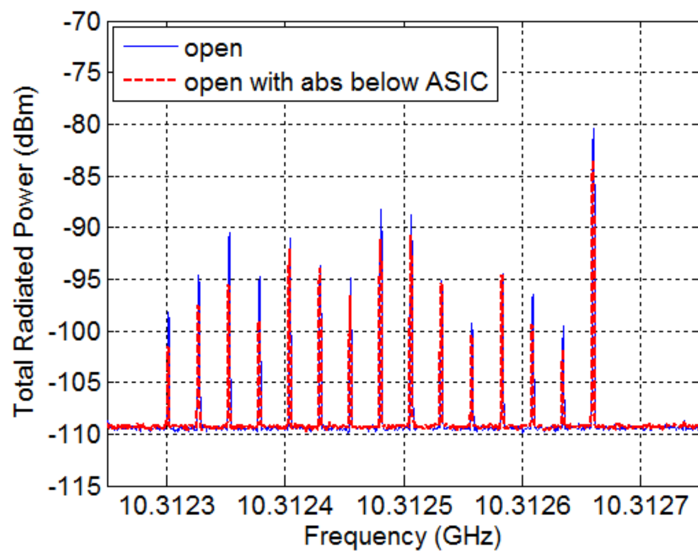

Figure 4.23 TRP results for DUT1 with and without the absorber below ASIC heatsink.

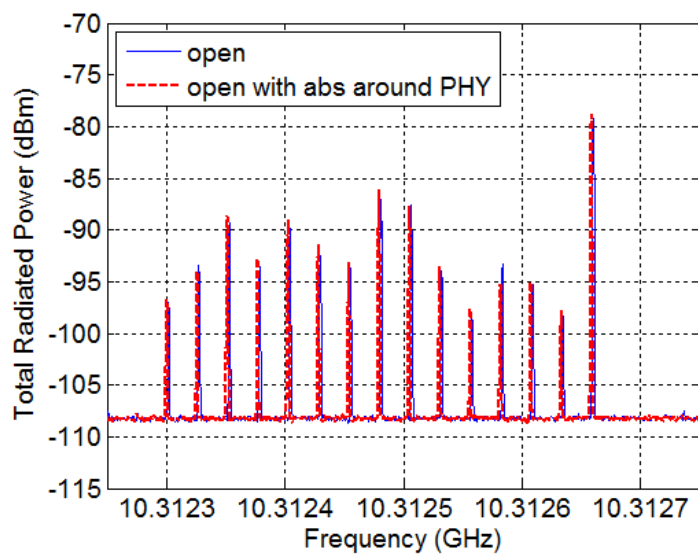

Figure 4.24 TRP results for DUT1 with and without the absorber around PHY heatsink.

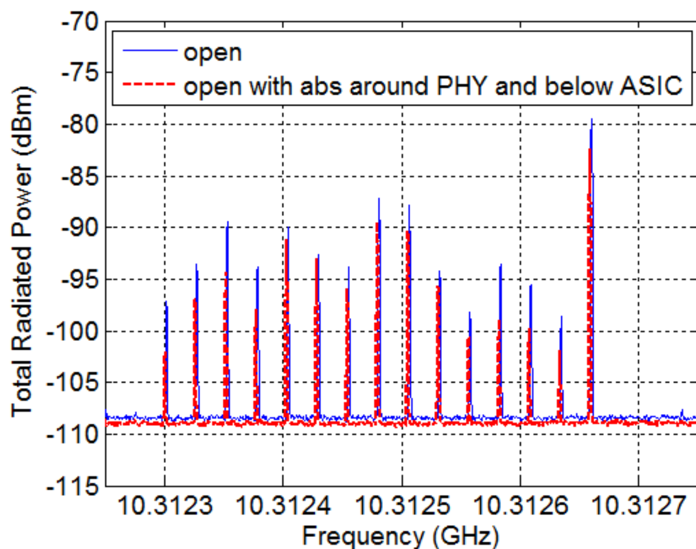

Figure 4.25 TRP results for DUT1 with and without the absorber around PHY heatsink and below ASIC.

The TRP reduction obtained using the absorber material calculated using the ESM methodology and using the RC method are summarized in Table 4.1 below.

Table 4.1 Table showing the reduction in the TRP with absorber material at different locations.

Frequency Peak # 12	TRP using ESM method	TRP using RC
With absorber only below the ASCI heatsink	≈0 dB	≈1 dB
With absorber only around the PHY heatsink	≈2 dB	≈2 dB
With absorber below the ASCI heatsink and around PHY heatsink	≈4 dB	≈5 dB

As shown in the table, the reduction obtained TRP calculation using the ESM agrees closely with the RC measurement results. More reduction is obtained by placing the absorbing material around the PHY heatsink instead of below the ASIC heatsink.

The analysis performed for Freq # 12 was also extended for another frequency corresponding to frequency peak # 15 (freq #15). The focused E_x and E_y field magnitude on the PCB plane for frequency # 15 without any absorber material are as shown below in Figure 4.26 and Figure 4.27.

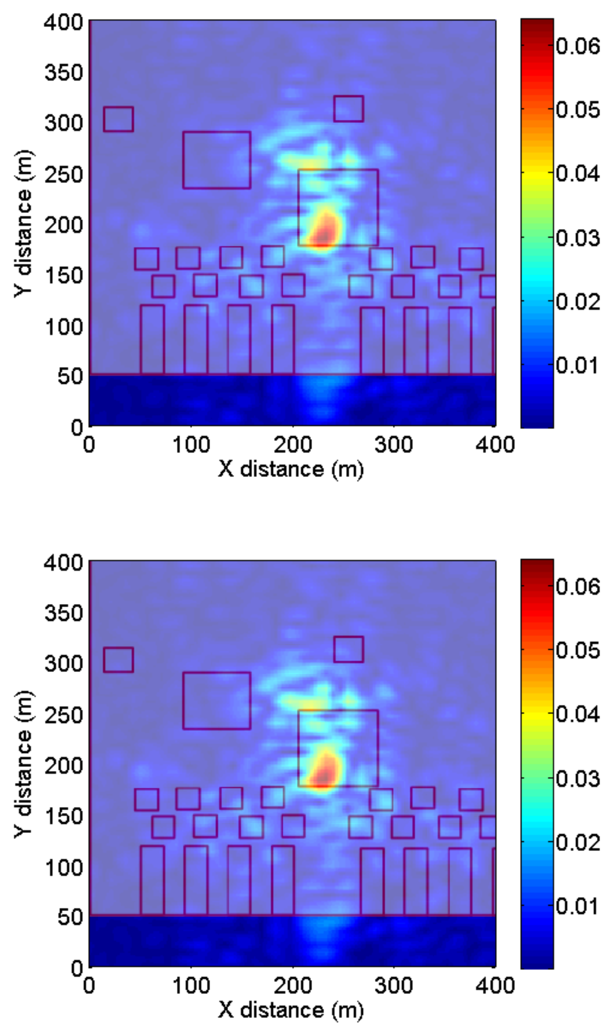

Figure 4.26 Reconstructed E_x fields at the PCB plane, without absorber.

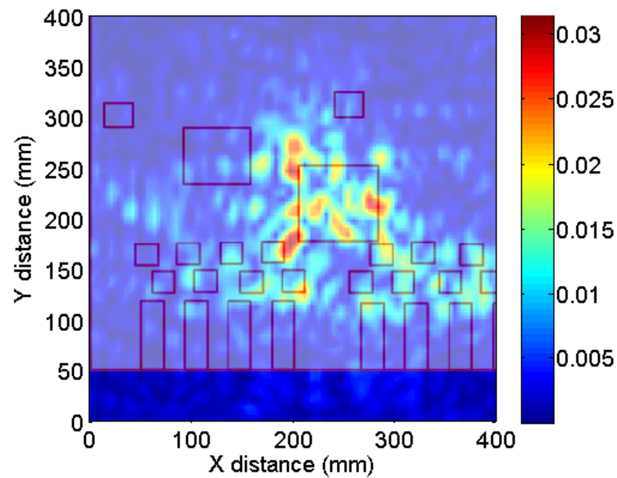

Figure 4.27 Reconstructed E_y fields at the PCB plane, without absorber.

As shown in results above, the main source of radiation seem to be mainly from the main ASIC heatsink, so the absorber material is placed below the main heatsink only. The results for reconstructed fields on the PCB plane with the absorber material are shown in Figure 4.28 and Figure 4.29.

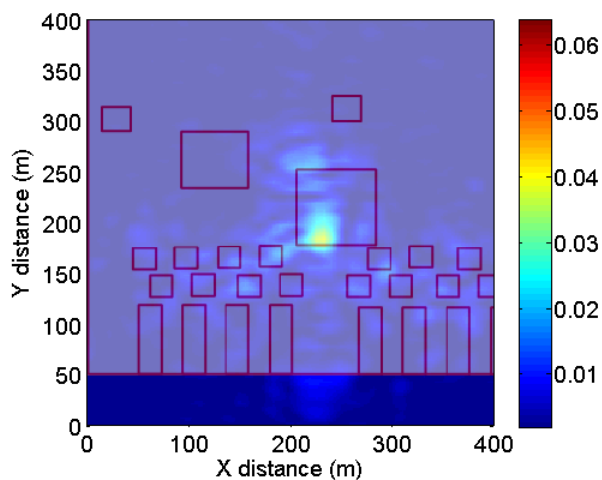

Figure 4.28 Reconstructed E_x fields at the PCB plane, with absorber.

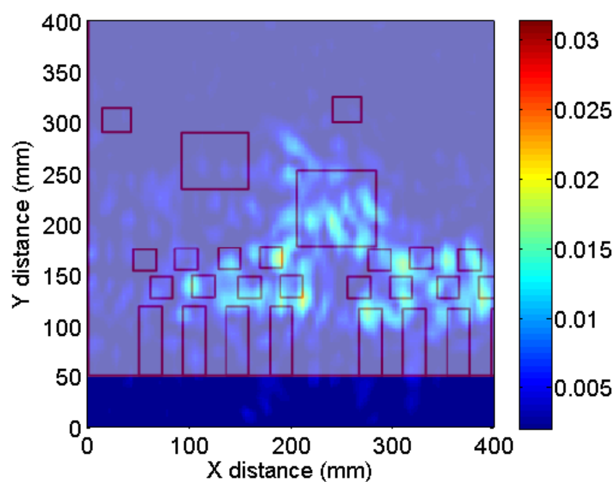

Figure 4.29 Reconstructed E_x fields at the PCB plane, with absorber.

The reduction in the TRP calculated from ESM method is validated by measurements from RC. The results of the reduction in the TRP after placing the absorber material below the main ASIC heatsink are summarized in Table 4.2 below.

Table 4.2 Table showing the reduction in the TRP with absorber material below the main ASIC heatsink.

Frequency Peak # 15	TRP using ESM method	TRP using RC
With absorber only below the ASIC heatsink	3 dB	3 dB

In this example too, the reduction in the TRP from the reverberation chamber data agrees closely with the calculated TRP reduction from the reconstructed fields on the PCB plane.

4.2. REAL DUT 2 – FPGA EVALUATION BOARD

For a real hardware board such as a FPGA board, a reference signal to one port of the VNA can be obtained by either tapping the signal from the board or by using a stationary reference antenna. The other port of the VNA can be used as an input from the scanning antenna. For the FPGA board used in this measurement, the reference is obtained by tapping the signal from one of the FPGA outputs.

The FPGA is programmed to output a pseudorandom bit sequence at one of the differential channels. The clock frequency for the FPGA is 3.125 GHz. The spatial resolution at the clock frequency calculated using (6) which is 5 cm might be not enough to resolve the location of source on the FPGA board, so the third harmonic 9.375 GHz, giving the maximum resolution of 1.6 cm, is used to conduct the experiment. The scanning antenna used is a log-periodic antenna with a range of 2-11 GHz connected on the moving arm of the API 3-axis EMI scanning system. The scanning step is kept as 5

mm in both x and y directions. The diagram of the phase resolved measurement is provided in Figure 4.30.

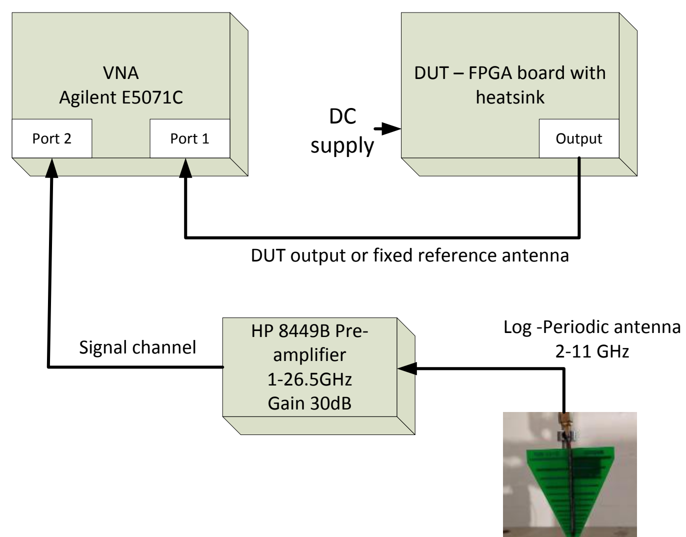

Figure 4.30 FPGA board phase measurement setup.

The result of scanning at a height of 10cm above the FPGA board is shown in Figure 4.31 and Figure 4.32. As observed no useful information about the sources of radiation can be obtained from the scanned fields.

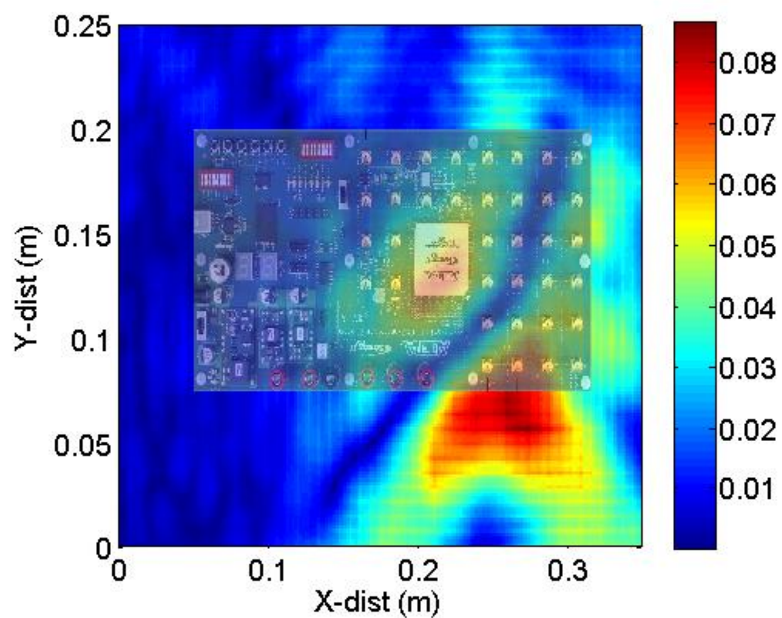

Figure 4.31 Measured E_x field magnitude ratio on a rectangular grid at 10 cm height.

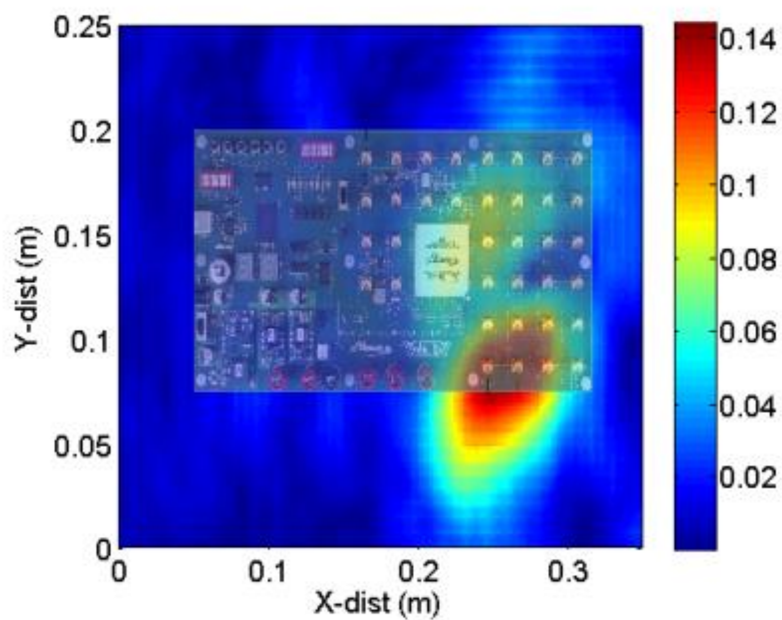

Figure 4.32 Measured E_y field magnitude ratio on a rectangular grid at 10 cm height.

The reconstructed fields on the PCB plane are shown at Figure 4.33 and Figure 4.34.

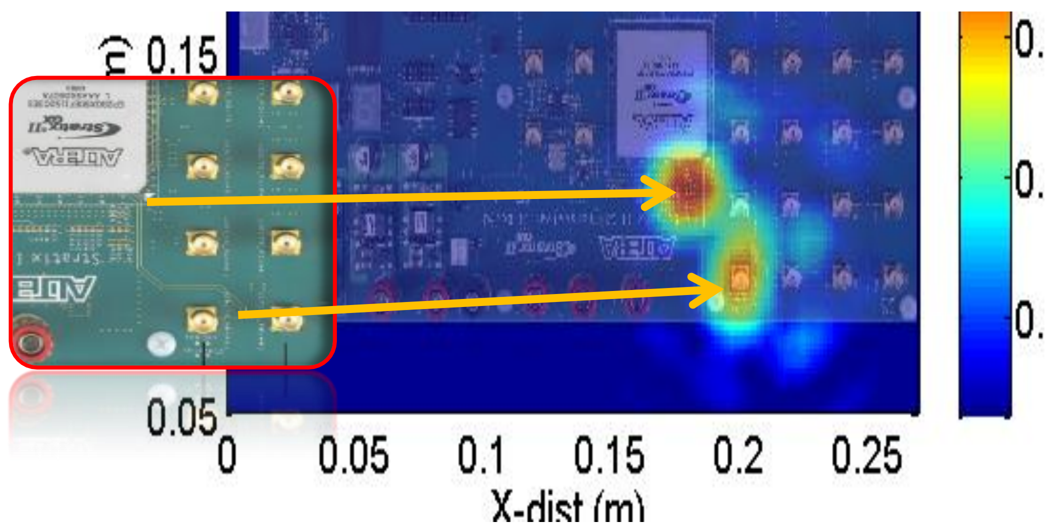

Figure 4.33 Reconstructed E_x field magnitude ratio on the source plane.

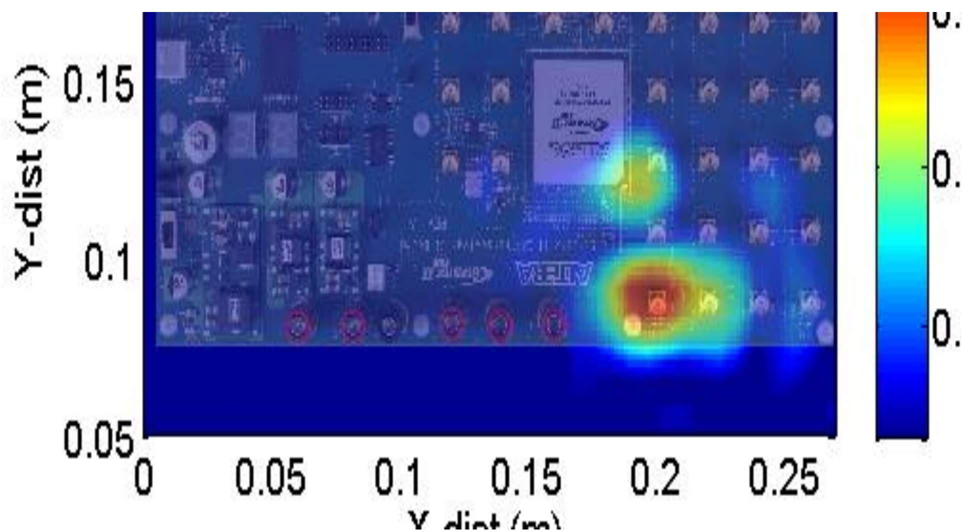

Figure 4.34 Reconstructed E_y field magnitude ratio on the source plane.

As observed the dominant source of radiation for the x-orientation seems to be coming from the differential trace-FPGA interface as well as the other open SMA connector on which the differential clock line from the FPGA terminates. Also for they orientation, the SMA connectors seems to be the dominant source of radiation rather than the FPGA itself. The open SMA is terminated to reduce the reflections and thus the common mode current on the differential line. The results of the reconstructed images after termination are as shown below in Figure 4.35 and Figure 4.36. It can be seen that there is a significant drop in the overall radiated emission from both the heatsink as well as the open SMA connector.

Figure 4.35 Reconstructed E_x field magnitude ratio on the source plane.

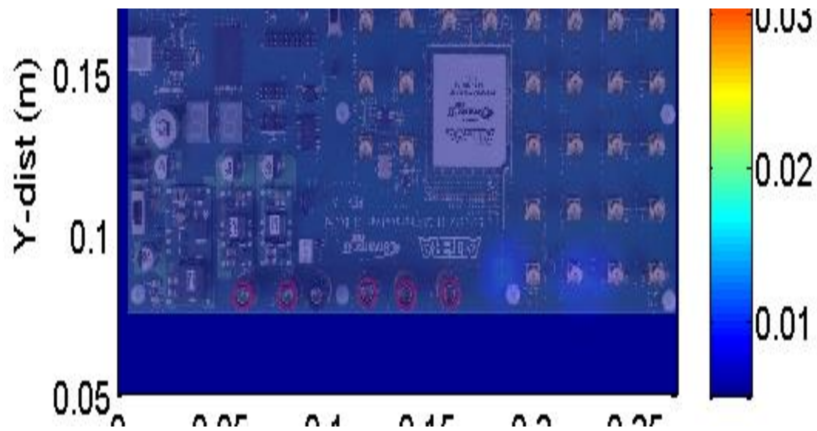

Figure 4.36 Reconstructed E_y field magnitude ratio on the source plane.

4.3. REAL DUT 3 – ORTHOGONAL PCBS

Another real DUT tested was a backplane like structure with two PCB orthogonal to each other as shown in Figure 4.37. Here multiple peaks are observed near the 10-12 GHz range out of which one of the peaks is chosen as the test frequency. Here the scanning was performed at two different heights. One scanning is performed at height lower than the vertical PCB of the DUT. This limited the range of scanning only till the vertical PCB in the scanning plane. Another measurement is performed at a height above the vertical PCB. In this way the scanning plane was extended beyond the vertical PCB of the DUT. Here the same setup as used in case of real DUT 1 (4.1) is used (Figure 4.38). The frequency of scanning is 11.936 GHz.

Figure 4.37 DUT with vertical PCB.

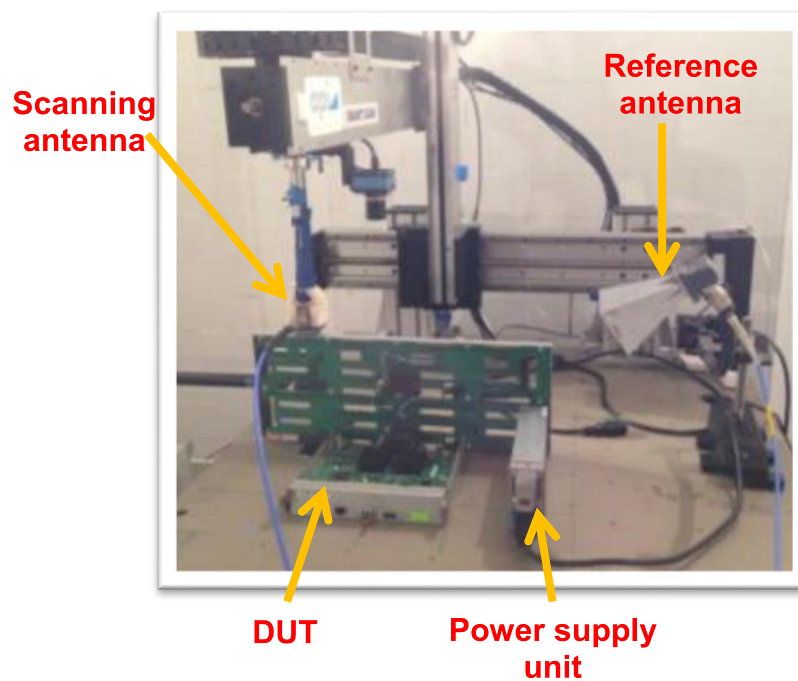

Figure 4.38 Measurement setup.

The scanned field magnitude and phase for the case with lower height (140mm) are shown in Figure 4.39 and Figure 4.40.

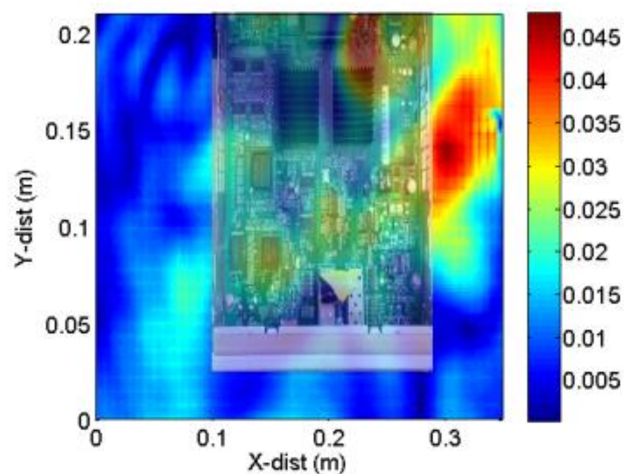

Figure 4.39 Measured field magnitude on the scanning plane at lower height.

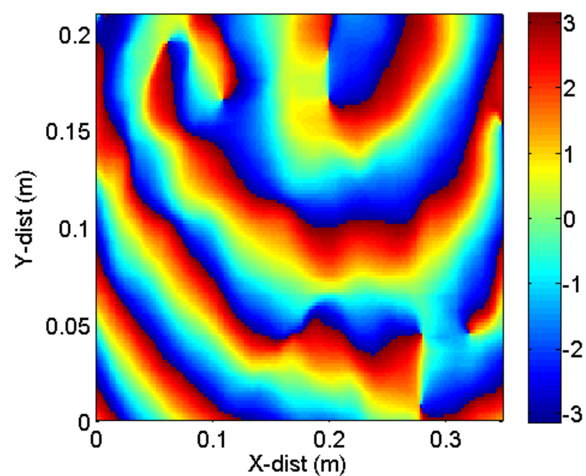

Figure 4.40 Measured field phase on the scanning plane at lower height.

As seen no actual information about the location of source can be derived from the scanned fields. After apply the ESM transformation, the reconstructed fields are shown in Figure 4.41.

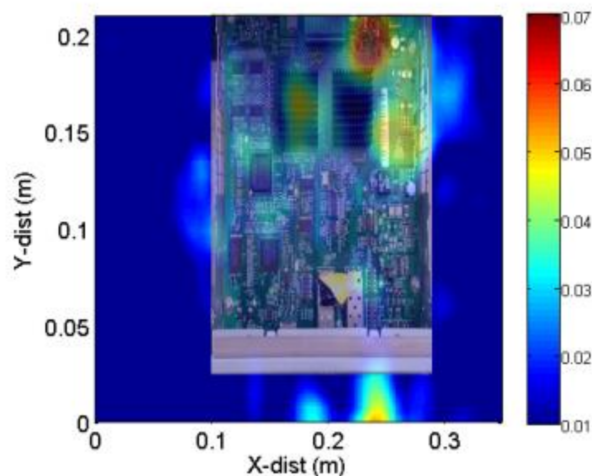

Figure 4.41 Reconstructed fields on the source plane.

Scanning at height above the DUT (175mm) leads to discontinuity in the measured phase due to the vertical PCB as shown in Figure 4.42.

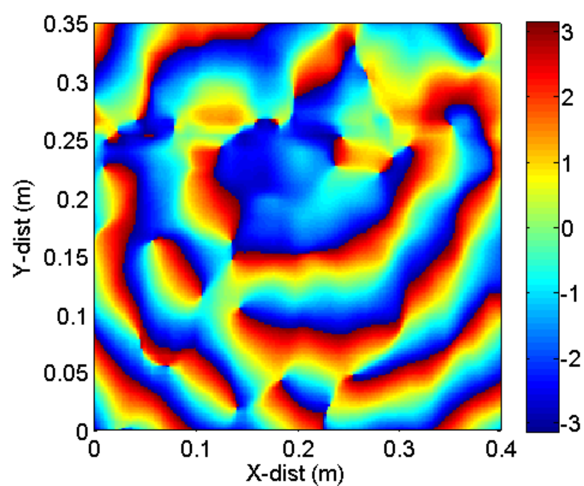

Figure 4.42 Measured field phase on the scanning plane at 175mm.

This discontinuity in phase creates artifacts in the reconstructed image on the source plane as shown in Figure 4.43.

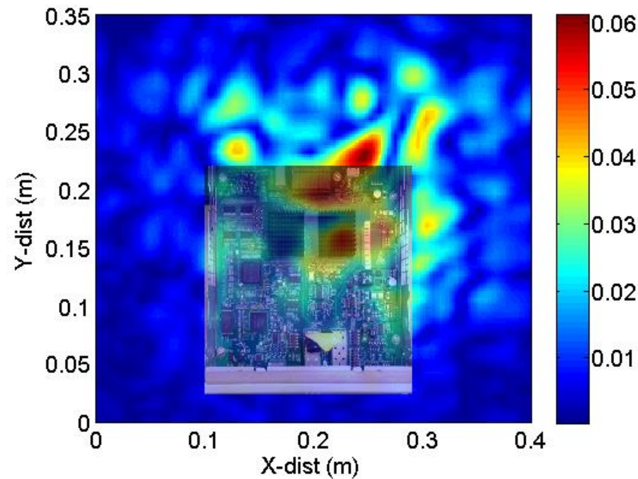

Figure 4.43 Reconstructed fields on the source plane.

4.4. TIME-DOMAIN PHASE MEASUREMENT METHOD

Phase measurement using the frequency domain method (VNA tuned receiver) has been shown in the previous sections. The main limitation of the frequency domain method is that measurement can be performed only for one single frequency as zero spanning is required. If the radiated spectrum consists of more than one frequency, then the frequency domain method would need to be repeated at all the frequencies of interest. Also in the frequency domain method, the image rejection of the instrument should be as high as possible or the input signals should be passed through narrow band-pas filter

before feeding it to the VNA. For time-domain method, image signals generated by non-linear devices such as mixers can be rejected by using external filtering.

For measuring the phase of a broadband signal, time-domain based phase measurement method can be utilized. Here the time response of the radiated spectrum is captured for the measurement channel and the reference channel. Next the time response is converted into the frequency spectrum by using Fourier transforms. By subtracting the measurement channel spectrum from the reference channel spectrum, the phase difference can be obtained.

The main drawbacks of time-domain phase measurement method as compared to the frequency domain method is that the sampling rate of the instrument used for measurement should be higher than the maximum radiated frequency to be measured. If not, then the measurement channel and the reference channel frequency have to be down converted using super heterodyne principle. Also to have enough spectral resolution, the length of the time-domain signal should be as long as possible. This would require additional memory depth in the instrument and may increase the computation overhead.

For demonstrating the time-domain based phase measurement method, the PCB with two patches is used. One of the Patch P1 is excited by an external signal generator at 8.2 GHz with 0 dBm input power. The setup for phase measurement using the time-domain method is as shown below in Figure 4.44.

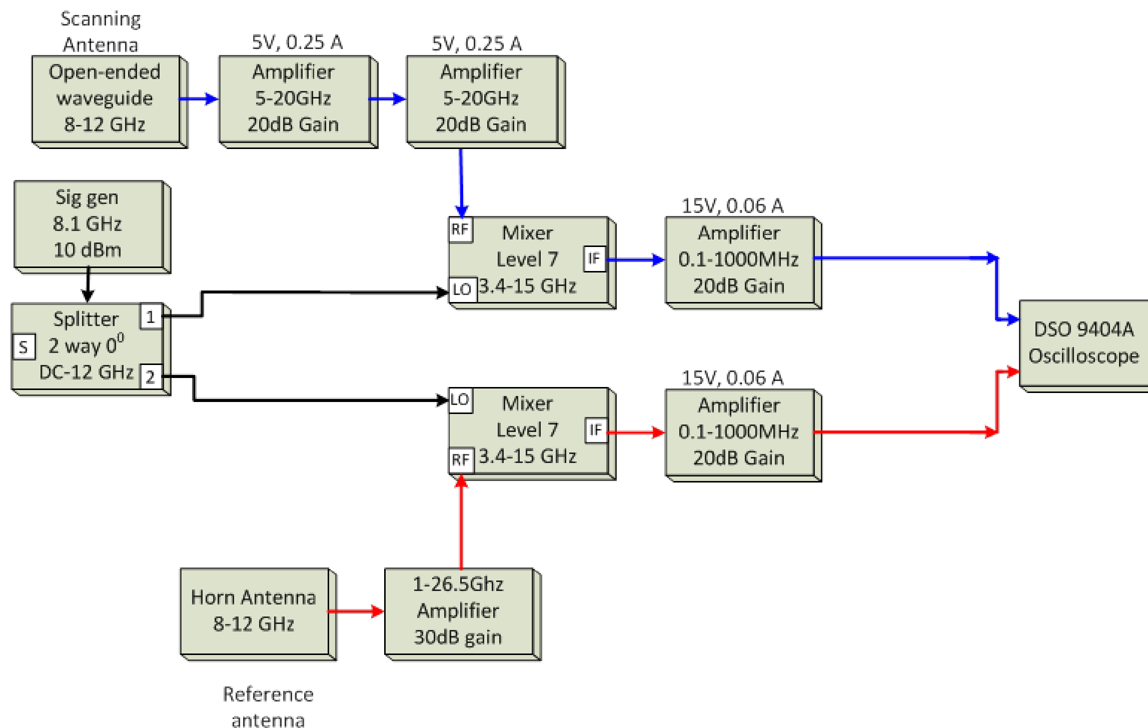

Figure 4.44 Time-domain based phase measurement setup.

Here the principle of super-heterodyning is used to down-convert the input signal to a lower frequency that is within the bandwidth of the sampling instrument. A 2-way resistive splitter splits the signal from a signal generator to feed the reference and the measurement channel local oscillators. The signal generator frequency for the reference is kept at 8.1 GHz with 10 dBm output enough to drive the local oscillators after compensating for the splitter insertion loss. The mixer is a level 7 mixer with a frequency range of 3.4 GHz to 15 GHz. In the measurement channel the RF input to the mixer comes from the scanning antenna after sufficient amplification, whereas in the reference channel, the RF input to the mixer comes from the reference antenna after sufficient amplification. The difference output from the mixer which is centered around 100 MHz

(8.2 – 8.1 GHz) is selected and further amplified to feed it to the two channels of a digital sampling oscilloscope. The scope is triggered for a single sweep only after the scanning antenna has arrived at the correct scanning location. This ensures the signal sampled on the reference as well as the measurement channel is from the same time instant. The advantage of this method is that image rejection can be achieved by using external filters.

The measured scanned field magnitude and phase at 100 mm height above the DUT are as shown below in Figure 4.45.

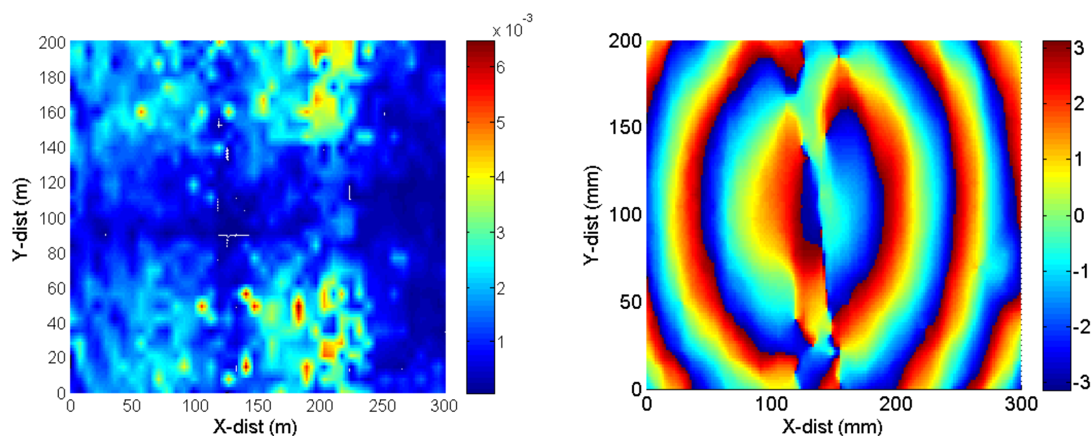

Figure 4.45 Measured field magnitude and phase at 100 mm height.

After applying the ESM methodology on the measured fields obtained on the scanning plane using the time-domain measurement method, the fields on the PCB can be obtained. The E_x and E_y field component magnitude on the PCB plane are as shown in Figure 4.46 and Figure 4.47. As observed, it correctly locates the source of radiation

(Patch P1). Similarly the time-domain phase measurement method can be used for other active DUT with appropriate filtering to reject the image products.

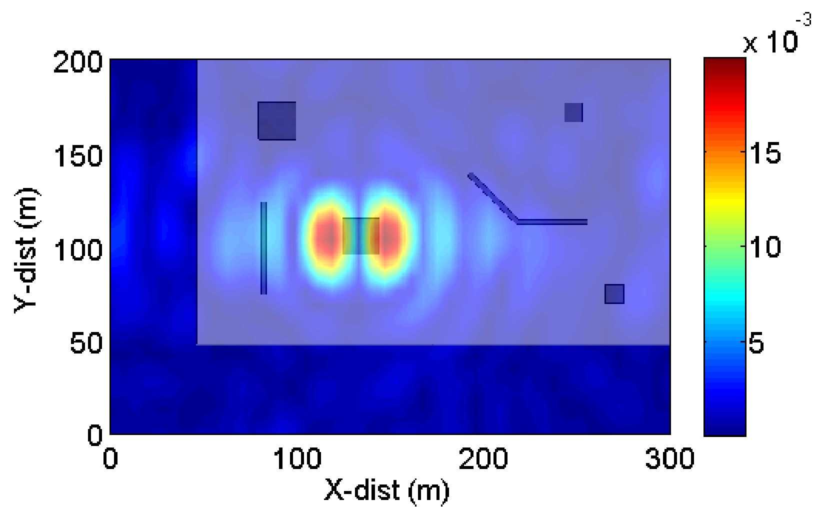

Figure 4.46 Reconstructed E_x field magnitude on the PCB plane.

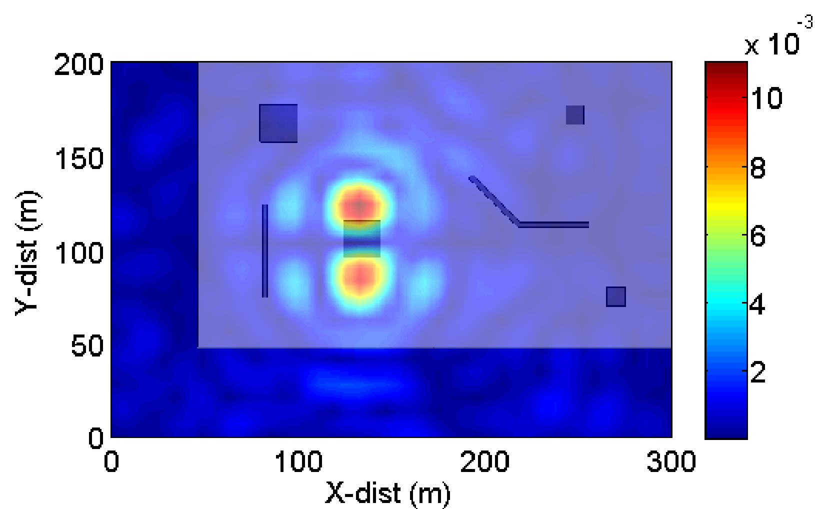

Figure 4.47 Reconstructed E_y field magnitude on the PCB plane.

5. CONCLUSION & FUTURE WORK

The first step in mitigating EMI involves identifying the sources of radiation on the DUT. The ESM methodology presented in this paper can help to approximately identify the sources of radiation on the PCB. After the sources are located, individual sources can be distinguished and an attempt can be made to identify the driving source. Individual sources can be isolated by using masking algorithms and individual far-field contributions can be calculated. It is shown that the total radiated power from each source can be estimated with good accuracy. Once dominant source of EMI can be identified, appropriate EMI fixes can be applied to reduce the radiated emissions. This can lead to more cost-effective EMI mitigation solutions.

Next steps for the project include investigating methods to reduce the overall scanning time. One method is to use a combination of an antenna array and switches/multiplexers to scan more than one scanning point at a time. The main drawback would be to design such an array at different frequencies to be scanned and complexity involved in the switching circuit. Other challenges would be the providing sufficient gain and reducing cross talk between adjacent elements. A second approach is to use method such as compressed sensing algorithm to reduce the total number of scan points. In compressed sensing, the scanning is performed with the rate of the sparsity of the field rather than the rate of the variation (Nyquist rate). This reduces the acquisition time by reducing the number of scanned points.

BIBLIOGRAPHY

[1] A.D. Yaghjian, "An Overview of Near-field Antenna Measurements," IEEE Transactions on Antennas and Propagation, vol. ap-34, no. 1, Jan. 1986.

[2] D. Baudry, C. Arcambal, A. Louis, B. Mazari, P. Eudeline, "Applications of the Near-Field Techniques in EMC Investigations," *IEEE Transactions on Electromagnetic Compatibility*, vol. 49, no. 3, pp. 485-493, Aug. 2007.

[3] D. Sheen, D. McMakin, T. Hall, "Three-dimensional Millimeter-Wave Imaging for concealed Weapon Detection," in *IEEE Transactions on Microwave Theory and Techniques*, vol. 49, no. 9, Sept. 2001.

[4] W.M. Brown, "Synthetic Aperture Radar," *IEEE Transactions on Aerospace and Electronic Systems*, vol.AES-3, no. 2, pp. 217-229, Mar. 1967.

[5] E. C. Fear, S. C. Hagness, P. M. Meaney, M. Okoniewski, M. A. Stuchly, "Enhancing Breast Tumor Detection with Near-Field Imaging," *IEEE Microwave Magazine*, vol. 3, no. 1, pp.48-56, Mar. 2002.

[6] M. Fallahpour, J.T. Case, M. Ghasr, and R. Zoughi, "Piecewise and Wiener Filter-Based SAR Techniques for Monostatic Microwave Imaging of Layered Structures," *IEEE Transactions on Antennas and Propagation*, vol. 62, no. 1, pp. 1-13, Jan., 2014.

[7] M. Fallahpour, M. Ghasr, J.T. Case, and R. Zoughi, "A Wiener Filter-Based Synthetic Aperture Radar (SAR) Algorithm for Microwave Imaging of Targets in Layered Media," *Materials Evaluation,* vol. 69, no. 10, pp. 1227-1237, Oct. 2011.

[8] M.T. Ghasr, M.A. Abour-Khousa, S. Kharkovsky., R. Zoughi, D. Pommerenke, "Portable Real-time microwave camera at 24GHz," *IEEE Transactions on Antennas and Propagation*, vol. 60, no. 2, pp. 1114-1125, Feb. 2012.

[9] D. J. Rochblatt, B.L. Seidel, "Microwave antenna holography*," IEEE Transactions on Microwave Theory and Techniques*, vol. 40, no. 6, pp. 1294-1300, Jun. 1992.

[10] G. Tricoles, N.H. Farhat, "Microwave holography: Applications and techniques," *Proceedings of the IEEE,* vol. 65, issue 1, pp. 108 – 121, Jan. 1977.

[11] K.S. Farhat, N. William, "Microwave holography applications in antenna development," *IEE Colloquium on Novel Antenna Measurement Techniques*, pp. 3/1, 3/4, 26, Jan. 1994.

[12] D. Smith, M. Leach, A. Sambell, "An indirect holographic method for determining antenna radiation patterns and imaging antenna fields," *IEEE Antennas and Propagation Society International Symposium,* vol. 3, pp.706-709, 2002.

[13] M. Popova, V. Boyanov, V. Vitkov, V. Peshlov, "An efficient procedure for calibration of scanning phased antennas by means of near field planar scanner," *15th International Conference on Microwaves, Radar and Wireless Communications*, vol. 1, pp. 58-61, 17-19 May 2004.

[14] P.L. Ransom, R. Mitra, "A method of locating defective elements in large phased arrays," *Proc. of the IEEE*, vol. 59, no. 6, pp. 1029-1030, Jun. 1971.

[15] J.J. Lee, E.M. Ferren, D.P. Woollen, K.M. Lee, "Near-field probe used as a diagnostic tool to locate defective elements in an array antenna," *IEEE Transactions on Antennas and Propagation,* vol. 36, no. 6, pp. 884-889, Jun. 1988.

[16] B. Toland, Y. Rahmat-Samii, "Application of FFT and DFT for image reconstruction of planar arrays in microwave holographic diagnostics," *Antennas and Propagation Society International Symposium, pp.* 292 - 295 vol.1, 7-11 May, 1990.

[17] B. Janice, "Differential Near-field Holography for small Antenna arrays," Thesis, 2011.

[18] J. D. Hanfling, G. V. Borgiotti and L. Kaplan, "The backward transform of the near field for reconstruction of aperture fields," *Proc. IEEE Antennas Propagation Symposium,* vol. 2, pp. 764 -767, 1979.

[19] D. J. Rochblatt and Y. Rahmat-Samii, "Effects of Measurement Errors on Microwave Antenna Holography," *IEEE Transactions on Antennas and Propagation*, vol. 39, no. 7, pp. 933–942, Jul. 1991.

[20] A.C. Newell, "Estimating the uncertainties due to truncation in planar near-field holograms," *AMTA Conference*, 2004.

[21] C. A. Rose, "Accuracy estimation of microwave holography from planar near-field measurements," *Microwave Instrumentation Technologies*, Available: www.mi-technologies.com

[22] G.F. Masters, "Hologram accuracy estimation," *AMTA Conference*, Nov. 13-17, 1995.

[23] P. K. Agrawal, “A method to compensate for probe positioning errors in an antenna near field test facility,” *in Antenna Propagat. Soc. Symp. Dig., Albuquerque, NM,* May 1982, vol. 1, pp. 218–221.

[24] C.A. Balanis, “Antenna Theory: Analysis and design,” 3rd Edition, Apr. 2005.

[25] P. Petre and T. K. Sarkar, “Planar near-field to far-field transformation using an equivalent magnetic current approach,” *IEEE Transactions of Antennas and Propagation*, vol 40, no. 11, pp. 1348-1356, Nov. 1992.

[26] J.T. Case, M.T. Ghasr, R. Zoughi, “Optimum Two-Dimensional uniform spatial sampling for microwave SAR-Based NDE imaging,” *IEEE Transactions on Instrumentation and Measurement*, vol. 60, no. 12, pp. 3806-3815, Dec. 2011.

[27] M. Abramowitz and M.W. Davidson, “Microscope Objectives: Numerical aperture and resolution,” *Molecular Expressions: Optical Microscopy Primer* (website), Florida State University, Apr., 2004.

[28] H. Kajbaf, J.T. Case, Z. Yang, Y.R. Zheng, “Compressed sensing for SAR-based wideband three-dimensional microwave imaging system using non-uniform fast Fourier transform,” *Radar, Sonar & Navigation*, IET , vol. 7, no. 6, pp. 658-670, July 2013.

[29] G. Muchaidze, J. Koo, Q. Cai, T. Li, L. Han, A. Martwick, K. Wang, J. Min, J. L. Drewniak, D. Pommerenke, “Susceptibility Scanning as a Failure Analysis Tool for System-Level Electrostatic Discharge (ESD) Problems,” *IEEE Transactions on Electromagnetic Compatibility,* vol. 50, no. 2, pp. 268-276, May 2008.

[30] P. Petre and T.K. Sarkar, “Differences between modal Expansion and integral equation methods for planar near-field to far-field transformation,” *Progress in Electromagnetics Research*, PIER 12, pp. 37-56, 1996.

[31] E. Joy, W. Leach, G. Jr. Rodrigue, “Applications of probe-compensated near-field measurements,” *IEEE Transactions on Antennas and Propagation*, vol. 26, no.3, pp.379-389, May 1978.

[32] CST Microwave Studio, Version 2011, www.cst.com

[33] X. Ren, P. Maheshwari, Y.-J. Zhang, V. Khikevich, J. Fan “The impact of near-field scanning size on the accuracy of far-field estimation,” to be published at the *IEEE EMC Symposium*, 2014.

[34] M. Sorensen, O. Franek, G.F. Pedersen, A. Radchenko, K. Kam, D. Pommerenke, "Estimate on the uncertainty of predicting radiated emission from near-field scan caused by insufficient or inaccurate near-field data: Evaluation of the needed step size, phase accuracy and the need for all surfaces in the Huygens' box," *Electromagnetic Compatibility (EMC EUROPE)*, 2012.

[35] A.D. Yahhjian, "Approximate formulas for the far-field and gain of open-ended rectangular waveguide," *IEEE Transactions on Antennas and Propagation*, vol. 32, no. 4, pp. 378-384, Apr. 1984.

[36] M. Kanda, R. Orr, "Near-field gain of a horn and an open-ended waveguide: Comparison between theory and experiment," *IEEE Transactions on Antennas and Propagation*, vol.35, no.1, pp.33,40, Jan 1987

[37] Y. Vives-Gilabert, C. Arcambal, A. Louis, D. F. Daran, P. Eudeline, B. Mazari, "Modeling Magnetic Radiations of Electronic Circuits Using Near-Field Scanning Method," *IEEE Transactions on Electromagnetic Compatibility*, vol. 49, no. 2, pp. 391-400, May 2007.

[38] J. Zhang, K.W. Kam, J. Min, V.V. Khilkevich, D. Pommerenke, J. Fan, "An Effective Method of Probe Calibration in Phase-Resolved Near-Field Scanning for EMI Application," *IEEE Transactions on Instrumentation and Measurement*, vol. 62, no. 3, pp. 648-658, Mar. 2013.

[39] M. Saitoh, T. Yamamoto, T. Sakamoto, H. Niori, M. Chino, and M. Kobayasi, "Electromagnetic wave absorber using dielectric (Ti)·magnetic(Fe) composite material for GHz frequency band," *Proceedings of the 12th IEEE International Symposium on Applications of Ferroelectrics*, vol. 2, pp. 871-874, 2000.

[40] Laird Technologies, "Microwave Absorber: ECCOSORB," [Online]. Available: http://www.eccosorb.com/products-eccosorb-bsr.htm.

[41] G. Koepke and J. Ladbury, "Radiated Power Measurements in Reverberation Chambers," *56th ARFTG Conference Digest-Fall*, vol. 38, pp.1-7, 2000.

[42] H. Hirayama, T. Yakabe, Y. Kami, "An imaging system for EM emitting sources using a 6-port correlator," *IEEE International Symposium on Electromagnetic Compatibility*, vol. 1, pp. 374-37, 2001.

[43] P.H. Harms, J.G. Maloney, M.P. Kesler, E.J. Kuster, G.S. Smith, "A system for unobtrusive measurement of surface currents," *IEEE Antennas and Propagation Society International Symposium*, vol. 3, pp. 1646-1649, 21-26 Jun. 1998.

[44] J.J.H. Wang, “An examination of the theory and practices of planar near-field measurement,” *IEEE Transactions on antennas and propagation,* vol. 36, no. 6, Jun. 1988.

VITA

Pratik Maheshwari was born in India, in 1986. He received the B.E. degree in Electronics Engineering, in 2008, from the University of Mumbai, India. He started his Ph.D. program in 2009 in the Electrical and Computer Engineering department at Missouri University of Science and Technology. He has also worked as a summer intern at Apple EMC Group for summer of 2013. He received his PhD degree in August 2014. His research interests include EMI source localization, Electrostatic discharge, and RF system design.